Department of Physics and Astronomy

University of Heidelberg

Diploma thesis
in Physics

submitted by
Katharina Kreplin
born in Nürnberg, Germany

February 2011

Selection of doubly Cabibbo suppressed $D^{*+} \to D^0(K^+\pi^-)\pi^+$ decays and measurement of the D^0 lifetime in $D^0 \to K^-\pi^+$ at the LHC*b* experiment

This diploma thesis has been carried out by Katharina Kreplin at the
Physical Institute
under the supervision of
Prof. Dr. Stephanie Hansmann-Menzemer

Selection of doubly Cabibbo suppressed $D^{*+} \to D^0(K^+\pi^-)\pi^+$ decays and measurement of the D^0 lifetime in $D^0 \to K^-\pi^+$ at the LHC*b* experiment

The LHC beauty (LHC*b*) experiment is one of the four main experiments at the Large Hadron Collider, colliding protons since March 2010 with a center-of-mass energy of 7 TeV. This thesis investigates the current status towards a mixing analysis in the D system in LHC*b* data. First, a selection of Doubly Cabibbo Suppressed (DCS) $D^0 \to K^+\pi^-$ decays in the presently largest LHC*b* data set is presented. The self tagging decay chain $D^{*+} \to D^0\pi^+$ is used. A signal of 1966 ± 28 decays is measured in $37\,\text{pb}^{-1}$ of data. The ratio of DCS decays to Cabibbo Favored (CF) $D^0 \to K^-\pi^+$ decays, using the same D^* decay chain, is measured with $(4.89 \pm 0.07) \times 10^{-3}$. Second, the D^0 lifetime is measured in the CF decay mode. In hadronic interactions the proper time distribution of heavy mesons is distorted due to trigger cuts on the final state hadrons' impact parameters. In this thesis an average proper time acceptance function is evaluated in the Monte Carlo (MC) simulation to correct for the distortion. Therefore, the track resolution in MC needed to be adapted to the track resolution measured in data. The D^0 proper time resolution is determined in MC to be (50.89 ± 11.38) fs. The fraction of D^0 coming from B decays is measured with (5.16 ± 0.20) % in data. The D^0 lifetime is measured in data with $\tau = (451.8 \pm 3.1(\text{stat.}) \pm 6.5(\text{syst.}))$ fs.

Selektion der doppelt Cabibbo unterdrückten $D^{*+} \to D^0(K^+\pi^-)\pi^+$ Zerfälle und D^0 Lebensdauermessung in $D^0 \to K^-\pi^+$ Zerfällen am LHC*b* Experiment

Das LHC beauty (LHC*b*) Experiment ist eines der vier großen Experimente am Large Hadron Collider, der seit März 2010 Protonen mit einer Schwerpunktsenergie von 7 TeV beschleunigt. Diese Arbeit bereitet eine D-Mischungsanalyse mit LHC*b* Daten vor. Zunächst wird eine Selektion von doppelt Cabibbo unterdrückten (DCS) $D^0 \to K^+\pi^-$ Zerfällen im momentan größten LHC*b* Datenset präsentiert. Selektiert werden $D^{*+} \to D^0\pi^+ \to (K^+\pi^-)\pi^+$ Zerfälle. 1966 ± 28 Signalzerfälle werden in $37\,\text{pb}^{-1}$ Daten gemessen. Die Messung des Verhältnisses von DCS Zerfällen zu Cabibbo bevorzugten (CF) $D^0 \to K^-\pi^+$ Zerfällen, auch aus D^* Zerfällen stammend, ergibt $(4.89 \pm 0.97) \times 10^{-3}$. Als Zweites wird die D^0 Lebensdauer in CF Zerfällen gemessen. In hadronischen Wechselwirkungen wird die Eigenzeitverteilung von schweren Mesonen durch Triggerschnitte auf die Stoßparameter der Endzustandshadronen verändert. Diese Arbeit bestimmt eine gemittelte Eigenzeitakzeptanzfunktion in der Monte Carlo (MC) Simulation um diese Veränderung zu korrigieren. Dafür musste die Spurauflösung in MC an die in Daten gemessene Spurauflösung angepasst werden. Die Eigenzeitauflösung wird in MC zu (50.89 ± 11.38) fs bestimmt. Der Anteil an D^0 Mesonen, die aus B Zerfällen stammen, beträgt (5.16 ± 0.20) % in Daten. Die Messung der D^0 Lebensdauer in Daten resultiert in $\tau = (451.8 \pm 3.1(\text{stat.}) \pm 6.5(\text{syst.}))$ fs.

Contents

Introduction **1**

1. Standard Model Introduction **3**

2. LHC*b* Experiment **10**
2.1. Large Hadron Collider . . . 10
2.2. LHC*b* Experiment . . . 11
2.2.1. Tracking Detectors . . . 14
Vertex Locator . . . 14
Trigger Tracker . . . 15
Tracking Stations . . . 16
2.2.2. Particle Identification Detectors . . . 17
Ring Imaging Cherenkov Detectors RICH1 and RICH2 . . . 17
Calorimeter System . . . 18
Muon system . . . 19
Particle Hypothesis . . . 21
2.3. LHC*b* Trigger . . . 21
2.3.1. Level 0 Hardware Trigger . . . 21
2.3.2. High Level Trigger . . . 22
2.4. LHC*b* Software Environment . . . 23
2.5. LHC*b* Physics Programme . . . 24
2.5.1. Measurement of Rare $B_s \to \mu^+\mu^-$ Decays . . . 25
2.5.2. Measurement of the Mixing Frequencies Δm_s and Δm_d . . . 25
2.5.3. Measurement of CP Violation in the B Meson System . . . 27

3. $\mathrm{D^0} - \mathrm{\bar{D}^0}$ Mixing **29**
3.1. General Mixing Formalism . . . 29
3.2. D^0 Mixing in $D^{*+} \to D^0(K^+\pi^-)\pi^+$ . . . 32

4. $D^{*+} \to D^0(K^+\pi^-)\pi^+$ Wrong Sign Selection **38**
4.1. Physics Background . . . 39
4.1.1. Combinatorial Background . . . 40
4.1.2. Random Soft Pion Background . . . 40
4.1.3. Double Misidentification Background . . . 40
4.1.4. WS D^0 Decay Signal Box . . . 41

4.2. WS Decay Selection Cuts . . . 42
4.2.1. Momenta Cuts . . . 43
Momentum . . . 43
Transverse Momentum . . . 43
4.2.2. Quality Cuts . . . 45
Track χ^2/ndf . . . 45
Vertex χ^2/ndf . . . 45
Direction Angle . . . 48
4.2.3. Particle Identification and Interchanged Mass Assignment Cuts . . . 48
Delta Log Likelihood . . . 48
D^0 Mass Swap . . . 52
4.2.4. Displacement Cuts . . . 52
Impact Parameter χ^2 . . . 53
Primary Vertex displacement χ^2 . . . 54
4.2.5. Candidate per Event Selection Criterion . . . 54
4.3. Signal Significance Optimization . . . 54
4.3.1. D^0 Daughters Quantities . . . 57
4.3.2. D^0 Quantities . . . 59
4.3.3. D^* and π_s Quantities . . . 61
4.4. WS Selection Efficiency . . . 62
4.5. Final WS Selection . . . 66

5. D^0 Wrong Sign Decay Signal Yield in Data **69**
5.1. Fit to the $\Delta M = m_{D^*} - m_{D^0}$ Distribution in MC . . . 69
5.2. Fit to the D^0 Mass Distribution in MC . . . 70
5.3. Stripping 07 Data Set . . . 72
5.3.1. Fit to the ΔM Distribution in Data . . . 73
5.3.2. Fit to the D^0 Mass Distribution in Data . . . 73
5.4. Stripping 12 Data Set . . . 76
5.4.1. Fit to the ΔM Distribution in Data . . . 77
5.4.2. Fit to the D^0 Mass Distribution in Data . . . 78

6. D^0 Lifetime Measurement **82**
6.1. Selection . . . 83
6.2. Lifetime Fit Principle . . . 84
6.3. Complete Lifetime PDF . . . 86
6.4. Track Resolution Smearing . . . 87
6.4.1. Smearing Idea . . . 87
6.4.2. Smearing Technique . . . 88
6.5. Proper Time Resolution . . . 93
6.6. Systematical Uncertainties . . . 98
6.6.1. Smearing Accuracy . . . 99
6.6.2. Proper Time Resolution Bias . . . 100
6.6.3. Lifetime Resolution Width . . . 103

6.6.4. Summary . . . 103
6.7. Selection Fine Tuning . . . 104
6.7.1. D^0 Daughters IP Error Scaling . . . 105
6.7.2. 2D Reweighting: D^0 Momentum Versus Flight Distance Error . . . 106
6.8. Prompt and Secondary D^0s Separation . . . 115
6.9. Trigger on Data . . . 117
6.10. Fit Procedure . . . 118
6.11. Lifetime Fit Results on Data . . . 119

7. Summary and Conclusion **124**

A. Appendix **126**
A.1. Additional Selection Optimization Curves . . . 126
A.2. Additional Remarks On An Alternative Lifetime Fit Approach . . . 128

Bibliography **137**

Introduction

The Large Hadron Collider (LHC), presently the most powerful collider in the world, started the first proton-proton collision data taking period at a center-of-mass energy of 7 TeV in March 2010. Up to now the LHC beauty (LHCb) experiment, one of the four large experiments at the LHC, recorded 37 pb^{-1} of data. LHCb is a dedicated B physics experiment.

The Standard Model was introduced more than 30 years ago and has been tested by many experiments. Up to now there is no single laboratory experiment which observed a significant deviation from the Standard Model. However, there are still many open questions and physicists expect new phenomena to be revealed at higher energies. The Cabibbo-Kobayashi-Maskawa (CKM) quark mixing mechanism of the Standard Model was extensively tested and confirmed to a tremendous especially by the B factories BaBar and Belle[1], which led to the Nobel Prize in physics in 2008. The goal of the LHCb experiment is to perform high precision measurements in the B system and search for deviations from the CKM-predictions, which would be an unambiguous sign of New Physics at the TeV scale and above. Besides the huge B physics programme, the LHCb experiment has also a promising charm physics programme. E.g. up to now, only the combination of the measurements of several experiments allowed for the observation of neutral D meson mixing. At LHCb, the first $5\,\sigma$ measurement of the D mixing parameters at a single experiment is expected to be performed based on the data taken in 2011. This thesis performs the first steps towards the analysis using the $D^{*+} \to D^0(K^+\pi^-)\pi^+$ decay.

A mixing analysis is a high precision measurement. The decay modes with mixing signature are singly or doubly Cabibbo suppressed. Compared to the dominant decay mode this leads to a high suppression factor of up to 3.8×10^{-3}. The reliable reconstruction of these decays and separating them from the physics background necessitates an excellent detector performance and a sophisticated online and offline data reconstruction. The inelastic cross-section which gives rise to huge combinatorial background is an order of magnitude higher than the charm cross-section[2]. In order to select the interesting physics events out of this background the long lifetime of the D^0 meson is exploited in the online and the offline reconstruction. This leads to a distortion of the proper time distribution of the reconstructed particles. As the mixing and CP violation analyses are time dependent analyses, a careful treatment of this bias is mandatory.

This thesis analyzes the first LHCb data to evaluate the present status towards a mixing analysis. Two steps preparing the analysis turned out to be already realizable on the early data. First, a dedicated selection of the doubly Cabibbo suppressed $D^0 \to K^+\pi^-$ decays is developed on minimum bias data and signal Monte Carlo samples. The aim of this selection is to reject all physics background from the Cabibbo favored decay, where the mass hypotheses of the D^0 daughters are mistakenly interchanged. Second, a D^0 lifetime measurement is performed on data using the

[1] e^+e^- collider running at the $Y(4S)$ resonance

[2] At 7 TeV the inelastic proton-proton cross-section is about 60 mb and the charm cross-section is about 5 mb.

Cabibbo favored decay $D^0 \to K^-\pi^+$. Several contributions to the systematic uncertainties of this measurement are investigated. An average proper time acceptance function is determined on Monte Carlo simulation, which required dedicated studies on the data Monte Carlo agreement.

This thesis is structured in the following way. Chapter 1 gives a short overview of the Standard Model of particle physics to introduce the relevant definitions concerning the quark mixing theory. Chapter 2 presents the LHC and the LHC*b* experiment focusing on the special detector features, e.g. the excellent vertex and momentum resolution needed for a mixing analysis. This chapter also briefly discusses some key measurements of the LHC*b* experiment, that have already reached competitive sensitivity based on the data set taken in 2010. Chapter 3 introduces the general CKM mixing formalism and focuses in detail on the mixing formalism in the D system to establish the observables that can be measured. The main own work of this thesis starts with chapter 4. In this chapter the optimization of the $D^{*+} \to D^0\pi^+ \to (K^+\pi^-)\pi^+$ selection on minimum bias collision data and on Monte Carlo signal data is presented. The result of this selection applied to the full 2010 data set is given in chapter 5. The various studies required for a D^0 lifetime measurement in data are described in detail in chapter 6. This chapter finishes with the D^0 lifetime fit performed on data. Chapter 7 summarizes the work presented in this thesis.

1. Standard Model Introduction

This chapter will give a short view over the Standard Model (SM) of particle physics. The SM is a quantum theory. Elementary particles are quantum states of the SM, characterized by quantum numbers denoting symmetries. The SM defines two types of elementary particles, fermions and bosons, distinguished by their spin quantum number.

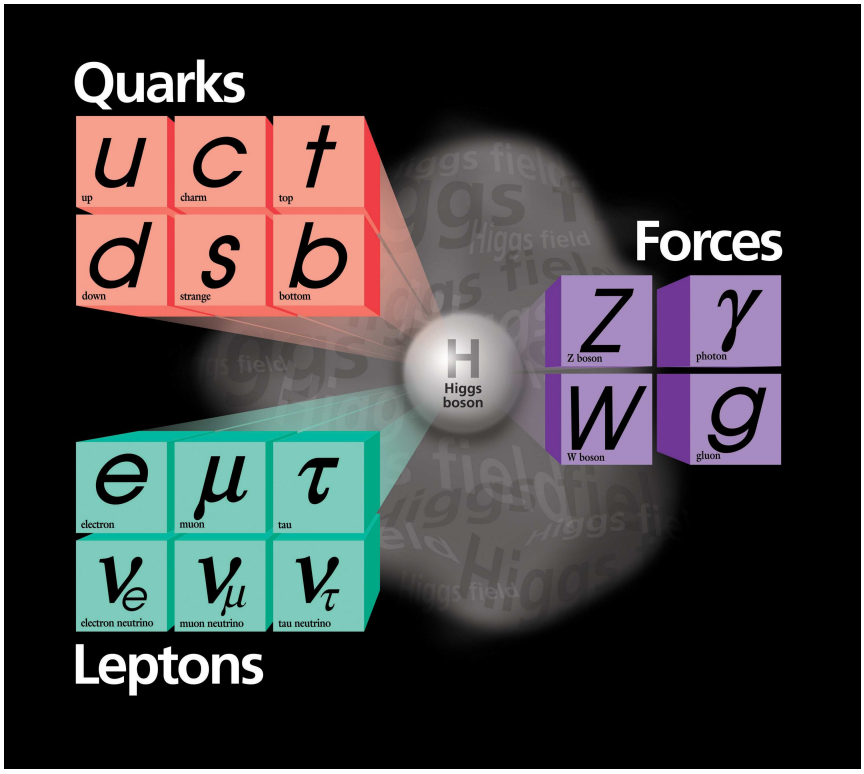

Figure 1.1.: The fundamental particles of the standard model. [25]

Fermions are characterized by having half integer spin and being the building blocks of matter. Quarks and leptons are fermions, each divided in three generations containing two types of fermions. In the quark sector there are six so called flavors, up, down, strange, charm, beauty and top. Every up-type flavor (up, charm and top) has its down-type flavor-partner (down, strange and beauty) forming three generations. In the lepton sector there are three flavors, electron, muon and tau. Every flavor is covered by a charged lepton and its neutral neutrino partner. All fermions and their antiparticles are observed. More fermion quantum numbers are listed in table 1.1.

	Type	1st generation	2nd generation	3rd generation
Leptons	neutrino	ν_e ($< 2\,\mathrm{eV}$)	ν_μ ($< 0.19\,\mathrm{MeV}$)	ν_τ ($< 18.2\,\mathrm{MeV}$)
	lepton	e ($511\,\mathrm{keV}$)	μ ($106\,\mathrm{MeV}$)	τ ($1.78\,\mathrm{GeV}$)
Quarks	up	u ($2\,\mathrm{MeV}$)	c ($1.25\,\mathrm{GeV}$)	t ($174\,\mathrm{GeV}$)
	down	d ($5\,\mathrm{MeV}$)	s ($95\,\mathrm{MeV}$)	b ($4.2\,\mathrm{GeV}$)

Table 1.1.: Fermion content of the Standard Model: quarks and leptons. The approximate particle masses are given in parenthesis. [19]

Bosons are characterized by having integer spin and being the fundamental force carriers, they mediate the interactions between particles. The photon (γ) mediates the electromagnetic force, the gluons mediate the strong force and the Z^0 and $W^\pm$ bosons mediate the weak force. One boson is still not detected yet, the Higgs boson. The Higgs boson, if it exists, will explain how elementary particles become massive. It is an integral and pervasive component of the material world. More boson quantum numbers are listed in table 1.2.

interaction	(gauge) bosons	mass	relative strength
Strong	gluons ($g_1, \ldots, g_8$)	0	$\alpha_s \sim \mathcal{O}(1)$
Electromagnetic	photon (γ)	0	$\alpha \sim \mathcal{O}(10^{-2})$
Weak	$W^\pm$	$80\,\mathrm{GeV}$	$\alpha_W \sim \mathcal{O}(10^{-6})$
	Z^0	$91\,\mathrm{GeV}$	
—	Higgs boson (H^0)	$> 114\,\mathrm{GeV}$	—

Table 1.2.: Boson content of the Standard Model and the approximate particle mass and relative strength of the corresponding interaction. [19]

Although the SM explains the action of three of the four fundamental forces very successful, the fourth force, gravitation, is not included in the theory. Each included force is described by its own quantum theory.

Quantum Chromodynamics (QCD) is the quantum theory of the strong force. It acts on a quark quantum number called color. There are three colors, red, green and blue and their three anti-colors, anti-red, anti-green and anti-blue. Quarks can change their color by exchanging a gluon with another quark. The principle of confinement postulates, that quarks only occur in color neutral bound states called hadrons. There are two types of hadrons, baryons, built from three quarks or antiquarks with different colors, and mesons, built from a quark and an antiquark with opposite colors. This thesis deals with D^0 mesons that are built from charm and up quarks.

Quantum Electrodynamics (QED) is the quantum theory of the electromagnetic force. It only effects charged particles, more precisely the electric charge. The mediator is the photon.

The weak force effects all fermions via exchange of Z^0, $W^\pm$ bosons. $W^\pm$ bosons change the flavor from up-type to down-type. This is called a charged current interaction. The Z^0 bosons

act as neutral currents. In the SM there are no flavor changing neutral currents (FCNCs) due to the Glashow-Iliopoulos-Maiani (GIM) mechanism [13] in first order. Every quantum interaction has quantum loop corrections, meaning that virtual particles in particular heavier particles than the interaction's energy would allow to take part in the interaction and modify it with small corrections. So in second order calculations FCNCs are allowed processes in the SM.

Second order processes are the physics to be explored by the LHC*b* experiment. In such quantum loop corrections, there can occur particles which need much more production energy than the interaction would allow in first order. In particular famous particles like the Higgs boson or supersymmetric particles are expected to appear.

The electromagnetic and weak interactions were unified by Glashow, Weinberg and Salam in the 1960s [12, 22, 23] into one electroweak theory. To get massive weak bosons (Z^0, $W^{\pm}$) and a massless electromagnetic boson (photon) the coupling to a scalar Higgs-field is needed which is called spontaneous symmetry breaking. The Higgs field is also responsible for all fermionic mass generation as quarks and leptons get their masses via Yukawa coupling to the Higgs field. The electroweak quantum numbers are the weak isospin T, its third component T_3 and the weak hypercharge $Y = Q - T_3$, with Q being the electric charge in units of the elementary charge e. The SM is a chiral gauge theory. It treats two chiralities differently, left-handed particles are weak isospin doublets, while right-handed particles are weak isospin singlets. See table 1.3.

generation			T	T_3	Y	Q
$\begin{pmatrix}\nu_{e\mathrm{L}}\\ e_{\mathrm{L}}\end{pmatrix}$	$\begin{pmatrix}\nu_{\mu\mathrm{L}}\\ \mu_{\mathrm{L}}\end{pmatrix}$	$\begin{pmatrix}\nu_{\tau\mathrm{L}}\\ \tau_{\mathrm{L}}\end{pmatrix}$	1/2	$+1/2$ $-1/2$	$-1/2$ $-1/2$	0 -1
e_{R}	μ_{R}	τ_{R}	0	0	-1	-1
$\begin{pmatrix}u_{\mathrm{L}}\\ \mathrm{d}'_{\mathrm{L}}\end{pmatrix}$	$\begin{pmatrix}c_{\mathrm{L}}\\ s'_{\mathrm{L}}\end{pmatrix}$	$\begin{pmatrix}t_{\mathrm{L}}\\ b'_{\mathrm{L}}\end{pmatrix}$	1/2	$+1/2$ $-1/2$	$+1/6$ $+1/6$	$+2/3$ $-1/3$
u_{R}	c_{R}	t_{R}	0	0	$+2/3$	$+2/3$
d_{R}	s_{R}	b_{R}	0	0	$-1/3$	$-1/3$

Table 1.3.: Electro-Weak flavor quantum numbers of leptons and quarks. T denotes the weak isospin, T_3 is its third component, $Y = Q - T_3$ the weak hypercharge, where Q is the electric charge. The subscripts L and R indicate left- and right-handed states. Weak isospin doublets are given in brackets. The weak eigenstates d', s' and b' are related to the mass eigenstates d, s and b via the CKM matrix. [18]

The Cabibbo-Kobayashi-Maskawa (CKM) quark mixing mechanism is also a very well established ingredient of the Standard Model. The fact that mass eigenstates q are unequal to weak eigenstates q' is described by a base transformation through the CKM quark mixing matrix [5, 16],

$$\begin{pmatrix}d'\\ s'\\ b'\end{pmatrix} = V_{CKM} \begin{pmatrix}d\\ s\\ b\end{pmatrix}$$

with

$$V_{CKM} = \begin{pmatrix} V_{ud} & V_{us} & V_{ub} \\ V_{cd} & V_{cs} & V_{cb} \\ V_{td} & V_{ts} & V_{tb} \end{pmatrix} . \tag{1.1}$$

The nine entries of the CKM matrix are complex numbers each consisting of a real and an imaginary part. So in total there are 18 parameters, which can be reduced to four independent parameters by several constraints. The first condition is that the matrix is unitary, $VV^\dagger = 1$. That means an up-type quark must transform into a down-type quark under a charged current interaction, $\sum_i V_{ki}^* V_{kj} = \delta_{ij}$. This pairwise condition reduces half of the parameters so there are nine free parameters left. Therefrom five parameters are absorbed in redefining the quark fields [18]. This is possible, because the quark fields are invariant under rotations, so they can be multiplied by a phase factor $e^{i\phi}$, where the absorbed five parameters are treated like phases ϕ. Finally four parameters are left, three real rotation angles and one CP-violating phase δ, responsible for all CP-violating phenomena in flavor-changing processes within the SM [16, 18]. One of the most common parameterizations of the CKM matrix is the Wolfenstein parameterization:

$$\boldsymbol{V}_{\mathrm{CKM}} = \begin{pmatrix} 1 - \frac{\lambda^2}{2} & \lambda & A\lambda^3 (\rho - i\eta) \\ -\lambda & 1 - \frac{\lambda^2}{2} & A\lambda^2 \\ A\lambda^3 (1 - \rho - i\eta) & -A\lambda^2 & 1 \end{pmatrix} + \mathcal{O}(\lambda^4) . \tag{1.2}$$

The Wolfenstein parameters are defined as:

$$\begin{aligned} \lambda &= \frac{|V_{us}|}{\sqrt{|V_{ud}|^2 + |V_{us}|^2}} , \\ A\lambda^2 &= \lambda \left| \frac{V_{cb}}{V_{us}} \right| , \\ A\lambda^3 (\rho + i\eta) &= {V_{ub}}^* . \end{aligned} \tag{1.3}$$

Experimentally they are determined to be [19]:

$$\begin{aligned} \lambda &\approx 0.23 , \\ A &\approx 0.81 . \end{aligned} \tag{1.4}$$

The Wolfenstein parameterization points out the main quark mixing attributes of first order calculations. The diagonal entries are approximately equal to one, so quarks basically mix in their own generation. Transitions between the first and second generation are still likely, but only to a fifth part of the in-generation transitions ($\propto \lambda$). Transitions between the second and the third generation are even more unlikely ($\propto \lambda^2$) and finally transitions between the first and the third generation are the most suppressed ($\propto \lambda^3$). Concurrently these transitions between the first and third generation are the only transitions proportional to the remaining imaginary phase. So this is the only source of CP violation in the SM.

The condition of unitarity of V_{CKM} can also be used in the following way. The sum of entries in one row or column must be equal to one, visualized as triangles in the complex plane. So six

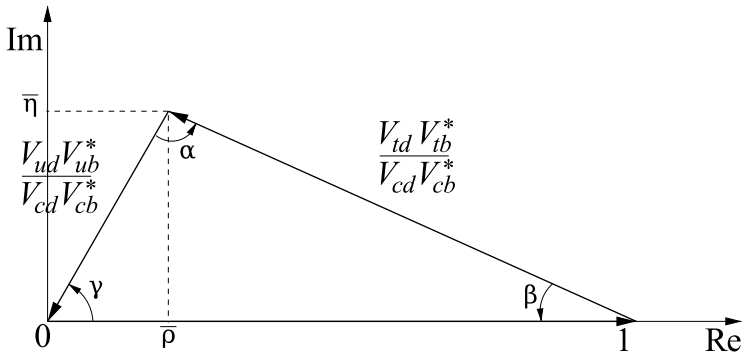

Figure 1.2.: Scheme of the unitarity triangle in the complex plane. [15]

triangles are constructible, two triangles have sides in the same order of magnitude, the other 4 are degenerated. One not degenerated triangle is for example the "b-d unitarity triangle", see in equation 1.5,

$$V_{ud}V_{ub}^* + V_{cd}V_{cb}^* + V_{td}V_{tb}^* = 0\,, \tag{1.5}$$

It can be drawn in the complex plane, see figure 1.2. The three angles in figure 1.2 are defined as counter-clockwise rotations of

$$\alpha = arg(-\frac{V_{td}V_{tb}^*}{V_{ud}V_{ub}^*})\,, \quad \beta = arg(-\frac{V_{cd}V_{cb}^*}{V_{td}V_{tb}^*})\,, \quad \gamma = arg(-\frac{V_{ud}V_{ub}^*}{V_{cd}V_{cb}^*})\,. \tag{1.6}$$

The global fit results of all CKM matrix contributing experiments are shown in figure 1.3. The SM, introduced more than 30 years ago and tested by many experiments, is a very successful theory. Up to now there is no single laboratory experiment, which observed a significant deviation from the SM. The SM CKM mechanism is presently experimentally overconstraint due to a very successful decade of measurements at the B-factories BaBar and Belle[1] and at the TeVatron[2]. Hence, the CKM mechanism, established by Makoto Kobayashi and Toshihide Maskawa, led to the Nobel prize in physics in 2008. Figure 1.3 clarifies the experimental overconstraints to this unitarity triangle. Thus, the goal of the LHC*b* experiment is not to redo these measurements of CP violation, but to perform high precision measurements in the B system and to search for deviations from the CKM-predictions, which would be an unambiguous sign of new physics at the TeV scale and above. Presently less well measured is the B_s triangle. The *b-s unitarity triangle*, shown in equation 1.7,

$$V_{us}V_{ub}^* + V_{cs}V_{cb}^* + V_{ts}V_{tb}^* = 0 \tag{1.7}$$

and the *b-d unitarity triangle*, see equation 1.5, will be measured by the LHC*b* experiment in $B_s - \bar{B}_s$, respectively $B_d - \bar{B}_d$ mixing. New physics are especially in the B_s system expected to be measured, see figure 1.4. The LHC*b* measurements of the decay frequencies Δm_s and Δm_d in the decays $B_s \to D_s 3\pi$ and $B_d \to D^-\pi^+$ have already reached competitive sensitivity. An overview

[1] e^+e^- collider running at the $Y(4S)$ resonance.
[2] Proton-Antiproton collider running at a center-of-mass energy of 1.96 TeV.

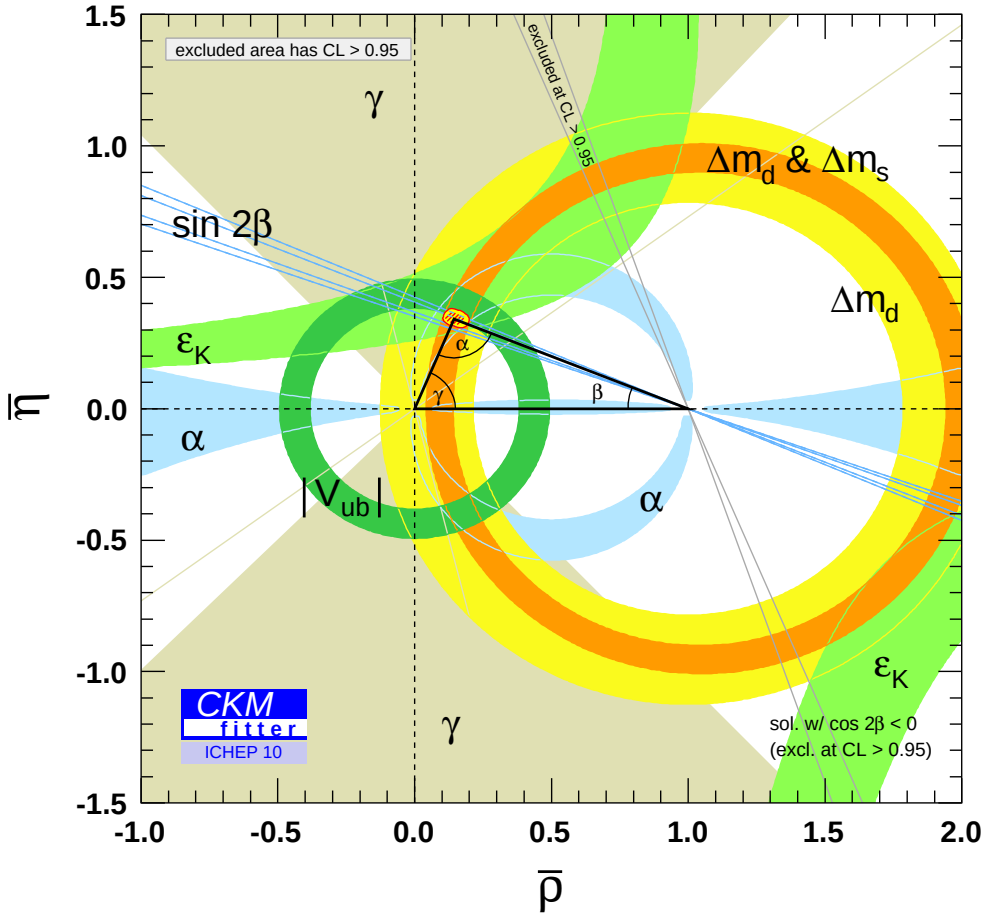

Figure 1.3.: Present CKM matrix fit results. The largest uncertainty comes from the angle γ. LHC*b* will perform a tree level measurement of this angle. [8]

of measurements of the LHC*b* physics programme, which have already reached competitive sensitivity, will be given in chapter 2.5. The entire mixing formalism will be described in chapter 3 aligned to D mixing quantities.

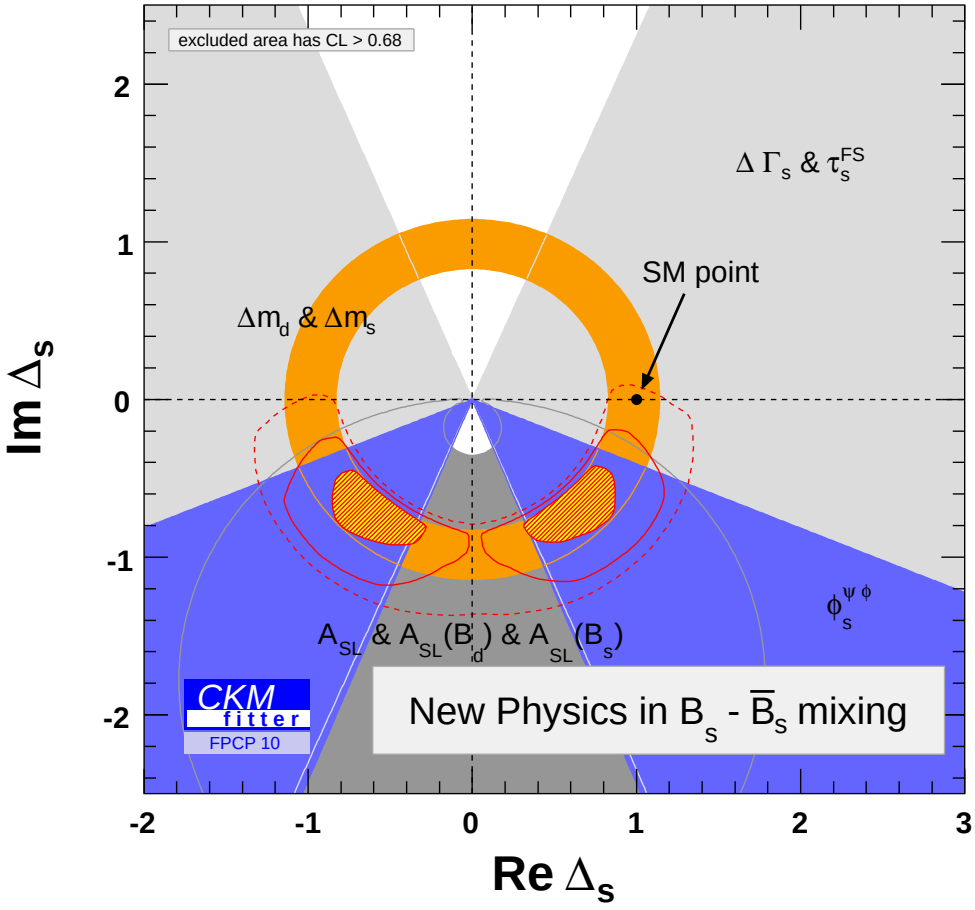

Figure 1.4.: Through precise measurements of Δm_d, Δm_s, $\Delta\Gamma_d$ and $\Delta\Gamma_s$ the additional CP violating phase Δ_s can be constraint and New Physics established. The current TeVatron measurements are included in the plot, a $1.9\,\sigma$ deviation is obtained from the SM hypothesis $\Delta_s = 1$ ($Re\Delta_s = 1, Im\Delta_s = 0$). [8]

2. LHC*b* Experiment

2.1. Large Hadron Collider

The Large Hadron Collider (LHC) is presently the most powerful particle accelerator in the world. It is hosted by the European Organization for Nuclear Research, CERN, which is situated in Geneva on the border between France and Switzerland.

The LHC has a circumference of 27 km long and runs 100 m underground. It accelerates two hadron beams of the same kind, either protons or lead ions. After a short period at a center-of-mass energy of $\sqrt{s} = 900\,\text{GeV}$ the first proton-proton collisions started in March 2010 with $\sqrt{s} = 7\,\text{TeV}$, half of the designed center-of-mass energy. On March 30^{th} 2010 the first TeV collisions took place and collision data taking at large scales began.

Four large detectors have been constructed at the LHC, namely ATLAS, CMS, ALICE and LHC*b*. ATLAS (A Toroidal LHC ApparatuS) and CMS (Compact Muon Solenoid) are large, general purpose particle detectors, searching for the Higgs boson, new heavy particles, predicted by the supersymmetric extensions of the Standard Model, and extra dimensions. ALICE (A Large Ion Collider Experiment) is specialized on the lead ion collisions, studying mainly quark-gluon plasma. The LHC*b* (Large Hadron Collider beauty) experiment investigates B-physics to perform indirect searches for new particles in high precision deviations from the Standard Model.

The LHC*b* experiment is designed to acquire data from proton-proton collisions. The proton source is hydrogen gas, that is ionized through a high electric field and stripping foils. From thermal energies the protons are accelerated to kinetic energies of 50 MeV by a linear accelerator called *LINAC2*, see figure 2.1. The first circular accelerator the protons pass through is the Proton Synchrotron Booster (PSB). Having reached a kinetic energy of 1.4 GeV the protons are injected into the Proton Synchrotron (PS). At an energy of 25 GeV they are transferred into the Super Proton Synchrotron (SPS). Finally, at an energy of 450 GeV the protons are injected in opposite directions into the two beam pipes of the LHC.

The protons are accelerated in form of bunches of up to $1.1 \cdot 10^{11}$ particles. Under nominal conditions each LHC beam has 2808 of these proton bunches with a separation in the beam pipe of about 25 ns. The nominal design energy is 7 TeV per beam. This requires a peak magnetic field of 8.33 TeV provided by superconducting magnets to keep the protons on the 27 km ring. 1232 dipole magnets keep the protons on a circular trajectory and 392 quadrupole magnets are used to ensure a well focused beam. The superconducting magnets are cooled with the help of 120 tons of superfluid helium. Besides, 8000 smaller magnets are used to fine tune the beams.

The LHC is split into eight sectors, see figure 2.2. Interaction points (IPs) are located in the center of the octants. Only four of the eight IPs are used by experiments, ATLAS is located at IP 1, ALICE at IP 2, CMS at IP 5 and LHC*b* at IP 8. The remaining four IPs are used by beam related instrumentation. Beam cleaning facilities are installed at IP 3 and IP 7. At IP

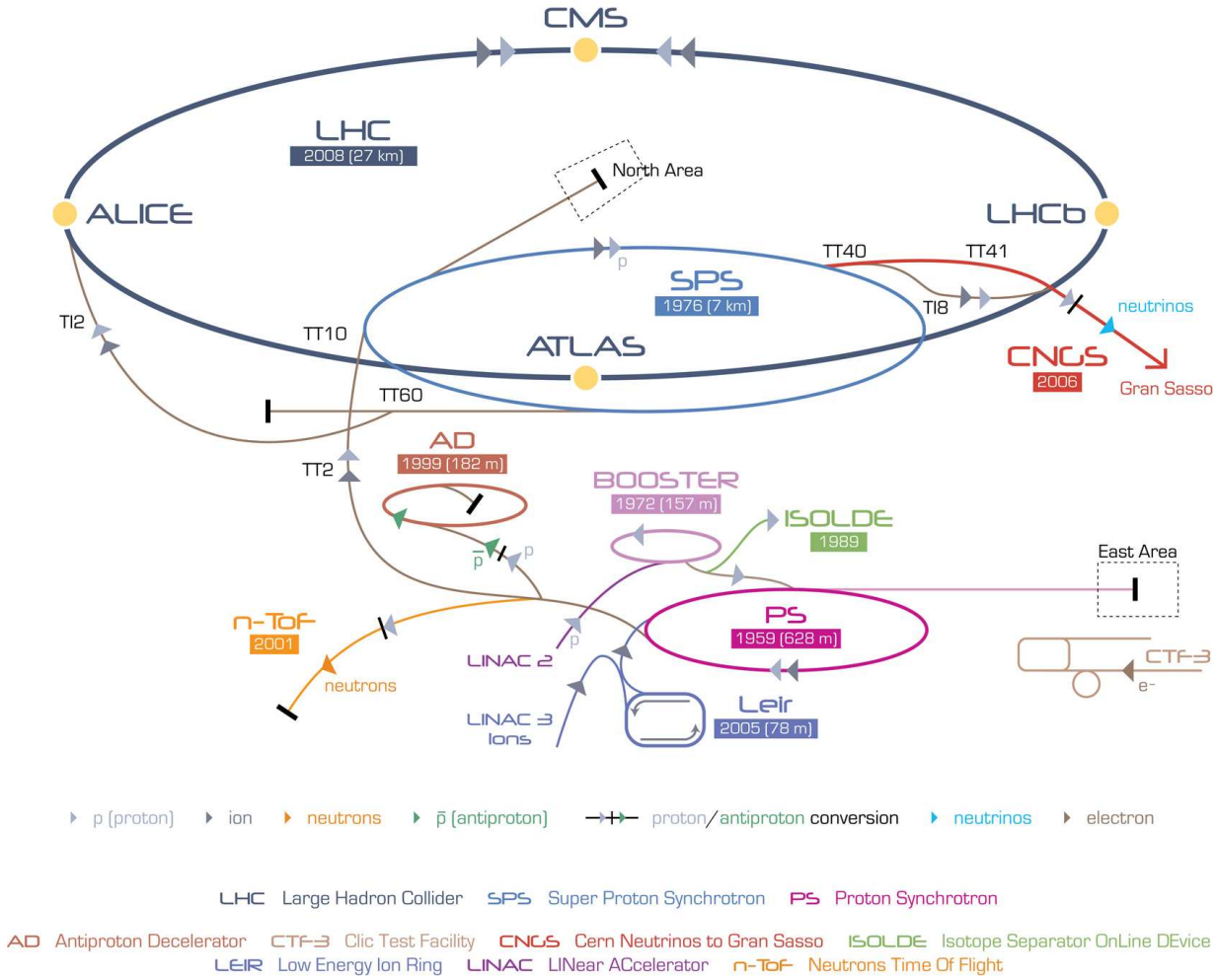

Figure 2.1.: The Large Hadron Collider (LHC) and the four main experiments: ATLAS, CMS, ALICE and LHC*b*. [7]

3 particles with large longitudinal oscillation amplitudes are removed from the beam and at IP 7 particles with large transversal oscillation amplitudes are removed. A facility to dump both beams is located at IP 6. Finally, at IP 4 high frequency cavities are located to accelerate the protons in the LHC up to the nominal energy. The cavities are superconducting and operate at a frequency of 400.8 MHz. With an energy gain per turn of 485 keV it takes the LHC only 20 minutes to reach the nominal beam energy of 7 TeV.

2.2. LHC*b* Experiment

The LHC*b* experiment is dedicated to precision measurements in the B system. At the LHC center-of-mass energy $\sqrt{s_{LHC}}$ the dominant production mechanism of $b\bar{b}$ pairs is gluon-gluon

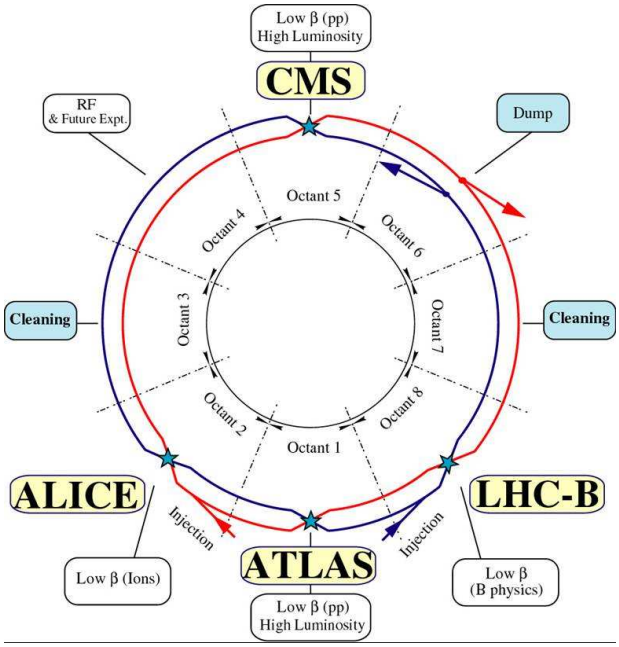

Figure 2.2.: The Large Hadron Collider (LHC) is split into eight octants. The interaction points (IPs), where the experiments are located are indicated. [17]

fusion. The b quark mass is very small compared to $\sqrt{s_{LHC}}$, so gluons from a wide momentum range contribute to their production. In this case the probability, that these gluons carry the same momentum fraction x, is very low. Different x-values mean, that the $b\bar{b}$ pairs are boosted in beam direction, see figure 2.3. Hence, both the b- and $\bar{b}$-hadrons are predominantly produced in the same forward or backward direction. Consequently, the LHCb detector is designed as a single-arm forward spectrometer in contrast to 4π-detectors like ATLAS or CMS.

The LHCb coordinate system has its origin in the nominal LHC interaction point. The z-axis follows the beam pipe of the LHC and points from the interaction point into the experiment. The x-axis is horizontal, following the ground of the cavern and points towards the outside of the LHC ring. The y-axis is perpendicular to the x- and z-axis. The LHCb dipole magnet is oriented in a way that it mainly bends in the $x - z$ plane. The total detector acceptance for B events, which means that all B daughters of the $b\bar{b}$ pairs are detected, is very large, about 25%. In the bending plane the acceptance covers from 10 to 300 mrad and in the non-bending plane from 10 to 250 mrad.

The LHCb detector consists of several subdetectors for tracking and particle identification. A schematic figure of the entire detector in the $z - y$ plane is given in figure 2.4. The tracking system consists of the VErtex LOcator (VELO), the Trigger Tracker (TT), the Inner Tracker (IT) and the Outer Tracker (OT). The particle identification system consists of the two Ring Imaging CHerenkov detectors RICH1 and RICH2, the Scintillating Pad Detector (SPD), the Pre-Shower detector (PS), the Electromagnetic CALorimeter (ECAL), the Hadronic CALorimeter (HCAL)

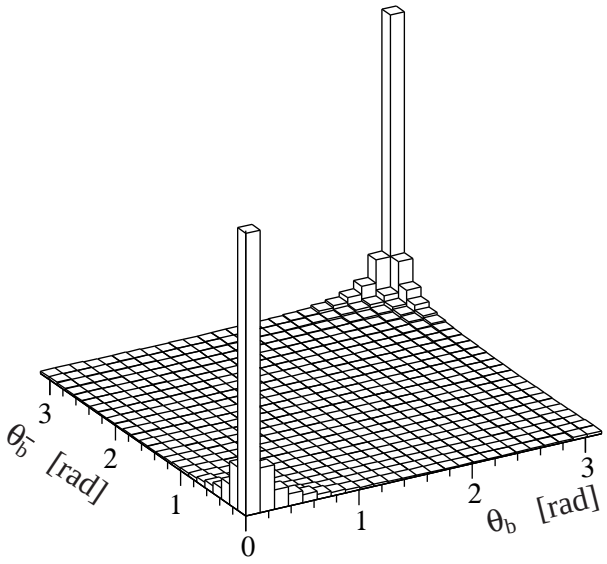

Figure 2.3.: The dominant $b\bar{b}$ pair production at the LHC*b* experiment. The angles $\Theta = 0$ denote the beam direction. $b\bar{b}$ pairs are predominantly produced in the same forward or backward direction. [26]

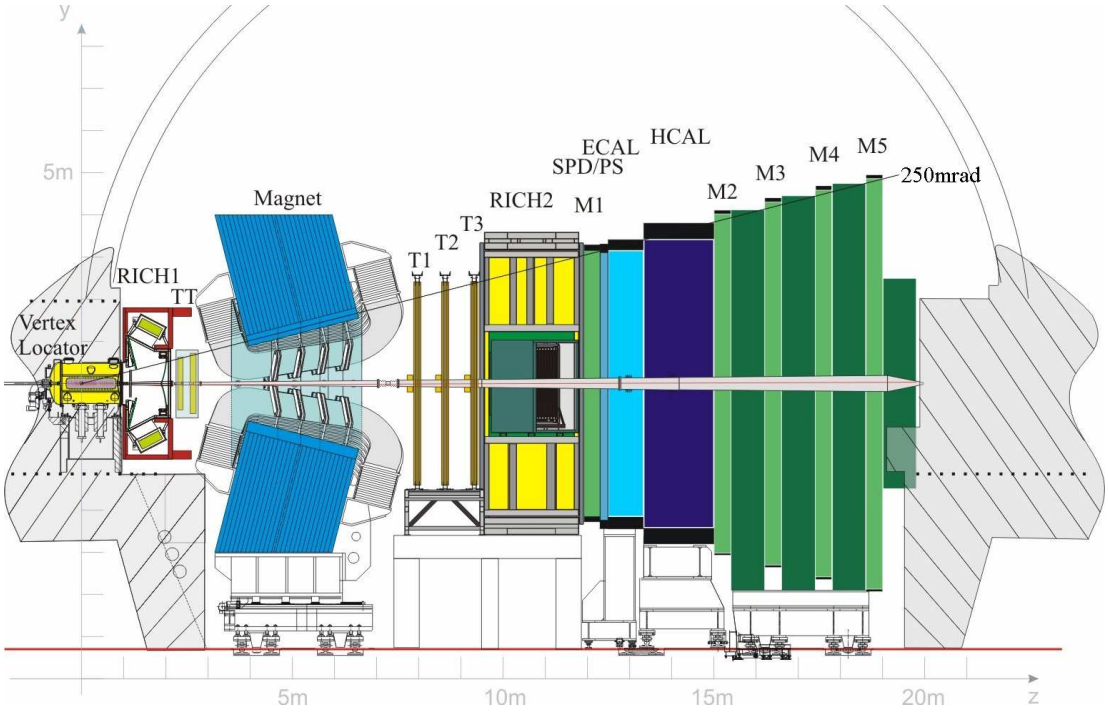

Figure 2.4.: The LHC*b* detector in the $z - y$ plane. [35]

and the five muon stations, $M_1 - M_5$. The subdetectors are briefly explained in the following. For more detailed information see [35].

2.2.1. Tracking Detectors

The main dipole magnet bends the trajectories of charged particles in its magnetic field to measure the particles momenta. The bending strength is $\int B\,dl = 4.2\,\mathrm{TM}$. By design it is large in y direction and small in x and z direction, to mainly bend particles moving in z direction in the bending plane. A special feature of the magnet is that its polarity is invertible, see figure 2.5. This allows to calibrate the tracking system very precisely. The tracking system consists of the VELO,

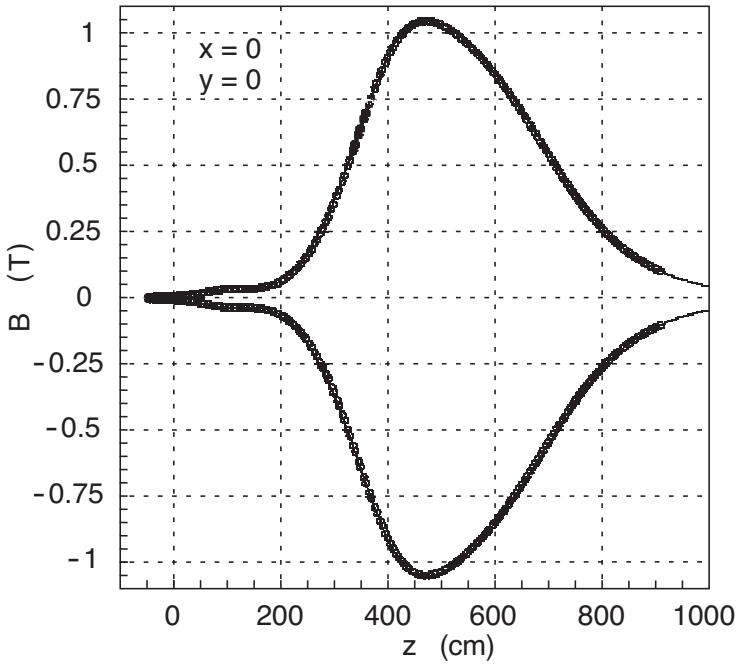

Figure 2.5.: The main magnetic field component B_y of the LHCb dipole magnet for both polarities. The VELO is positioned around 0 m, the TT around 2.5 m and the T-Stations are located between 7 and 8.5 m. [35]

the trigger tracker and the tracking stations. As an entire system it determines the momenta of the particles.

Vertex Locator

The VErtex LOcator (VELO) is positioned closest around the interaction region to precisely measure track coordinates and the displaced secondary vertices of b- and c-hadrons. It is built of 21 silicon modules each consisting of two types of silicon half disk sensors arranged along the beam direction, see figure 2.6. One type is built to measure the r-coordinate with circular strips centered around the beam axis, the other type to measure the ϕ-coordinate with radial strips.

The radial distance of the sensors to the beam is smaller than the aperture required by the LHC during injection, therefore, the VELO is not fully closed until the beam is stable. The primary vertex resolution provided by the VELO is in z-direction 60 µm and in the $x - y$ plane 10 µm. For more information about the VELO see [30].

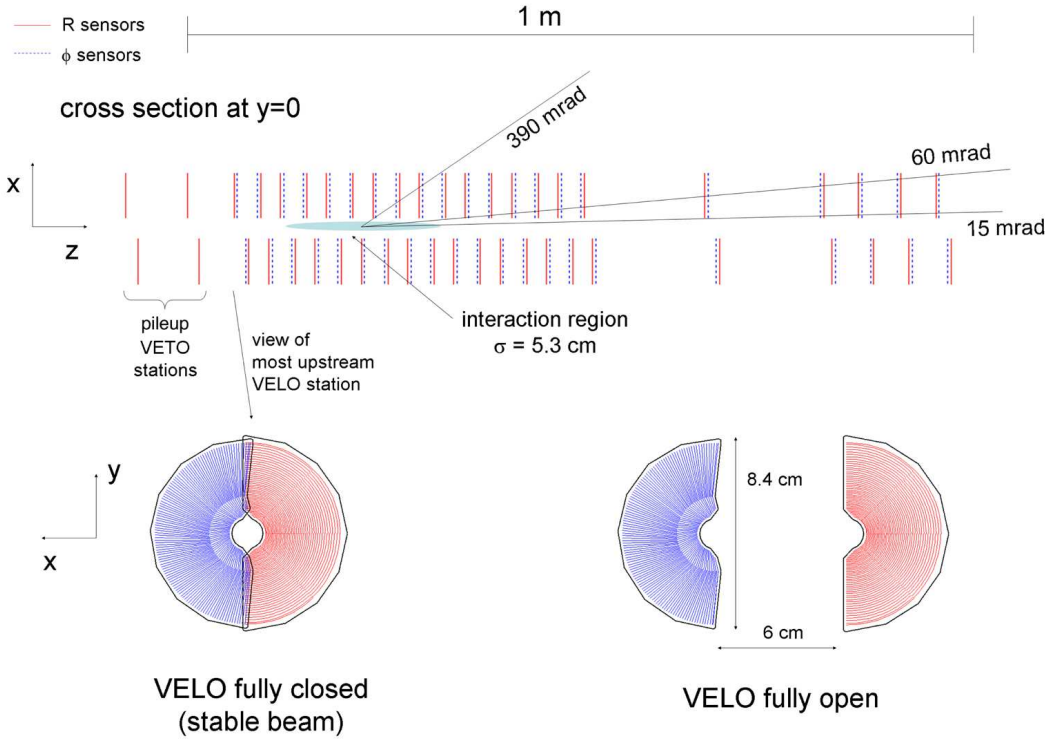

Figure 2.6.: The VErtex LOcator (VELO). A special feature of the VELO is, that it can be opened and closed. Thus it is possible to position it closest to the beam, after the injection when the beam is stable. [35]

Trigger Tracker

The Trigger Tracker (TT) is arranged directly in front of the dipole magnet, about 2 m behind the VELO. Its dimensions are 150 cm × 130 cm. It covers the full acceptance of the detector. It is built as a silicon strip detector consisting of two stations with a relative distance of 27 cm, see figure 2.7. The first station, TTa, consists of two layers called x and u. The x layer contains strips parallel to the y-axis. The u layer is rotated by the stereo angle of 5° with respect to the x layer. The second station, TTb, consists of two layers called v and x. The v layer is rotated by the stereo angle of $-5°$ with respect to the x layer. The x layer of TTb is build analogous to the x layer in TTa. This configuration allows a three dimensional track reconstruction with a good resolution (about 50 µm per single hit) in the bending plane of the magnet.

The main purpose of the TT is to reconstruct low momentum particles which are bent out of the detector by the magnet and long lived particles which decay mainly after the VELO. In addition to that the TT information also improves the momentum estimate of the T-Stations as an additional measurement in front of the magnet. For more information about the TT see [38].

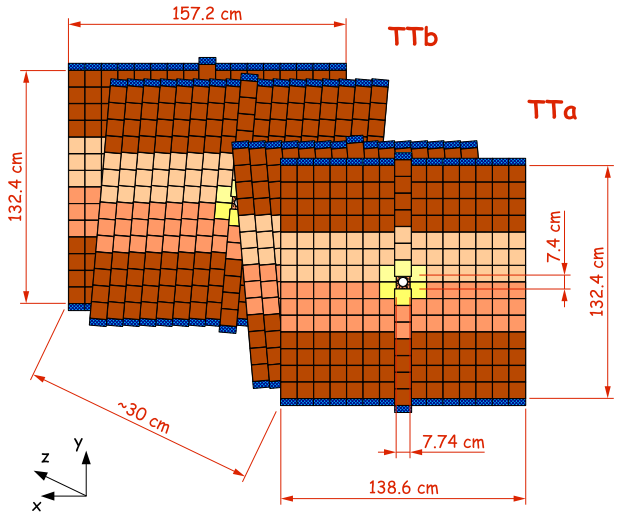

Figure 2.7.: The Trigger Tracker (TT) consisting of two stations in x and stereo layers configuration. [38]

Tracking Stations

The three Tracking Stations (T-Stations) are located behind the magnet with a size of $6\,\mathrm{m} \times 5\,\mathrm{m}$. Each station is built of two detectors, the Inner Tracker (IT), see figure 2.8, and the Outer Tracker (OT), see figure 2.9.

The IT is located directly around the beam pipe. It covers the region with the highest flux of charged particles. Similar to the Trigger Tracker the IT is also a silicon strip detector built in the x, u, v and x layer configuration provides also three dimensional tracking information with a resolution of approximately $50\,\mu\mathrm{m}$. For more information about the IT see [32].

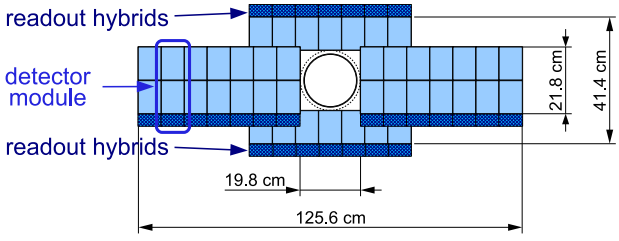

Figure 2.8.: The Inner Tracker: layout of an x detection layer in the second IT station. [35]

The OT covers the large region around the IT. It is a drift-time detector with straw tubes, filled with gas, serving as drift cells. The gas is a mixture of Argon (70%) and CO_2 (30%) that guarantees a drift time below 50 ns. A 24 µm thick gold coated tungsten anode in every straw center guarantees a drift-coordinate resolution of 200 µm. Each station is built of four layers, which are arranged in the same configuration of x and *stereo layers* as in the TT and the IT. A layer is composed of 14 long modules and 8 short modules, which are arranged around the IT. For more information about the OT see [31].

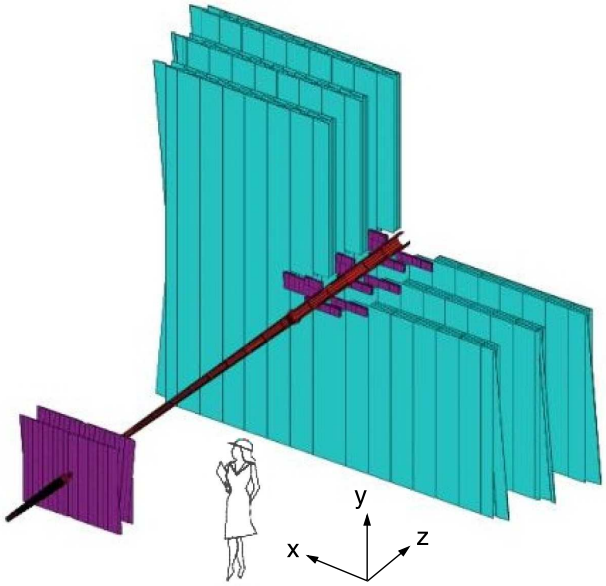

Figure 2.9.: The Outer Tracker (turquoise): Arrangement of the straw-tube modules in layers and stations. TT and IT shown in purple. [35]

2.2.2. Particle Identification Detectors

Beside a good tracking system an accurate particle identification is essential for the LHC*b* experiment. Many interesting decay channels contain only hadrons, so a good separation between kaons and pions is essential. Two Ring Imaging Cherenkov Detectors, RICH1 and RICH2, an Electromagnetic Calorimeter, ECal, a Hadronic Calorimeter, HCal, and five muon chambers, M1 – M5, built up the particle identification system. The information of this system is used to assign a relative probability for the particle hypothesis to the reconstructed particle tracks.

Ring Imaging Cherenkov Detectors RICH1 and RICH2

The RICH detectors utilize the Cherenkov effect. Charged particles passing through a medium (radiator) at a speed faster than the speed of light in that medium emit Cherenkov radiation. The light cone is radiated under a certain angle Θ_C relative to the flight direction and is connected to the velocity of the particle v, and the refractive index of the medium n through equation 2.1:

$$\cos\Theta_C = \frac{c}{nv}\,, \tag{2.1}$$

where c denotes the speed of light. The radiated photons are collected by spherical mirrors and imaged onto Pixel Hybrid Photon Detectors, located outside of the acceptance above and below the beamline. Hence, every light cone is imaged as a ring with radius r proportional to the Cherenkov opening angle Θ_C

The RICH1 detector is located between the VELO and the Trigger Tracker, so it is upstream of the magnet. It contains Aerogel and Fluorobutane (C_4F_10) gas radiators and covers a momentum range of approximately $1 - 60\,\mathrm{GeV/c}$ for particles inside the acceptance, see figure 2.10. The RICH2 detector is located between the last tracking station and the first muon station. It contains a CF_4 gas radiator and provides particle identification information for a momentum range between $15\,\mathrm{GeV/c}$ up to approximately $100\,\mathrm{GeV/c}$. Both RICH detectors are installed in areas with a low magnetic field, so that the passing tracks are not bent significantly. For more information about the RICH detectors see [29].

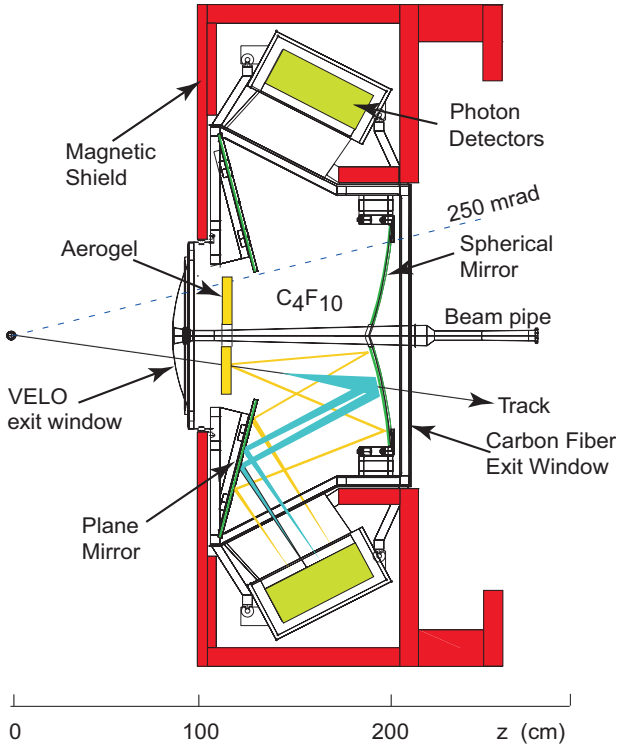

Figure 2.10.: Side view schematic layout of the RICH1 detector. [35]

Calorimeter System

The calorimeter system provides information to identify electrons, photons and hadrons and measures their energy and position. It plays an important role for the first trigger level (L0),

because it selects tracks with a certain minimum transverse energy to enable a decision 4 µs after the interaction.

Particles entering a calorimeter are decelerated until they are fully stopped. The lost energy is transformed into secondary particles. Hence, each fast incoming particle initiates a particle shower around its trajectory in the calorimeter. Leptons and photons loose their kinetic energy in the electromagnetic calorimeter by radiating bremsstrahlung. While hadrons, e.g. protons, kaons and pions are stopped in the hadronic calorimeter by strong interaction processes.

Here, the shower detection is longitudinally segmented to provide particle identification in addition to the measurement of the deposited energy. If the shower detection was segmented transversely, the direction of the incoming particles is measured instead of the particle identification. The calorimeter system is built of four elements: a single layer Scintillating Pad Detector (SPD) to differentiate between charged and neutral particles, a Pre-Shower Detector (PS) located right after a 12 mm lead wall, an Electromagnetic CALorimeter (ECAL) and a Hadronic CALorimter (HCAL).

The 15 mm lead converter, $2.5X_0$ electromagnetic (0.1λ hadronic) interaction lengths thick, is sandwiched between the SPD and the PS. It initiates an electromagnetic shower. Charged particles are detected in the SPD, while neutral particles do not leave a signal there. In this way electrons can be distinguished from photons. Both, the SPD and the PS consist of 15 mm thick scintillation pads from which the scintillation light is collected by a fiber and directed to photomultipliers outside of the acceptance. The sensitive area covers 7.6 m × 6.2 m.

The Electromagnetic CALorimeter (ECAL) is constructed in shashlik technology, which is a sampling structure of 66 alternating layers of 2 mm lead and 4 mm thick scintillator plates. This leads to a fast time response and a good radiation hardness, while the energy resolution is reasonable, see equation 2.2:

$$\frac{\sigma(E)}{E} \leq \frac{9.5\%}{\sqrt{E}} \oplus 0.8\%\,, \tag{2.2}$$

for the designed energy (E in GeV) resolution, where $\oplus$ denotes quadratic summation. In total the ECAL denotes for $25X_0$ electromagnetic interaction lengths and 1.1λ hadronic interaction lengths. It is placed 12.5 m from the interaction point.

The Hadron CALorimeter (HCAL) is a sampling device made from iron as absorbing material and scintillating tiles as active material. The light collecting fibres run parallel to the beam along the detector towards the back side to the photomultiplier tubes. In total the depth of the HCAL corresponds to 5.6λ and its weight is around 500 tons. The energy (E in GeV) resolution is, see equation 2.3:

$$\frac{\sigma(E)}{E} \leq \frac{69\%}{\sqrt{E}} \oplus 9\%\,. \tag{2.3}$$

For more information about the calorimeters see [27].

Muon system

Muon triggering and offline identification are fundamental requirements for the LHC*b* experiments. E.g. in the decay modes $B_d^0 \to J/\psi(\mu^+\mu^-)K_s^0$ and $B_s^0 \to J/\psi(\mu^+\mu^-)\phi$ muons are present in the final states. They will play a major role for CP-asymmetry measurements. The muon system

provides fast information for the high-p_T muon trigger at lowest level (L0) and muon identification for the high-level trigger (HLT) and offline analysis. It is composed of five stations (M1-M5) of rectangular shape, placed along the beam axis, see figure 2.11. M1 is located in front of the

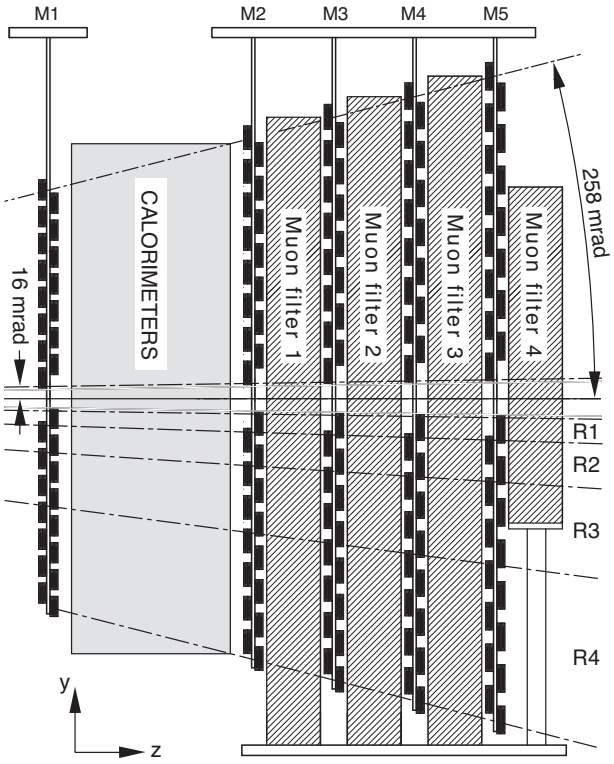

Figure 2.11.: Side view of the muon system. The first muon station is located in front of the calorimeters. The other four muon stations are located directly behind the calorimeters, separated by muon filters. [35]

calorimeter system to improve the momentum measurement, while M2 to M5 are directly behind it and are separated by 80 cm thick iron filters, corresponding to a total of 20 hadronic interaction lengths, to shield them from hadrons. An additional iron absorber is placed behind M5 to shield the system from muon coming from the opposite direction. To pass all five chambers a muon is required to have a minimum momentum of around 6 GeV. The chambers are composed of multi-wire proportional chambers (MWPC) and gas electron multipliers (GEM) in the inner part. The muon system covers a total area of 435 m^2 which corresponds to an acceptance of about 20% for muons from inclusive b semileptonic decays. For more information about the muon system see [28].

Particle Hypothesis

With the measurement of the Cherenkov opening angle Θ_C from the RICH detectors and the momentum (p) from the tracking system a mass (m) hypothesis can be made using equation 2.4:

$$\cos\Theta_C = \sqrt{1 + \left(\frac{m}{p}\right)^2}. \tag{2.4}$$

Additional information from the muon chambers and the calorimeter system is used to calculate a likelihood value $\mathcal{L}(X)$ for the mass hypothesis of the particle X. This likelihood value is then compared to the likelihood value of a pion $\mathcal{L}(\pi)$. Finally a relative particle hypothesis ("delta log-likelihood") is computed, equation 2.5:

$$\Delta\mathcal{L}_{X\pi} = \ln\mathcal{L}(X) - \ln\mathcal{L}(\pi) = \ln\frac{\mathcal{L}(X)}{\mathcal{L}(\pi)} \tag{2.5}$$

If $\Delta\mathcal{L}_{X\pi} > 0$, the reconstructed track corresponds more likely to the particle of type X than to a pion, and vice versa.

2.3. LHC*b* Trigger

At the LHC collider the proton bunches cross with a rate of $40MHz$. The rate of inelastic pp-collisions dependents on how strongly the beams are focused during collisions. This is called the instantaneous luminosity. For LHC*b* the nominal value is $2 \cdot 10^{32} cm^{-2} s^{-1}$ [26]. At the nominal luminosity, about 45% of the bunch crossings lead to an elastic or inelastic proton-proton interaction. For LHC*b* the rate of visible interactions, interactions with at least five tracks in the acceptance of the detector, is then 14 MHz. The trigger system consists of two main parts, the Level 0 hardware trigger getting its decision input from the pile-up system, the calorimeters and the muon system, and the High Level Trigger (HLT), which is a software trigger getting its decision input from the full detector information, see figure 2.12.

2.3.1. Level 0 Hardware Trigger

The Level 0 (L0) hardware trigger reduces the collision rate of 14 MHz to 1.1 MHz. At this rate the entire detector will be read out. The input of the L0 decision unit is made of three parts, the VELO Pile-Up System, the Calorimeters Triggers and the Muon Triggers. The Pile-Up System vetoes crossings with multiple visible interactions against the crossings with single interactions. So it provides the information about the position of the primary vertex candidates along the beam-line and a measure of the total backward charged track multiplicity.

Due to their large mass, B meson decays often produce particles with large transverse momentum p_T and energy E_T respectively. So the L0 trigger attempts to reconstruct the highest E_T hadron, electron and photon clusters in the calorimeters and the two highest p_T muons in the muon chambers. Typical thresholds for triggering are: HCAL having at least one cluster with $E_T^{\text{hadron}} > 3.5\,\text{GeV}$, ECAL with $E_T^{e,\gamma,\pi^0} > 2.5\,\text{GeV}$, or a muon candidate in the muon chambers with $p_T^{\mu} > 1.2\,\text{GeV}$, or two muons with $p_T^{\mu_1} + p_T^{\mu_2} > 1.0\,\text{GeV}$. The L0 trigger has a total latency, the

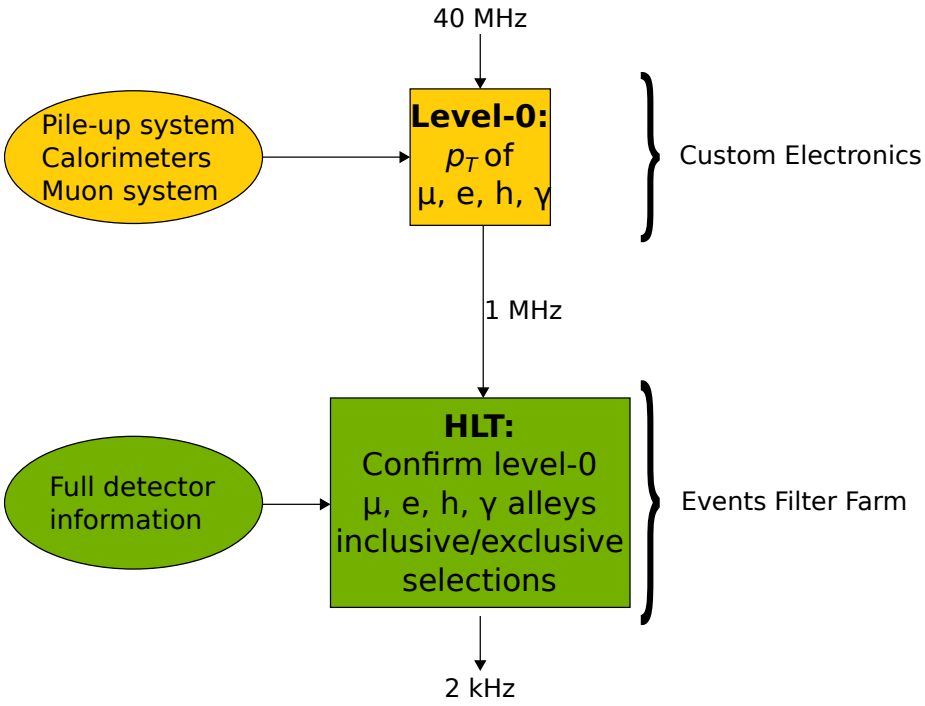

Figure 2.12.: The LHCb Trigger system. [35]

time elapsed between a pp interaction and the arrival of the L0 trigger decision at the front-end electronics, fixed to 4 µs. Including the time-of-flight of the particles, cable delays and all delays in the front end electronics this latency leaves 2 µs for the processing of the data in the L0 trigger to derive a decision.

2.3.2. High Level Trigger

The High Level Trigger (HLT) is a software trigger. It reduces the 1.1 MHz rate to a 2 kHz rate. This is done within two steps, the HLT1 goes down to 30 kHz and the HLT2 to the final output rate, see figure 2.13.

The HLT1 reduces the input rate obtained from L0 by a factor of ~ 20 by searching for a single track with high momentum, a large impact parameter with respect to all primary vertices in the event and good tracking quality. The reconstruction software, used by the HLT1, differs from the final analysis reconstruction software in precision and time consumption. It takes ~ 15 ms to process a L0 accepted minimum bias event and has a retention rate of $\sim 5\%$ on these events.

The remaining events, corresponding to a rate of 30 kHz, are then filtered by the HLT2. At this rate it is possible for the HLT2 to perform a reconstruction that is very similar to what is done offline. Event-selection criteria are used, that are in line with those used in offline analyses. Every analysis approach releases its own HLT2 trigger line, to preselect its own candidates. The online trigger decision is then the logical OR of all these lines. For more information on the trigger in general see [33].

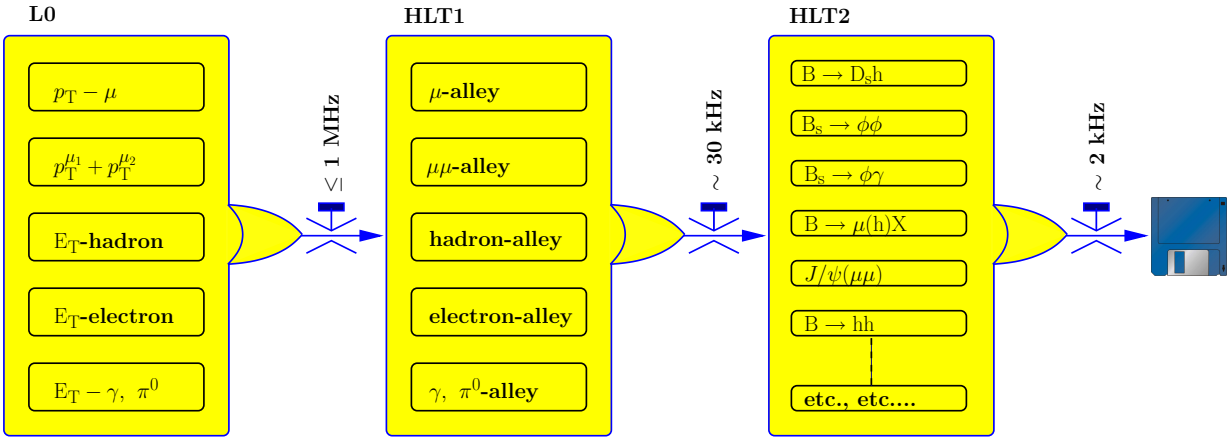

Figure 2.13.: The LHCb Trigger system workflow. [35]

2.4. LHCb Software Environment

All applications are based on the Gaudi framework [2]. The LHCb data processing applications are shown in figure 2.14. The full generation and simulation of Monte Carlo events is done in the

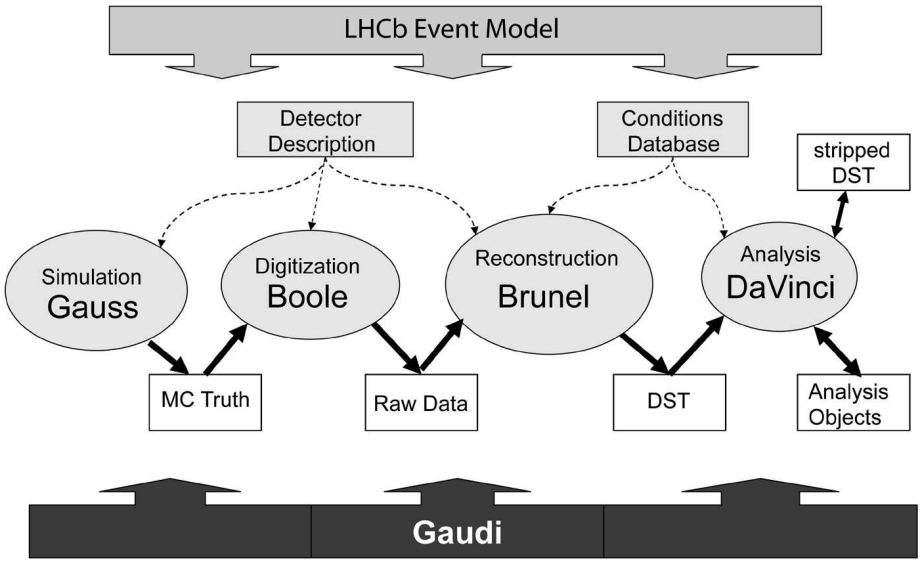

Figure 2.14.: The LHCb data processing applications and data flow. [9]

software framework Gauss [4]. In detail, the event generation of proton-proton collisions is done by PYTHIA [24] and the decaying of the B (and charmed) mesons in channels of interest is simulated by EvtGen [21]. The simulation, that means the propagation of the particles through the LHCb detector including all physical processes and material interactions, produced in the proton-proton interaction, is done by GEANT4 [10]. So the software framework Gauss mimics what will happen in the detector to understand the experimental conditions and the detector performance. The

simulation should be as close as possible to real data, hence, running conditions, e.g. event pileup due to the special luminosity the experiment will run at, are also simulated. To understand the detector for each particle a collection of associated hits and the entire detector response are stored. Afterwards, the digitization of the simulated events is done by Boole [9]. It transforms the simulated hits into a format, which is equivalent to the detector output from real data taking. This is very detector specific. After the digitization real data and simulated data are processed in the same way. Additionally, simulated data is linked to Monte Carlo truth information, which in the end allows to access the full history of a particle.

The event reconstruction is done by Brunel [9]. On this stage algorithms for track finding and particle identification are processed. The produced output files contain all reconstructed items, such as calorimeter clusters, tracks and information on particle identification from the RICH, calorimeter and muon subsystems. The final analysis is done in DaVinci [9]. Particle hypotheses are assigned to reconstructed tracks. These tracks are combined to reconstruct vertices of decayed particles. The full detector information is used to reconstruct the whole physics scenario, that has happened after the proton-proton interaction. For detailed information about the software environment see [34].

2.5. LHC*b* Physics Programme

The SM has been introduced more than 30 years ago. It is an extremely successful theory, because up to now it is consistent with all measurements at collider experiments. However, some (cosmological) observations cannot be explained: First, gravitation is not included in the SM at all. There is a graviton boson expected, but due to its softness on small scales the gravitation is always negligible at collider experiments like the LHC. Second, dark matter and dark energy are predicted by cosmology. Observations have shown that SM particles only are not sufficient to explain the structure of our universe. Third, baryon asymmetry is clearly visible in the excess of matter over antimatter in the universe. The SM can explain CP violation, but the predicted frequency is too small to explain the universe's baryon asymmetry.

The LHC was built to find first evidence for a physics theory beyond the SM called "New Physics", which would be able to explain dark matter and baryon asymmetry, e.g. by discovering supersymmetric particles. Additionally the Higgs boson, the last non confirmed building block of the SM, should be found. Two approaches are followed to measure the signatures of New Physics. Direct searches for real particles are covered by the multi-purpose experiments ATLAS and CMS. While searches for indirect effects by virtual particles which appear in loop processes are covered by the LHC*b* experiment. The advantage of the indirect search is, that very high energies can be probed due to the virtuality of loop particles. In order to observe New Physics via loop processes, these quantum corrections have to be of the same order of magnitude as the SM processes. This is the case for branching ratios of rare decays or CP violating phases in mixing processes.

Detailed information about the key measurements of the LHC*b* experiment, which are expected to give the first significant results, can be found in [37]. A short excerpt of these measurements, which have already reached competitive sensitivity on 2010 data, is given in the following paragraphs.

2.5.1. Measurement of Rare $B_s \to \mu^+\mu^-$ Decays

In flavor-changing $b \to s$ transitions New Physics effects can be large. Within the SM Flavor Changing Neutral Currents (FCNC) occur through loop corrections.

The measurement of the decay $B_s^0 \to \mu^+\mu^-$ could show a clear indication of New Physics and/or constrain the parameter space of models describing physics beyond the SM. The SM $B_s^0 \to \mu^+\mu^-$ decay is shown in figure 2.15 (a). One possible extension of the SM is the Minimal Supersymmetric Standard Model (MSSM). Within the MSSM the branching ratio of this decay is known to increase as the sixth power of the ratio of Higgs vacuum expectation values, $\tan\beta$. In figure 2.15 (b) an example of a "Higgs Penguin" contribution ($\sim \tan^6\beta$), possible in the MSSM, is shown.

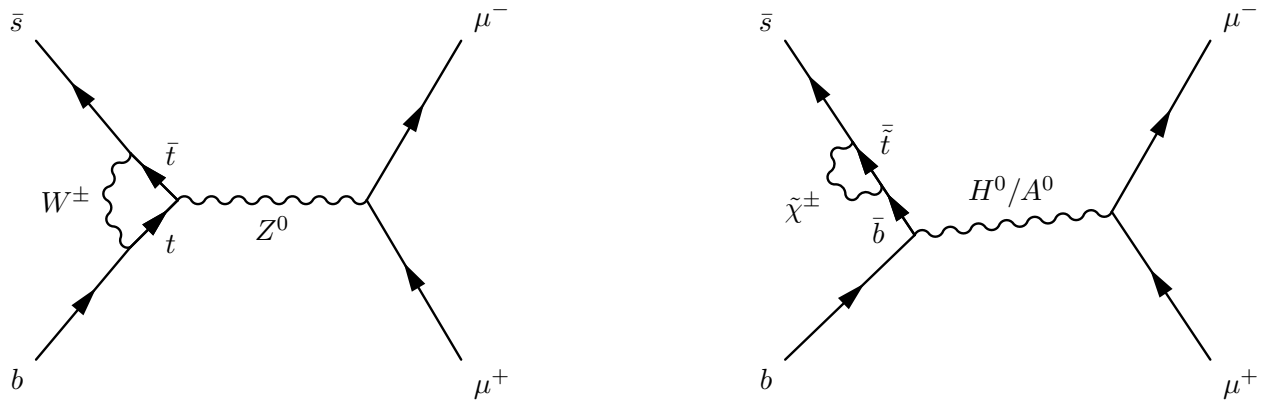

(a) SM $B_s^0 \to \mu^+\mu^-$ decay

(b) MSSM $B_s^0 \to \mu^+\mu^-$ decay

Figure 2.15.: Feynman diagrams contributing to the rare decay $B_s^0 \to \mu^+\mu^-$ in the SM via FCNC (a) and the MSSM via a "Higgs Penguin" (b).

The LHC*b* experiment has already reached sensitivity similar to the best existing limits for the very rare decays $B_s^0 \to \mu^+\mu^-$ and $B^0 \to \mu^+\mu^-$ on $37\,\text{pb}^{-1}$ of data, taken in 2010, see [39]. The invariant mass of the two final state muons is shown as a data Monte Carlo comparison in figure 2.16. The observed events are compatible with the background expectations, and the upper limits are evaluated to be:

$$\mathcal{B}(B_s^0 \to \mu^+\mu^-) < 54 \times 10^{-9}\,@\,\text{CL} = 95\% \tag{2.6}$$

The LHC*b* measurement also shows, that LHC*b* can explore the region of branching ratios at the $\sim 10^{-8}$ level with the data the LHC will deliver in 2011.

2.5.2. Measurement of the Mixing Frequencies Δm_s and Δm_d

Due to the CKM quark mixing mechanism there are two mass eigenstates for B mesons, a lighter and a heavier one. The mixing formalism will be discussed in detail in chapter 3, here, only the mass difference Δm between the lighter and the heavier mass eigenstates is necessary. It gives a

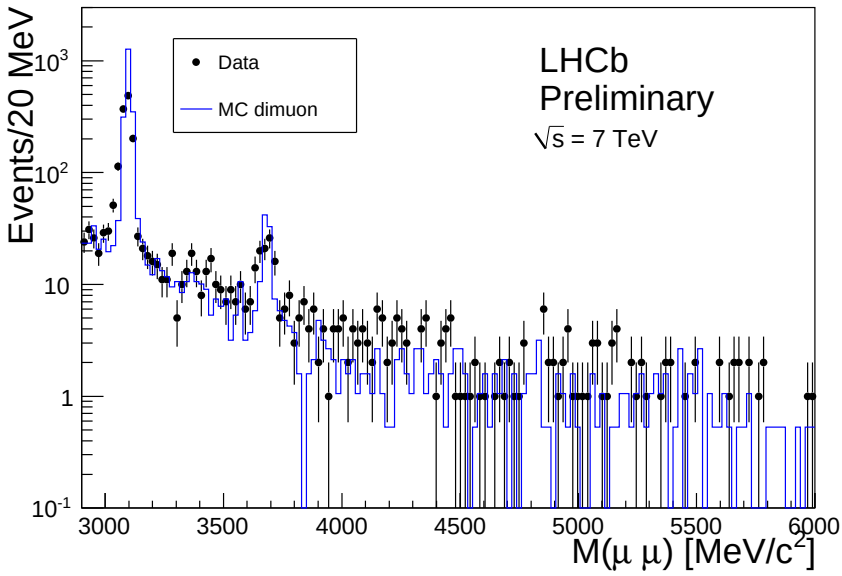

Figure 2.16.: The invariant mass of two muons produced in the very rare decay $B_s^0 \to \mu^+\mu^-$ in LHC*b* data and Monte Carlo. [36]

measure on the mixing frequency. The proper time distribution of mixing mesons is proportional to a $\cos(\Delta m_q t)$ term, q can be a s quark or a d quark. Hence, the mixing frequency Δm_q can be extracted of a fit to the proper time distribution of the B_q, if the production and the decay flavor of every single B_q is known. The decay flavor of the B_q corresponds to the final states' flavor, while the production flavor of the B_q has to be measured by dedicated flavor taggers.

The LHC*b* experiment has already performed two mixing frequency analyses on $35\,\mathrm{pb}^{-1}$ of data, taken in 2010, which have reached competitive sensitivity. The $B_s^0 - \bar{B}_s^0$ mixing frequency Δm_s is measured in a blinded analysis, see [41]. About 1400 B_s^0 candidates are reconstructed in $B_s \to D_s(3)\pi$ decays. The average proper time resolution is measured with $36 - 44\,\mathrm{fs}$. The observed mixing frequency is given in equation 2.7.

$$\Delta m_s = 17.63 \pm 0.11(\mathrm{stat.}) \pm 0.04(\mathrm{syst.})\mathrm{ps}^{-1} \tag{2.7}$$

The current world average value of Δm_s [19] is given in equation 2.8.

$$\Delta m_s = 17.77 \pm 0.10(\mathrm{stat.}) \pm 0.07(\mathrm{syst.})\mathrm{ps}^{-1} \tag{2.8}$$

The $B_d^0 - \bar{B}_d^0$ mixing frequency Δm_d is measured in a blinded analysis, see [40]. About 6000 B^0 candidates are reconstructed in $B^0 \to D^-\pi^+$ decays. The observed mixing frequency is given in equation 2.9.

$$\Delta m_d = 0.499 \pm 0.032(\mathrm{stat.}) \pm 0.003(\mathrm{syst.})\mathrm{ps}^{-1} \tag{2.9}$$

The current world average value of Δm_d [19] is given in equation 2.10.

$$\Delta m_s = 0.507 \pm 0.005\mathrm{ps}^{-1} \tag{2.10}$$

2.5.3. Measurement of CP Violation in the B Meson System

Another key measurement of the LHC*b* experiment is the CP violating phase $\Phi_s^{J/\psi\phi}$ in $B_s^0 \to J/\psi\phi$ decay. In first order Standard Model theory the B_s^0 and the $\bar{B}_s^0$ both decay into the same final state $J/\psi\phi$, shown in figure 2.17.

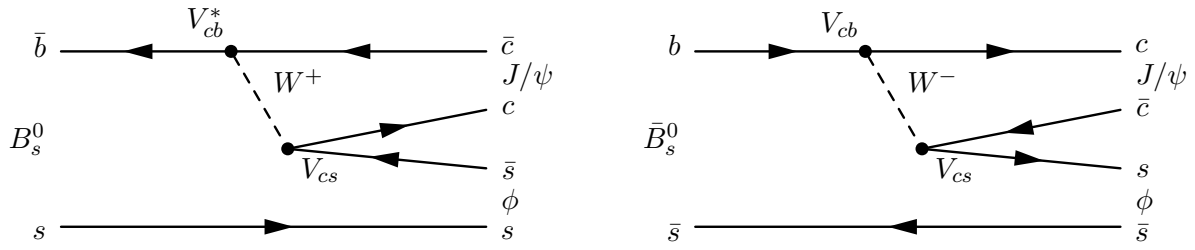

(a) $B_s \to J/\psi\phi$ (b) $\bar{B}_s \to J/\psi\phi$

Figure 2.17.: Dominant decays: (a) $B_s^0 \to J/\psi\,\phi$, (b) $\bar{B}_s^0 \to J/\psi\,\phi$.

Before the B meson decays it can mix into its anti-meson and vice versa, see figure 2.18.

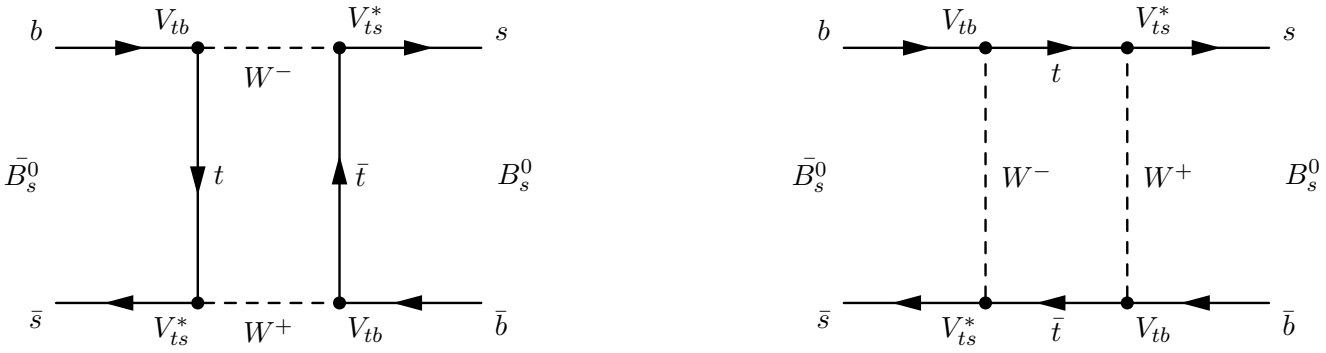

Figure 2.18.: Box diagrams for $B_s^0 - \bar{B}_s{}^0$ mixing.

A detailed description of the CP violation in the D meson system will be discussed in chapter 3, so here are only given very few keywords about the B meson system. The B_s^0 is a pseudo-scalar meson, it has total spin 0 and odd parity ($J^p = 0^-$), whereas the final state consists of two vector mesons, having a total spin of 1 and odd parity ($J^p = 1^-$). Due to the angular momentum conservation the final state is a superposition of three possible states with a relative orbital angular momentum $l = 0, 1, 2$ between the vector mesons. The CP eigenvalue depends on the relative angular momentum of the final state: The CP-odd final state is obtained for $= 1$, the CP-even state for $= 0, 2$. The CP-even and -odd final states can be statistically disentangled by an angular analysis.

The B_s^0 meson can directly decay into $J/\psi\phi$ or first oscillate into a $\bar{B}_s{}^0$ meson and then decay. The interference between direct B_s^0 decays or decays via $B_s^0 - \bar{B}_s^0$ oscillation gives rise to a CP

violating phase $\phi_s^{J/\psi\phi}$. An angular and time dependent analysis can extract this CP violating phase $\phi_s^{J/\psi\phi}$.

The first order SM prediction for the CP violating phase is given in equation 2.11.

$$\Phi_s^{J/\psi\phi} = -2\beta_s \,, \tag{2.11}$$

where β_s is the smallest angle of the "b-s unitarity triangle", given in equation 2.12.

$$\beta_s = arg\left(-\frac{V_{ts}V_{tb}^*}{V_{cs}V_{cb}^*}\right) \tag{2.12}$$

The theoretical uncertainties for the CP violating phase within the SM are very small, thus it is a good probe for New Physics contributions to the SM. The indirect measurement via global fits to data gives [8], see equation 2.13:

$$2\beta_s = 0.0360\,^{+0.0020}_{-0.0016} \tag{2.13}$$

The sensitivity of LHCb to $\phi_s^{J/\psi\phi}$ is shown in figure 2.19

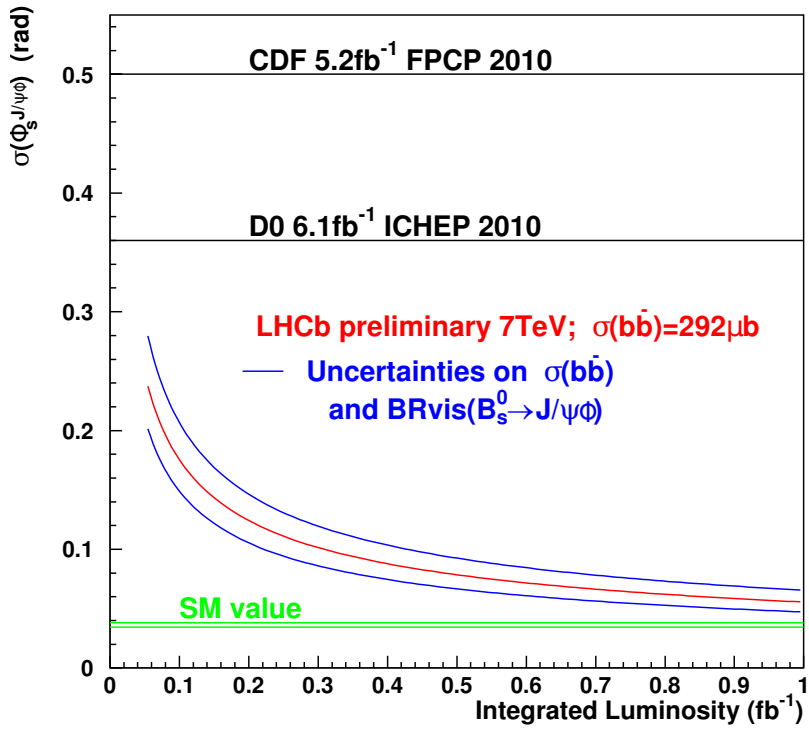

Figure 2.19.: The sensitivity to $\phi_s^{J/\psi\phi}$ of the LHCb experiment (red line) versus the integrated luminosity. The uncertainties due to the $b\bar{b}$ cross-section and the visible branching ratio of $B_s \to J/\psi(\mu^+\mu^-)\phi(KK)$ are shown as blue band. The black line shows the expected sensitivity from the TeVatron experiments. [36]

3. $D^0 - \bar{D}^0$ Mixing

D^0 Mesons are non stable particles, they decay after a certain lifetime via the weak interaction, see figure 3.1(a). Additionally there is a certain probability, that a D^0 meson mixes into an $\bar{D}^0$ meson before it decays, see for example figure 3.1(b). This is called flavor oscillation. The D^0 meson switches between the D^0 and $\bar{D}^0$ states back and forth.

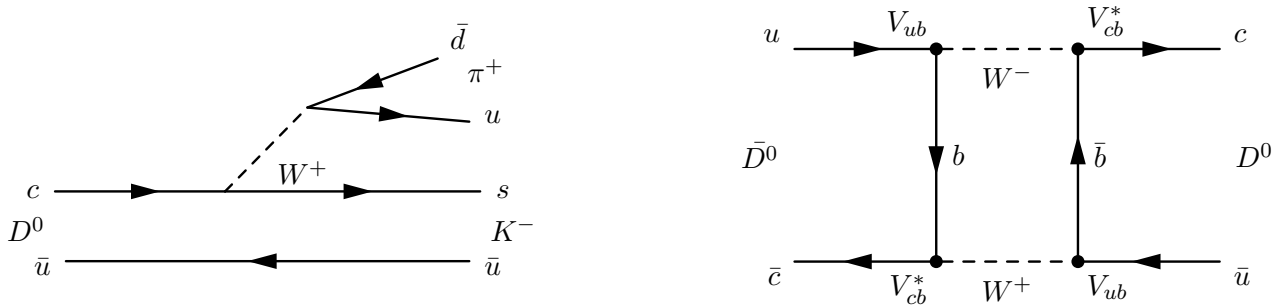

(a) Meson decay

(b) Meson mixing

Figure 3.1.: (a) D^0-meson decay and (b) $\bar{D}^0 - D^0$ mixing.

3.1. General Mixing Formalism

The D^0, $\bar{D}^0$ flavor eigenstates ($|D^0\rangle$, $|\bar{D}^0\rangle$) are associated with charm and up quarks as depicted in equation 3.1:

$$|D^0\rangle \sim |c\bar{u}\rangle\,, \quad |\bar{D}^0\rangle \sim |\bar{c}u\rangle\,. \tag{3.1}$$

These eigenstates are linked through CP transformation, see equation 3.2. C stands for charge conjugation, flipping the sign of the electric charge, and P for parity transformation, flipping the signs of the spacial coordinates.

$$CP|D^0\rangle = -|\bar{D}^0\rangle\,, \quad CP|\bar{D}^0\rangle = -|D^0\rangle \tag{3.2}$$

Flavor eigenstates can now be expressed as CP eigenstates, see equation 3.3:

$$|D^0_{\text{CP even}}\rangle = \frac{1}{\sqrt{2}}(|D^0\rangle - |\bar{D}^0\rangle)\,, \quad |D^0_{\text{CP odd}}\rangle = \frac{1}{\sqrt{2}}(|D^0\rangle + |\bar{D}^0\rangle)\,. \tag{3.3}$$

If time t is much larger than the typical strong interaction scale, the time evolution of combinations of flavor eigenstates $a|D^0\rangle + b|\bar{D}^0\rangle$ can be described by an effective Schrödinger equation,

equation 3.4:

$$i\frac{\partial}{\partial t}\begin{pmatrix} a(t) \\ b(t) \end{pmatrix} = \mathcal{H}\begin{pmatrix} a(t) \\ b(t) \end{pmatrix}, \tag{3.4}$$

with the 2×2 effective Hamiltonian, see equation 3.5:

$$\mathcal{H} = M - \frac{i}{2}\Gamma \tag{3.5}$$

and M, Γ Hermitian 2×2 matrices, respectively. The CPT theorem states that $m(D^0) = m(\bar{D}^0)$ and $\tau(D^0) = \tau(\bar{D}^0)$. Hence, the diagonal elements of $\mathcal{H}$ correspond to flavor conserving transitions $D^0 \to D^0$ and $\bar{D}^0 \to \bar{D}^0$, with $M_{11} = M_{22}$ and $\Gamma_{11} = \Gamma_{22}$, while off-diagonal elements correspond to flavor changing transitions $D^0 \leftrightarrow \bar{D}^0$, satisfying $M_{12} = M_{21}^*$ and $\Gamma_{12} = \Gamma_{21}^*$. So these elements are important for the mixing and CP violation discussion.

The eigenvectors of the Hamiltonian are mass-eigenstates (L for light, H for heavy), see equation 3.6. These are the meson states that can be observed.

$$|D_L\rangle = p|D^0\rangle + q|\bar{D}^0\rangle\,, \quad |D_H\rangle = p|D^0\rangle - q|\bar{D}^0\rangle\,, \tag{3.6}$$

with p and q being complex parameters, specifying the components of the flavor eigenstates and obeying the normalization condition, equation 3.7:

$$|p|^2 + |q|^2 = 1\,. \tag{3.7}$$

The mass difference ΔM and the width difference $\Delta\Gamma$ between the mass eigenstates are defined by equation 3.8:

$$\Delta M = M_H - M_L\,, \quad \Delta\Gamma = \Gamma_L - \Gamma_H \tag{3.8}$$

Hence, the average mass M and width Γ can be written as, see equation 3.9:

$$M = \frac{M_H + M_L}{2}\,, \quad \Gamma = \frac{\Gamma_L + \Gamma_H}{2} \tag{3.9}$$

For $D^0 - \bar{D}^0$ mixing the dimensionless variables x, y are commonly used, see equation 3.10:

$$x = \frac{\Delta M}{\Gamma}\,, \quad y = \frac{\Delta\Gamma}{2\Gamma}\,. \tag{3.10}$$

The mass difference ΔM between the mass eigenstates originates from the SM first order box diagrams, while the width difference $\Delta\Gamma$ originates from long range contributions, that are intermediate hadron states during the mixing process, see figure 3.2.

Solving the Schrödinger equation for eigenvalues of $\mathcal{H}$ allows to link the ratio q/p to the off-diagonal matrix elements $M_{1,2}$ and $\Gamma_{1,2}$ and to describe the time evolution of the D^0 and $\bar{D}^0$ mesons, see equation 3.11:

$$\left|\frac{q}{p}\right| = -\sqrt{\frac{2M_{12}^* - i\Gamma_{12}^*}{2M_{12} - i\Gamma_{12}}}\,. \tag{3.11}$$

If $\frac{q}{p} \neq 1$, the transition probability of $D^0 \to \bar{D}^0$ is unequal to that of $\bar{D}^0 \to D^0$, hence, the CP symmetry is violated by the mixing process.

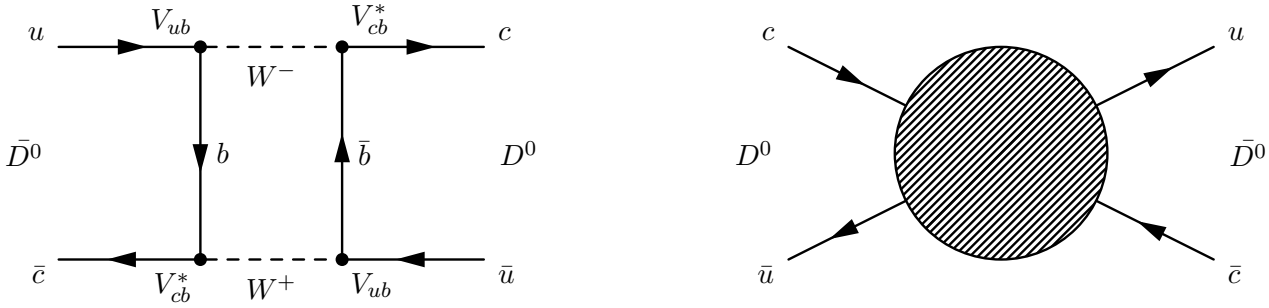

(a) SM short range contribution

(b) SM long range contribution

Figure 3.2.: D mixing (a) first order SM short range contributions causing the mass difference ΔM between the mass eigenstates (b) first order SM long range contributions causing the width difference $\Delta\Gamma$. The central blob denotes intermediate hadron-hadron states, e.g. K^+K^-, $\pi^+\pi^-$, $K^+\pi^-$, $\pi^+\pi^-\pi^0$.

The state of an initially pure $|D^0\rangle$, $|\bar{D}^0\rangle$ develops after an elapsed proper time t to $|D^0_{phys}(t)\rangle$, $|\bar{D}^0_{phys}(t)\rangle$, using the effective Hamiltonian approximation, see equation 3.12 and equation 3.13:

$$|D^0_{phys}(t)\rangle = g_+(t)|D^0\rangle - \frac{q}{p}g_-(t)|\bar{D}^0\rangle\,, \tag{3.12}$$

$$|\bar{D}^0_{phys}(t)\rangle = g_+(t)|\bar{D}^0\rangle - \frac{q}{p}g_-(t)|D^0\rangle\,, \tag{3.13}$$

where the time dependence is put into the coefficient $g_\pm$, see equation 3.14:

$$g_\pm = \frac{1}{2}(e^{-im_H t-\frac{1}{2}\Gamma_H t} \pm e^{-im_L t-\frac{1}{2}\Gamma_L t})\,. \tag{3.14}$$

If the D^0 ($\bar{D}^0$) meson decays into a final state f, the instantaneous decay amplitude is defined as: $A_f = \langle f|\mathcal{H}|D^0\rangle$ ($\bar{A}_f = \langle f|\mathcal{H}|\bar{D}^0\rangle$). The time-dependent decay rates are obtained as equation 3.15 and equation 3.16, taken from [20]:

$$\begin{aligned}\frac{d\Gamma[D^0_{phys}(t)\to f]/dt}{e^{-\Gamma t}\mathcal{N}_f} &= (|A_f|^2 + |\frac{q}{p}\bar{A}_f|^2)\cosh(y\Gamma t) + (|A_f|^2 - |\frac{q}{p}\bar{A}_f|^2)\cos(x\Gamma t)\\ &+ 2\mathfrak{Re}(\frac{q}{p}A_f^*\bar{A}_f)\sinh(y\Gamma t) - 2\mathfrak{Im}(\frac{q}{p}A_f^*\bar{A}_f)\sin(x\Gamma t)\end{aligned} \tag{3.15}$$

$$\begin{aligned}\frac{d\Gamma[\bar{D}^0_{phys}(t)\to f]/dt}{e^{-\Gamma t}\mathcal{N}_f} &= (|\frac{p}{q}A_f|^2 + |\bar{A}_f|^2)\cosh(y\Gamma t) + (|\frac{p}{q}A_f|^2 - |\bar{A}_f|^2)\cos(x\Gamma t)\\ &+ 2\mathfrak{Re}(\frac{p}{q}A_f\bar{A}_f^*)\sinh(y\Gamma t) - 2\mathfrak{Im}(\frac{p}{q}A_f\bar{A}_f^*)\sin(x\Gamma t)\end{aligned} \tag{3.16}$$

where $\mathcal{N}_f$ is a time-dependent normalization factor. If the final state is its Hermitian conjugate: $A_{\bar{f}} = \langle\bar{f}|\mathcal{H}|D^0\rangle$, $\bar{A}_{\bar{f}} = \langle\bar{f}|\mathcal{H}|\bar{D}^0\rangle$, replace $\mathcal{N}_f$ by $\mathcal{N}_{\bar{f}}$ and A_f by $A_{\bar{f}}$ respectively $\bar{A}_f$ by $\bar{A}_{\bar{f}}$.

There are three types of CP violation, which can occur in a neutral meson system:

- CP violation in the decay process (equation 3.17):

$$\left|\frac{A_f}{\bar{A}_f}\right| \neq 1\,. \tag{3.17}$$

  The decay amplitude A_f of $D^0 \to f$ differs from the decay amplitude $\bar{A}_f$ of $\bar{D}^0 \to f$. So the possibility to decay into the same final state f is different for a D^0 than for a $\bar{D}^0$.

- CP violation in the mixing process (equation 3.18):

$$\left|\frac{q}{p}\right| \neq 1\,. \tag{3.18}$$

  The oscillation probability of $D^0 \to \bar{D}^0$ differs from the probability of $\bar{D}^0 \to D^0$.

- CP violation in the interference between a decay without mixing $D^0 \to f$ and a decay with mixing $D^0 \to \bar{D}^0 \to f$ (equation 3.19):

$$\mathfrak{Im}(\lambda_f) \neq 0\,, \tag{3.19}$$

  where $\lambda_f = \frac{q}{p}\frac{\bar{A}_f}{A_f}$ is the quantity to derive the weak mixing phase $\phi = -arg(\lambda_f)$. The CP violation arises as an interference effect.

3.2. D^0 Mixing in $D^{*+} \to D^0(K^+\pi^-)\pi^+$

To study D mixing in this analysis the dominant decay $D^{*+} \to D^0(K^+\pi^-)\pi^+$ was used. The branching ratio for the decay $D^* \to D^0\pi$ has been measured [19] and is given in equation 3.20:

$$\mathcal{B}(D^* \to D^0\pi) = (67.7 \pm 0.5)\%\,. \tag{3.20}$$

The D^* decay is self tagging, so the production flavor of the D^0 is reconstructable. The final state (K^+, π^-) determines the D^0 decay flavor. Hence, a mixing maesurement can be performed.

There are two physical D^0 decay modes with a kaon and a pion as final state hadrons. The dominant decay is Cabibbo Favored (CF), depicted in equation 3.21:

$$D^0 \to K^-\pi^+ \quad \text{or} \quad \bar{D}^0 \to K^+\pi^-\,. \tag{3.21}$$

Additonally, the D^0 can decay Doubly Cabibbo Suppressed (DCS), depicted in equation 3.22:

$$D^0 \to K^+\pi^- \quad \text{or} \quad \bar{D}^0 \to K^-\pi^+\,. \tag{3.22}$$

Both D^0 decay modes, the dominant CF mode and the suppressed DCS mode, are shown in figure 3.3.

The CF decay chain $D^{*+} \to D^0\pi^+ \to (K^-\pi^+)\pi^+$ is also called 'Right Sign' (RS). The two final state pions have the same charge. Therefore, the DCS decay chain $D^{*+} \to D^0\pi^+ \to (K^+\pi^-)\pi^+$ is

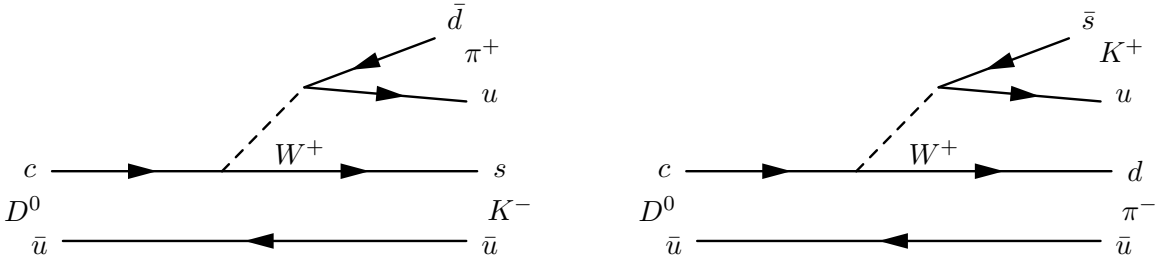

(a) Cabibbo Favored (CF) D^0 Decay

(b) Doubly Cabibbo Suppressed (DCS) D^0 Decay

Figure 3.3.: (a) Cabibbo Favored (CF) Decay: $D^0 \to K^-\pi^+$. The c quark becomes a s quark, so the quark transition occurs within one quark family. (b) Doubly Cabibbo Suppressed (DCS) Decay: $D^0 \to K^+\pi^-$. The c quark becomes a d quark, so the transition occurs between two quark families.

also called 'Wrong Sign' (WS). The two final state pions are oppositely charged. Both branching ratios have been measured [19], given in equation 3.23 and equation 3.24.

$$\mathcal{B}(\text{RS}) = (3.89 \pm 0.05)\% \tag{3.23}$$

$$\mathcal{B}(\text{WS}) = (1.48 \pm 0.07) \times 10^{-4} \tag{3.24}$$

The ratio of these branching ratios can be directly measured, given in equation 3.25.

$$\frac{\mathcal{B}(\text{WS})}{\mathcal{B}(\text{RS})} = (3.80 \pm 0.19) \times 10^{-3} \tag{3.25}$$

The D mixing occurs, when a D^0 mixes into a $\bar{D}^0$ and the $\bar{D}^0$ decays into the final state hadrons, or vice versa, see equation 3.26. In both cases the mixed D will most likely decay in the CF mode considering the above quoted branching ratios for CF and DCS D decays.

$$D^0 \to \bar{D}^0 \to K^+\pi^- \quad \text{or} \quad \bar{D}^0 \to D^0 \to K^-\pi^+ \,. \tag{3.26}$$

The dominant mixing process is visualized by "box" diagrams, see figure 3.4.

Taking only the D production flavor and the final state hadrons flavors into account, the mixed decay carries also WS signature. Hence, the branching ratio for D^0 WS decays splits up into two parts, first the DCS decay without mixing, see equation 3.27 and second the mixed decay, where the final D^0 meson decays CF, see equation 3.28, measured by [19].

$$\mathcal{B}(\text{DCS}) = (1.31 \pm 0.08) \times 10^{-4} \tag{3.27}$$

$$\mathcal{B}(\text{mixing}) < 1.6 \times 10^{-5} \,@\, \text{CL} = 95\% \tag{3.28}$$

The D^0 mixing has contributions from short range physics processes (box diagrams), shown in figure 3.4, responsible for the mass difference ΔM, and from long range processes with intermediate hadron states, shown in figure 3.5, responsible for the width difference $\Delta\Gamma$ between the mass eigenstates.

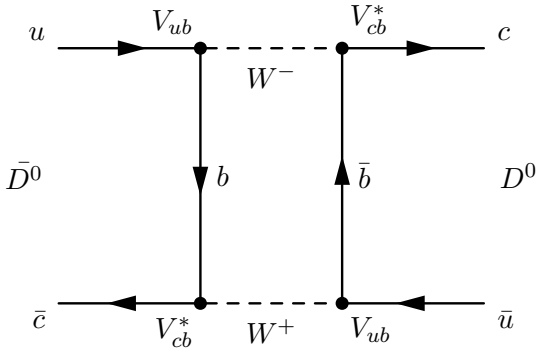

(a) First Possibility of Meson Mixing within the Standard Model

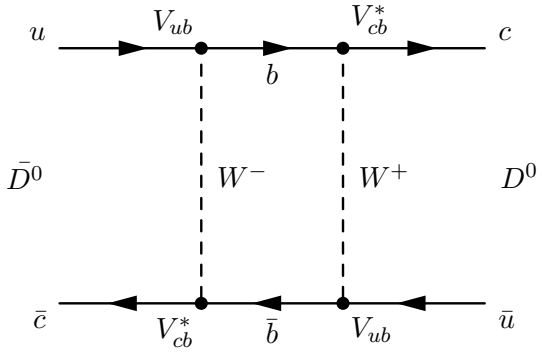

(b) Second Possibility of Meson Mixing within the Standard Model

Figure 3.4.: Box diagrams for $D^0 - \bar{D}^0$ mixing. There are two possibilities of mixing processes (in first order) within the Standard Model described by the CKM mechanism. The intermediate state quarks must be down type quarks, but due to the fact, that the b quarks are much heavier than the d and s quarks, in almost all cases only b and $\bar{b}$ quarks take part in the mixing process. Hence, these are the dominant diagrams for $D^0 - \bar{D}^0$ mixing.

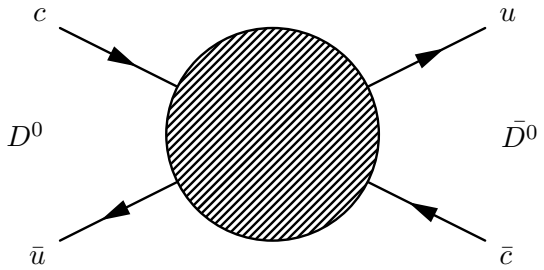

Figure 3.5.: Long range diagram for $D^0 - \bar{D}^0$ mixing. The central blob denotes intermediate hadron-hadron states like K^+K^-, $\pi^+\pi^-$, $K^+\pi^-$, $\pi^+\pi^-\pi^0$, etc.

Under certain theoretical assumptions the expansion in xt and yt of the time-dependent decay rates, previously shown in equation 3.15 and equation 3.16, yields equation 3.29 and equation 3.30, taken from [20]:

$$\frac{\Gamma[D^0_{phys}(t) \to K^+\pi^-]}{\Gamma[\bar{D}^0_{phys}(t) \to K^+\pi^-]} = \underbrace{r_d^2}_{\text{DCS/CF}} + \underbrace{r_d \left|\frac{q}{p}\right| (y' \cos\phi_D - x' \sin\phi_D)\Gamma t}_{\text{Interference}} + \underbrace{\left|\frac{q}{p}\right|^2 \frac{y^2 + x^2}{4}(\Gamma t)^2}_{\text{Mixing}} \tag{3.29}$$

$$\frac{\Gamma[\bar{D}^0_{phys}(t) \to K^-\pi^+]}{\Gamma[D^0_{phys}(t) \to K^-\pi^+]} = \underbrace{r_d^2}_{\text{DCS/CF}} + \underbrace{r_d \left|\frac{p}{q}\right| (y' \cos\phi_D + x' \sin\phi_D)\Gamma t}_{\text{Interference}} + \underbrace{\left|\frac{p}{q}\right|^2 \frac{y^2 + x^2}{4}(\Gamma t)^2}_{\text{Mixing}} \tag{3.30}$$

The mixing parameters x and y are defined up to a strong phase difference δ between the CF and the DCS decay amplitudes, hence they are substituted by x' and y', see equation 3.31:

$$y' = y\cos(\delta) - x\sin(\delta)\,, \quad x' = x\cos(\delta) + y\sin(\delta)\,. \tag{3.31}$$

The symbol r_d denotes the ratio of the DCS decay amplitude to the CF decay amplitude, see equation 3.32:

$$r_d = \left|A_{K^+\pi^-}/\bar{A}_{K^+\pi^-}\right| = \left|\bar{A}_{K^-\pi^+}/A_{K^-\pi^+}\right|\,. \tag{3.32}$$

The mixing parameters can be extracted from the time dependence of the WS and RS decay rates. Analyzing the occurred WS and RS events as a function of the time t gives a measure on all D mixing parameters, x', y', q/p and the weak phase ϕ_D. Equation 3.29 and equation 3.30 are therefore divided into three summands, listed in the following enumeration.

1. DCS/CF: This term is just the ratio of the DCS and CF branching ratios $\mathcal{B}$(DCS), $\mathcal{B}$(CF), a constant offset in the distribution.
2. Mixing: This term originates from the mixed decays.
3. Interference: This term arises through the interference of the DCS and mixed decays.

The weak mixing phase $\phi_D = -arg(\lambda_f)$ can then be derived following equation 3.33:

$$\lambda_{K^-\pi^+} = r_d(q/p)e^{-i(\delta-\phi_D)}\,, \quad \lambda^{-1}_{K^+\pi^-} = r_d(p/q)e^{-i(\delta+\phi_D)}\,. \tag{3.33}$$

Under the assumptions, that CP symmetry is conserved and the values for x and y are small, the ratio R of $D^0 \to K^+\pi^-$ to $D^0 \to K^-\pi^+$ decay rates can be approximated as a quadratic function of t/τ, where t is the proper time and τ is the mean D^0 lifetime, taken from [6] and shown in equation 3.34.

$$R(t/\tau) = R_D + \sqrt{R_D}y'(t/\tau) + \frac{x'^2 + y'^2}{4}(t/\tau)^2 \tag{3.34}$$

$R_D = r_D^2$ denotes the squared modulus of the ratio of DCS to CF amplitudes.

Evidence for $D^0 - \bar{D}^0$ mixing was found by BaBar [1], Belle [3] and CDF [6]. However, a $5\,\sigma$ measurement of a single experiment was not yet performed. The BaBar experiment, positioned at the e^+e^- collider SLAC, performed a D mixing analysis on $384\,\mathrm{fb}^{-1}$ of data. R_D was measured to be $[0.303 \pm 0.016(\mathrm{stat.}) \pm 0.010(\mathrm{syst.})]\%$. The analysis provides evidence for $D^0 - \bar{D}^0$ mixing at a level of 3.9 standard deviations (σ). For CP violation no evidence was found. The Belle experiment, positioned at the e^+e^- collider KEKB, observed evidence for D mixing by measuring the difference in the apparent lifetime when a D^0 meson decays to the CP eigenstates K^+K^- and $\pi^+\pi^-$ and when it decays to the final state $K^+\pi^-$. The result is obtained at a level of $3.2\,\sigma$ and is based on $540\,\mathrm{fb}^{-1}$ of data. The CDF experiment, positioned at the hadron collider TeVatron, performed an analysis on $1.5\,\mathrm{fb}^{-1}$ of data and recorded 12.7×10^3 WS events. The time dependence of the ratio of decay rates for the WS $D^0 \to K^+\pi^-$ decay to the CF decay $D^0 \to \mathrm{K}^-\pi^+$ was measured. The hypothesis, that D mixing does not occur, was excluded at a level of $3.8\,\sigma$.

Hence, the average values for D mixing are quoted from the Heavy Flavor Averaging Group (HFAG). The parameters are derived by dedicated fits in two different ways distinguished by their

basic assumption. The first assumption is that the CP symmetry is not directly violated, while the second assumption is that CP symmetry violation is allowed. All D^0 mixing parameter world average values are listed in table 3.1. Additionally, two dimensional plots of x against y assuming no direct CP violation, figure 3.6, and assuming direct CP violation, figure 3.7, are given. Finally, also the decay amplitude ratio q/p is given as a two dimensional plot, the absolute value of q/p against the angle's argument of q/p, see figure 3.8.

parameter	No CPV	CPV-allowed	CPV-allowed 95% C.L.
$x(\%)$	$0.65 \quad +0.18 - 0.19$	$0.63 \quad +0.19 - 0.20$	$[\ 0.24, 1.00\ ]$
$y(\%)$	$0.74 \quad \pm 0.12$	$0.75 \quad \pm 0.12$	$[\ 0.51, 0.99\ ]$
$\delta(^\circ)$	$21.3 \quad +9.8 - 11.1$	$22.0 \quad +9.8 - 11.2$	$[\ -3.1, 40.7\ ]$
$R_D(\%)$	0.3308 ± 0.0080	0.3309 ± 0.0081	$[\ 0.315, 0.347\ ]$
$A_D(\%)$	–	$-1.92 \quad \pm 2.4$	$[\ -6.6, 2.8\ ]$
$\lvert\frac{q}{p}\rvert$	–	$0.91 \quad +0.18 - 0.16$	$[\ 0.60, 1.28\ ]$
$\phi(^\circ)$	–	$-10.2 \quad +9.4 - 8.9$	$[\ -27.5, 8.4\ ]$

Table 3.1.: World Average D^0 Mixing Parameter Results. [14]

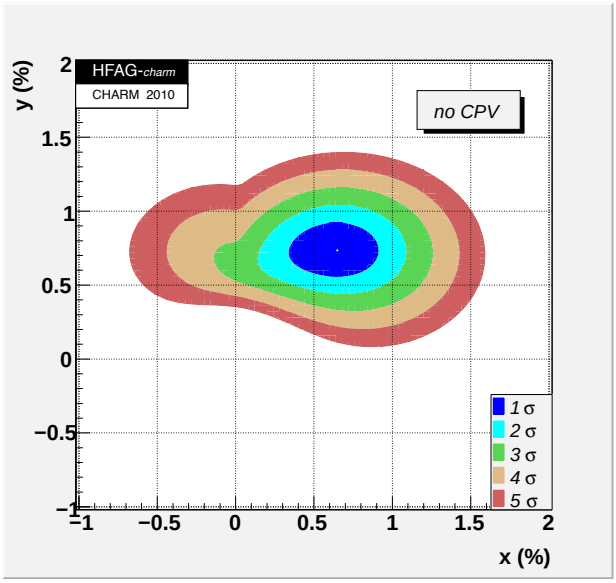

Figure 3.6.: Heavy Flavor Averaging Group (HFAG): World average results for the D^0 mixing parameters x and y. No direct CP violation is assumed in the calculation. [14]

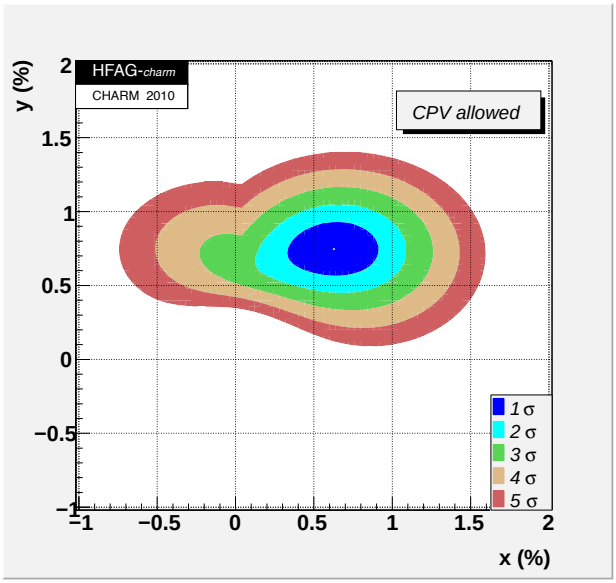

Figure 3.7.: HFAG: World average results for the D^0 mixing parameters x and y. CP violation is allowed in the basic assumption of the calculation. [14]

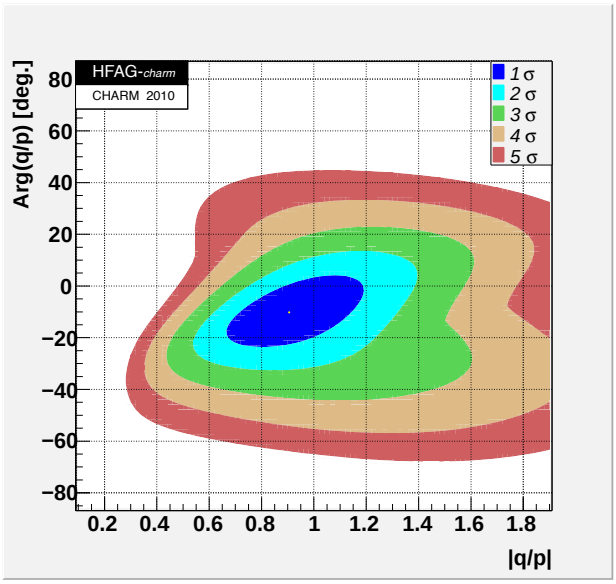

Figure 3.8.: HFAG: World average mixing results for the D^0 mixing parameters $\frac{q}{p}$. CP violation is allowed in the basic assumption of the calculation. [14]

4. $D^{*+} \to D^0(K^+\pi^-)\pi^+$ Wrong Sign Selection

A first step towards the mixing analysis in the D system is to reconstruct RS and especially WS decays properly. The D mixing is very slow, therefore the measurement of mixed decays is complicated by a huge background. Hence, the optimization of the selection is a crucial part of the analysis. In this thesis a WS selection is developed and optimized to reach a maximum signal significance.

The selection was optimized on an exclusive signal MC sample[1] with respect to a minimum bias data sample. The MC signal sample exclusively simulates the decay $D^{*+} \to D^0\pi^+ \to (K\pi)\pi^+$ and its charge conjugate. It includes prompt D^*s as well as D^* coming from B decays. The generation conditions of this sample were adjusted to the real data taking conditions since March 2010, when the LHC ran at an center-of-mass energy of 7 TeV. Hence, the center-of-mass energy was simulated with $2 \times 3.5\,\text{TeV}$ and corresponds to an integrated luminosity of $\mathcal{L} = 193.49\,\text{nb}^{-1}$.

The integrated luminosity of the signal MC sample was calculated, using equation 4.1:

$$\mathcal{L} = \frac{\#\text{events}}{\epsilon_{gen}} \left(\{\sigma_{bb} f_{b\to B} f_{B\text{accepted}} \mathcal{B}_{B\to D^*} + \sigma_{cc} f_{c\to D^*} f_{D^*\text{accepted}}\} \cdot \mathcal{B}_{D^*\to D^0\pi_s\to\{K\pi\}\pi_s} \right)^{-1} . \quad (4.1)$$

Simulated are 2.4×10^6 events. These events are reduced by the fraction of D^* momenta pointing into the detector acceptance with respect to all D^* momenta, denoted by ϵ_{gen}. Additionally a factor, computed by the cross-sections of $b\bar{b}$ and $c\bar{c}$ events, the fractions to form out of a b quark a B meson and out of a c quark a D^* meson, the fractions to accept these B and D^* mesons, and finally the branching ratios of the $B \to D^*$ decays and the signal decay $D^* \to D^0\pi_s \to (K\pi)\pi_s$, has to be considered also. The used MC generator values are listed in table 4.1[2].

The minimum bias data sample was recorded in April 2010[3] and was minimal triggered to exclude beam gas events. It contains events with at least one proton proton interaction and corresponds to an integrated luminosity of approximately $\mathcal{L} = 400\,\mu\text{b}^{-1}$. Compared to the luminosity of the signal MC sample of $193.49\,\text{nb}^{-1}$ the luminosity of the minimum bias data sample is a factor of ~ 500 smaller. Only such a small amount of minimum bias data was taken in the beginning of the data taking period filtered by the one track trigger, because later the high level trigger was switched on to record signal data sets for physics analysis.

In this thesis a selection for the WS decay $D^{*+} \to D^0(K^+\pi^-)\pi^+$ is developed. This is a challenging task, because the WS decays are strongly suppressed, $1\#WS \sim 260\#RS$, and the

[1] MC, 2010, Beam3500GeV-VeloClosed-MagDown-Nu1, 2010-Sim03Reco03-withTruth, $Dst\_D0pi,hh = DecProdCut$. LHC*b* event type number: 27363001, Gauss v38r4.

[2] The LHC*b* generator statistics are documented in `http://lhcb-release-area.web.cern.ch/LHCb-release-area/DOC/gauss/`, the Branching Ratios $\mathcal{B}$ are taken from [19].

[3] LHC*b* run numbers: 69353 – 71807.

Quantity	Generator Value		
ϵ_{gen}	0.3765	$\pm$	0.00067
σ_{bb}	0.4965	$\pm$	0.00128 mb
σ_{cc}	5.3928	$\pm$	0.00411 mb
$f_{B\text{accepted}}$	0.9085	$\pm$	0.00748
$f_{D^*\text{accepted}}$	0.7373	$\pm$	0.00087
$f_{b\to B}$	0.7980	$\pm$	0.015
$f_{c\to D^*}$	0.255	$\pm$	0.017
$\mathcal{B}_{B\to D^*}$	0.255	$\pm$	0.015
$\mathcal{B}_{D^*\to D^0\pi_s\to(K\pi)\pi_s}$	0.030	$\pm$	0.004

Table 4.1.: Generation values for the signal MC sample.

D mixing is very slow. Hence, a huge background needs to be suppressed. Additionally, due to the hadronic character of the proton proton interactions, a lot of combinatorial background appears. Consequently, the detector is full of kaons and pions. Out of these tracks the D^0 are reconstructed and finally together with another pion track the D^* are combined. So there are two stages, at which combinatorics can strike. This will be discussed in detail in section 4.1. Although the minimum bias data set is a factor of ~ 500 smaller than the signal sample, the background contribution considered in the selection optimization is sufficient, because the D^0 mass window is chosen to be very broad (150 MeV) compared to the signal peak (25 MeV) and also the combinatorial and the random soft pion background combinations of the D^* decay are not rejected during the optimization process. The broad D^0 mass range gives a background increasing factor of 6 and the wide D^* decay combinations give a factor of 4.5. Hence, in total the background used to optimize the selection is increased by a factor of 27.

4.1. Physics Background

To perform a mixing analysis the D^0 production flavor and the decay flavor have to be measured. Thus the self tagging WS decay chain $D^{*+} \to D^0\pi^+$, $D^0 \to K^+\pi^-$ is used. As mentioned above, there are two reconstruction stages, where the D^0 flavor determination can be incorrect, the combination of a kaon and a pion to a D^0 and the combination of this D^0 and another pion to a D^*. The probability for random soft pion background increases with the event activity, because when the event is very full of interactions many pions are produced, that can be wrongly matched to a D^0 to form a D^*. Although this background is peaking in the D^0 mass, it is caused by combinatorics. Additionally, general combinatorial background can fake the occurrence of the entire decay. Consequently, there are two sources of combinatorial background, the common combinatorics and the random soft pion combinations, and one source of physics background, the double misidentification of the D^0 daughters.

4.1.1. Combinatorial Background

The combinatorial background consists of kaons and pions, which are produced at the primary vertex or at other decays, forming fake D^0 and D^* decays. This kind of background is flat in the mass distributions of the D^0 and the D^*. The main part of this background is rejected through displacement cuts, requiring a minimum distance of the D^0 decay vertex with respect to the primary vertex. If still a part of this background remains after the final signal selection, it can be eliminated through D^0 mass sideband subtraction. Sideband subtraction is a statistical instrument to apply weights, with values between -1 and $+1$, to candidates that are filled in a histogram. Here, the values for the weights are determined in the D^0 mass distribution. In this distribution regions of pure signal, of background under signal and of pure background are defined by the fitted Probability Density Function (PDF), that is composed of a signal and a background PDF. The weights are then determined by the number of events lying in each region. A detailed explanation is given in section 5.2. Depending on the corresponding D^0 mass value, a weight is applied to the candidate filled in the histogram. In this way also background lying under the signal peak is eliminated.

4.1.2. Random Soft Pion Background

The random soft pion background consists of coincidentally tagged D^0 production flavors. Soft pion (π_s) tracks are randomly combined to D^0 candidates to reconstruct the D^* decay. In 50% of all cases, these random combinations will faulty tag the D^0 production flavor. This background will also make out of a RS decay a WS decay and vice versa, but in contrast to the double misidentification background it is peaking in the D^0 mass. So a separating variable is necessary, like the $\Delta M = m_{D^*} - m_{D^0}$ distribution. The masses of the D^* and the D^0 mesons are quite close, $m_{D^*} = (2010.27 \pm 0.17)\,\mathrm{MeV}$ and $m_{D^0} = (1864.84 \pm 0.17)\,\mathrm{MeV}$. So calculating the mass difference, see equation 4.2:

$$\Delta M = m_{D^*} - m_{D^0} = 145.43\,\mathrm{MeV} = m_\pi + 5.86\,\mathrm{MeV} \tag{4.2}$$

yields a small mass range around the pion mass. Almost all decay energy of the D^* decay goes into the D^0 mass, hence, the pion is low energetic, so it is called soft pion: π_s. Hence, the ΔM quantity is a good proof for the correctly tagged D^0 reconstruction. Cutting in ΔM or using the distribution for side band subtraction is therefore a very effective method against combinatorical background.

The correctly combined D^*s peak very clear around the pion mass, while the random pion combinations yield a flat background distribution. To select WS Signal candidates without random π_s background, the D^0 mass distribution is ΔM sideband subtracted.

4.1.3. Double Misidentification Background

The double misidentification background consists of RS decays where the D^0 decay tracks are misidentified because the kaon and pion mass hypothesis assignments are mistakenly interchanged. The kaon and pion masses are not measured by the LHC*b* detector but the mass hypothesis is determined by the particle identification system, see section 2.2.2. If the kaon was misidentified

as a pion and the pion as a kaon, a much more likely RS decay is reconstructed as a WS. This case is illustrated in the following scenario. Assuming the physics process is a RS decay, depicted in equation 4.3.

$$D^0 \to K^- \pi^+ \tag{4.3}$$

Given the double misidentification case, the mass hypothesis assignments are mistakenly interchanged. Then the physical RS decay is reconstructed as a WS decay, depicted in equation 4.4.

$$D^0 \to \pi^- K^+ \tag{4.4}$$

In the MC simulation, the true physics decay is accessible through the MC associator. Hence, the frequency of double misidentified D^0 decay tracks can be studied. In data the D^0 mass is reconstructed with 1862 MeV. Within two standard deviations ($m_{D^0} \pm 20\,\text{MeV}$) 98% of the MC truth signal WS decays are located in this mass range. Due to the fact, that the mass distribution of double misidentified D^0 decay tracks is much broader, only 25% of these background decays are located in the same mass range. Nevertheless, because of the 260 times larger branching ratio of RS decays, this is a serious physics background. A special cut, named D^0 mass swap cut, was introduced to reject these background events. The D^0 decay tracks mass hypotheses are swapped again and the D^0 masses are recalculated using the 4 vector formalism for relativistic particles. After swapping the mass hypothesis of the double misidentification background again, the D^0 background mass distribution is peaking like the signal mass distribution. These background events are rejected by cutting on that peaking mass within the mass range of $m_{D^0} \pm 20\,\text{MeV}$. Swapping the mass hypotheses of signal events, leads to the broad mass distribution like the double misidentification background mass distribution, of course. Applying this mass swap cut to all events leads to a double misidentification background suppression of 97%, while it keeps 85% of the signal events.

4.1.4. WS D^0 Decay Signal Box

WS decay signal candidates can only be selected by using the information of at least both distributions, the D^0 mass and the $\Delta M = m_{D^*} - m_{D^0}$ distribution. The double misidentification background peaks in the ΔM distribution, while it is flat in the D^0 mass distribution. The random π_s background peaks in the D^0 mass distribution, while it is flat in the ΔM distribution. Hence, the true WS signal candidates can only be estimated as a signal box in the two dimensional histogram of the ΔM against the D^0 mass distributions, see figure 4.1. After the preselection, figure 4.1 (a), the underlying physical background is still present, flat in both variables ΔM and D^0 mass. After the final selection, figure 4.1 (b), the physical background vanishes and the true signal shrinks to a signal box with defined tight limits in the ΔM and in the D^0 mass distribution.

Other combinatorial background, random combinations of kaons and pions from other decay processes, visible as a flat background in the D^0 mass distribution, if still present after the final selection, can then be eliminated by sideband subtraction in the mass distribution.

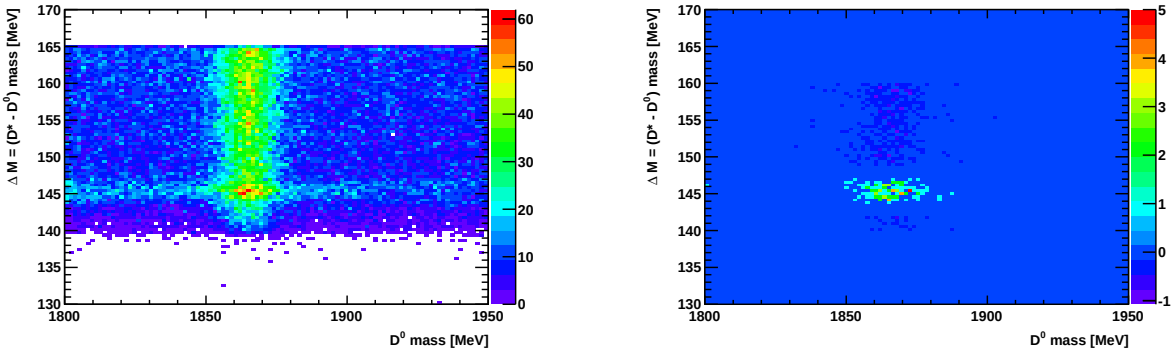

(a) 2D D^0 mass – ΔM preselected

(b) 2D D^0 mass – ΔM finally selected and ΔM sideband subtracted

Figure 4.1.: MC reconstructed signal WS decays: 2 dimensional plot of the D^0 mass distribution against the $\Delta M = m_{D^*} - m_{D^0}$ distribution before (a) and after (b) the signal selection including the D^0 mass swap cut and the ΔM sideband subtraction. The WS signal decays are shrinked to a signal box with defined tight limits in both quantities, the D^0 mass and the ΔM quantity.

4.2. WS Decay Selection Cuts

MC truth information is used to separate the reconstructed D^0 candidates in two categories: true signal D^0 candidates and fake D^0 candidates. By comparing the reconstructed distributions of quantities such as the track χ^2, the impact parameter or the transverse momentum distribution of the minimum bias data events with the MC truth events selection criteria are found to reject fake D^0 candidates. In this section all considered cut quantities are introduced and for each quantity the corresponding distributions for signal and background are shown. The next section, section 4.3, will demonstrate the optimization process of the interplay of these cut quantities to find the best value for every cut. In section 4.4 a total and a relative efficiency is given for every cut leading to the choice of the final selection's cuts, shown in section 4.5.

The basis to start a comparison of minimum bias data quantities to MC signal quantities is a very loose preselection consisting of momenta, track and vertex quality cuts, listed in table 4.2. The cuts will be explained in detail in the following paragraphs. At this point a uniform preselection for both samples, the signal MC sample and the minimum bias data sample, is necessary, to assure that these samples are comparable.

Choosing the best set of cuts is not a trivial task. Here, the approach was taken to keep the cut quantities descriptive and to avoid too many correlations. First of all the geometry of the decay determined by the particles momenta was used to distinguish between signal and background. Second, a choice is made through selecting only candidates, that provide a minimum quality in reconstruction. Third, due to the fact, that a correct separation of kaons and pions is crucial for this mixing analysis, cuts on particle identification quantities are made. Finally, the displaced character of a D^0 decay is used by requiring a minimum impact parameter of the D^0 daughters.

Particle	Cut Variable		Cut Value
D^0 daughters	p	$>$	1000 MeV
D^0 daughters	p_T	$>$	100 MeV
D^0 daughters	Track $\chi^2/ndof$	$<$	10
D^0	Vertex $\chi^2/ndof$	$<$	12
π_s	p_T	$>$	110 MeV
π_s	Track $\chi^2/ndof$	$<$	12
D^*	Vertex $\chi^2/ndof$	$<$	14

Table 4.2.: Preselection: Basis for the Comparison of Minimum Bias Data with Signal MC

The other way around to use the prompt character of the D^* and the slow pion, a maximum impact parameter of these particles is required. The cuts are discussed in detail in the following paragraphs.

To assure that the minimum bias data sample totally consists of fake D^0 background events, only the events of the D^0 mass sidebands are taken to find the optimal selection. Figure 4.2 shows the chosen categories for true signal D^0 candidates in MC and for fake background D^0 candidates in minimum bias data. The mass sidebands for the background category are chosen asymmetric around the MC $m_{D^0} = 1865\,\text{MeV}$ mass peak, because in data the mass peak is shifted by 3 MeV to smaller masses, $m_{D^0} = 1862\,\text{MeV}$. This mass shift to smaller values is caused by the not yet perfect alignment and magnetic field calibration of the LHC*b* detector. The same limits are chosen for this category as for the swapped D^0 mass cut: $m_{D^0} \pm 2\sigma = [1842, 1881]\,\text{MeV}$.

4.2.1. Momenta Cuts

The masses of the final state hadrons kaon and pion are compared to the D^0 mass much smaller: $m_{D^0}(1865\,\text{MeV}) \gg m_K(493\,\text{MeV}) + m_\pi(139\,\text{MeV})$. Approximately 1 GeV of the D^0 rest energy plus the kinetic energy of the D^0 is left to become kinetic energy of the final state hadrons. This is a good criterion to distinguish between low energetic prompt background and high energetic signal final state hadrons.

Momentum

The main part of the left D^0 decay energy is transformed into a boost in flight direction of the final state hadrons. Hence, the MC signal D^0 daughters have a energetically higher momentum distribution, see figure 4.3, while the momentum distribution of the fake D^0 daughters peaks at small momenta.

Transverse Momentum

The transverse momentum p_T is defined as the fraction of the momentum p, that is perpendicular to the z-axis, the main flight direction of heavy particles. In the transverse momentum distribution

4. $D^{*+} \to D^0(K^+\pi^-)\pi^+$ Wrong Sign Selection

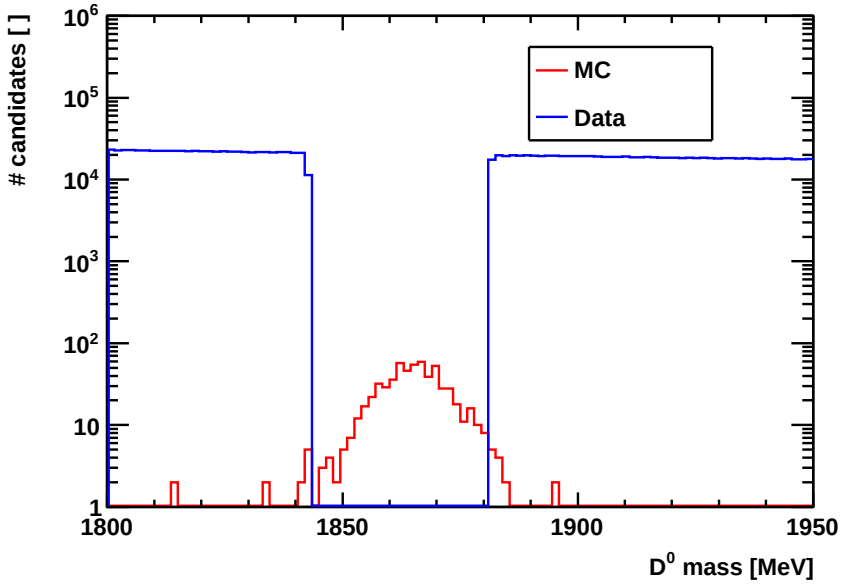

Figure 4.2.: D^0 mass distribution for signal MC candidates (red curve) and fake D^0 background candidates in minimum bias data (blue curve). In avoid any potential signal tail in the background distribution, we restrict ourselves to the D^0 mass sideband region to study fake D^0 distributions.

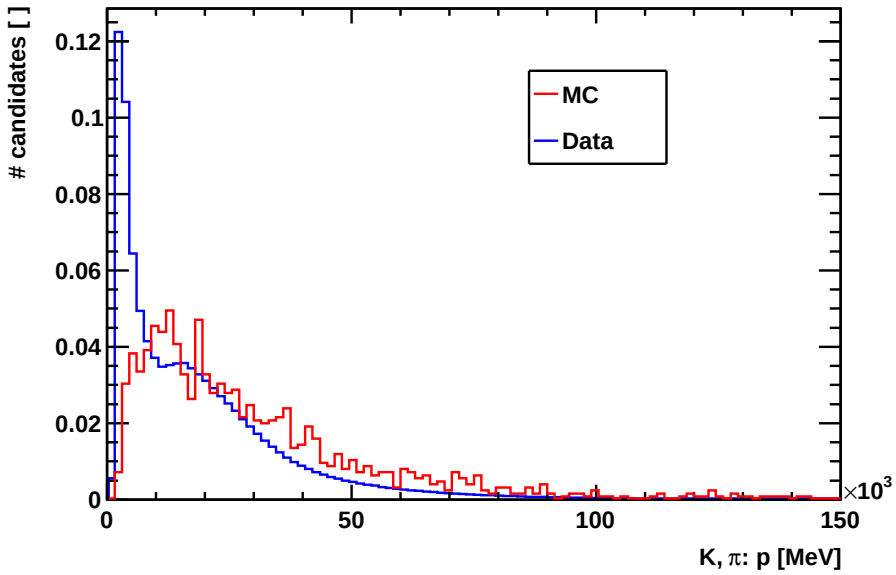

Figure 4.3.: Momentum distribution of the D^0 daughters of MC truth signal D^0 (red curve) and minimum bias data fake D^0 (blue curve). The background distribution peaks at low momenta.

the separation power of this energetic criterion is even more apparent. Fake D^0, D^0 daughters, D^* and fake soft pions are all a lot lower energetic than the signal final state hadrons and Ds, see figure 4.4, figure 4.5, figure 4.6 and figure 4.7.

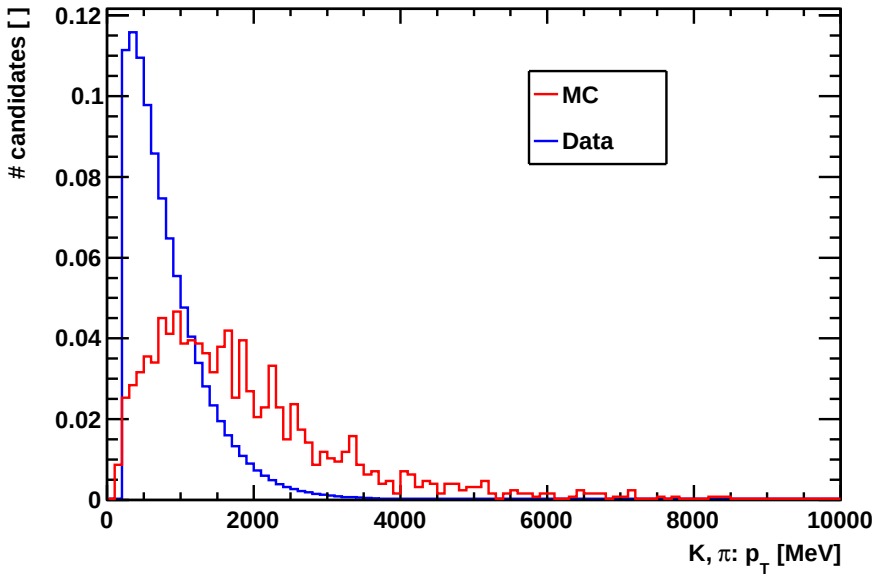

Figure 4.4.: Transverse Momentum distributions of the D^0 daughters of MC truth signal D^0 (red curve) and minimum bias data fake D^0 (blue curve). The background distribution peaks at low transverse momenta.

4.2.2. Quality Cuts

Track χ^2/ndf

The track χ^2 is defined as the squared sum of the perpendicular distances between the track and all hits assigned to it. This quantity is minimized by the track fitting algorithms to obtain an optimal alignment. To trust a reconstructed track, the reduced χ^2, normalized to the number of degrees of freedom of the track, is taken. Ideally the track χ^2/ndf is equal to one. Consequently, the bigger the track χ^2/ndf, the worse the reconstructed track. A maximum cut of 5 is recommended by the tracking group. The track χ^2/ndf distributions for fake D^0 daughters and fake soft pions compared to signal D^0 daughters and signal soft pions are shown in figure 4.8 and figure 4.9.

Vertex χ^2/ndf

The vertex χ^2 is defined as the squared sum of the perpendicular distances between a vertex and all tracks assigned to it. The uncertainties in the distances are included in the calculation. Similar to the track χ^2/ndf the vertex χ^2/ndf is minimized by the algorithms for vertex reconstruction to obtain optimal vertex positions. Again, ideally the vertex χ^2/ndf is equal to one. The vertex

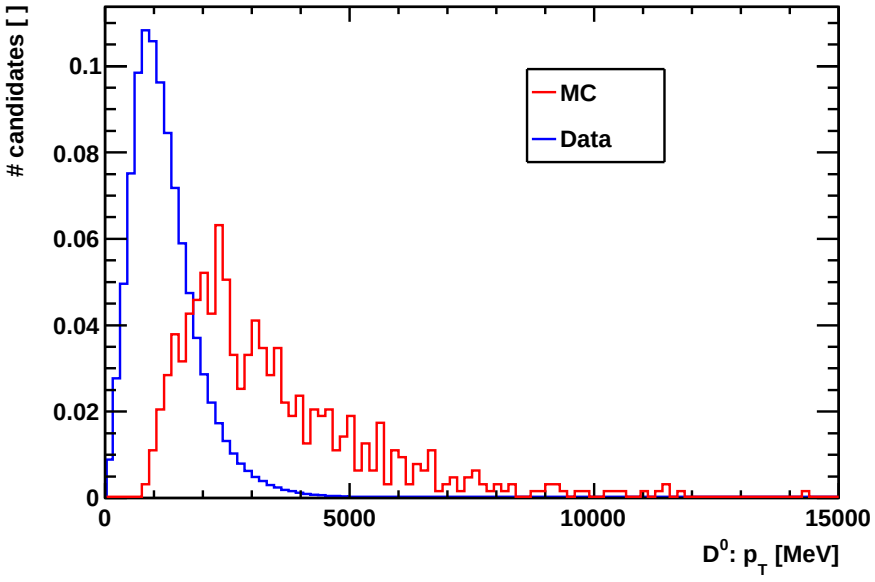

Figure 4.5.: Transverse Momentum distributions of MC truth signal D^0 (red curve) and minimum bias data fake D^0 (blue curve). The fake D^0 background distribution peaks at low transverse momenta.

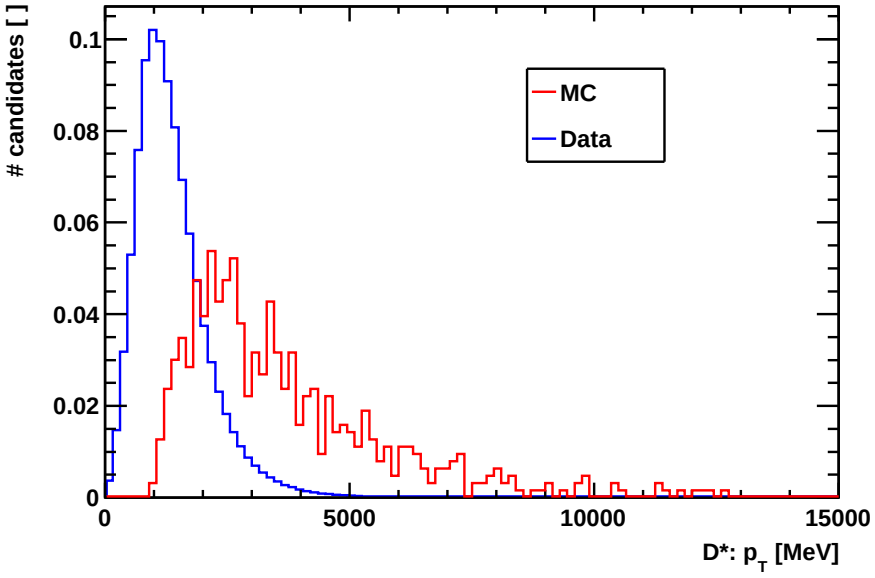

Figure 4.6.: Transverse Momentum distributions of MC truth signal D^* (red curve) and minimum bias data fake D^* (blue curve). The fake D^* background distribution peaks at low transverse momenta.

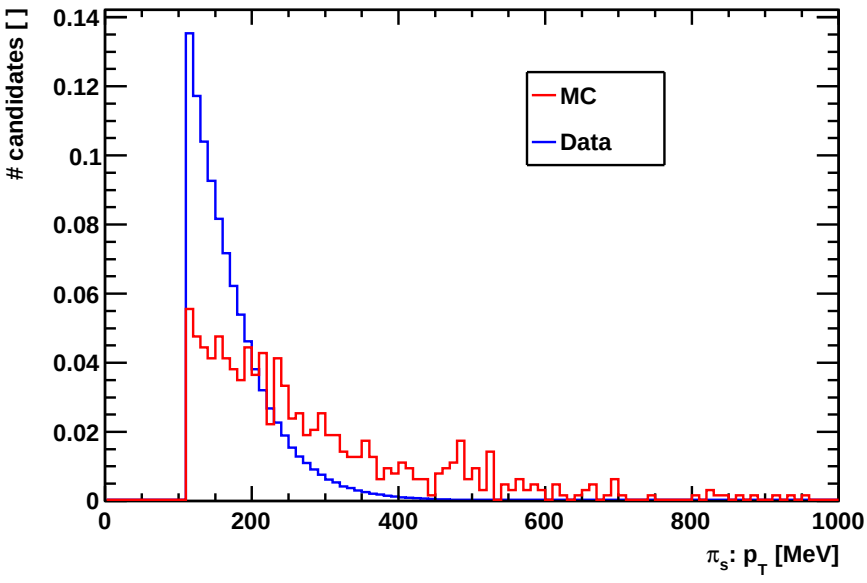

Figure 4.7.: Transverse Momentum distributions of MC truth signal soft pions (red curve) and minimum bias data fake soft pions (blue curve). The fake soft pion background distribution peaks at low transverse momenta.

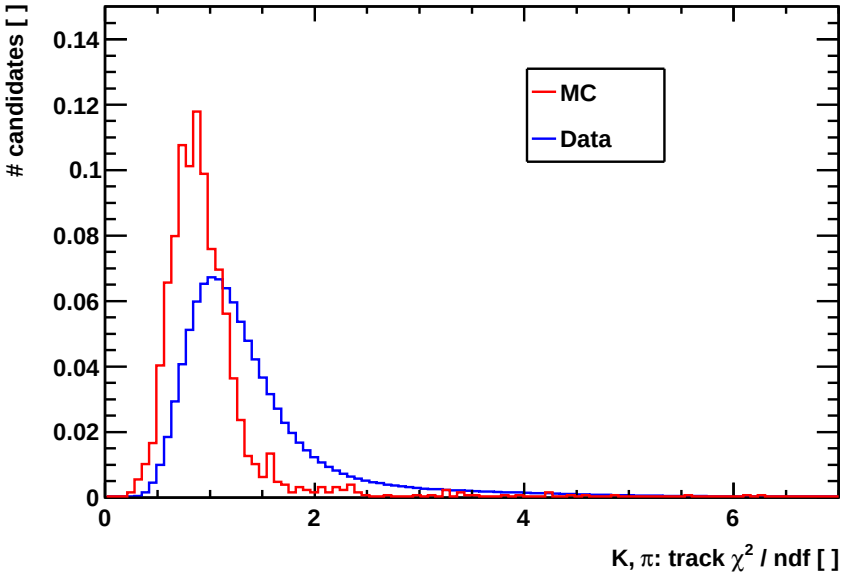

Figure 4.8.: Track χ^2/ndf distributions of MC truth signal D^0 daughters (red curve) and minimum bias data fake D^0 daughters (blue curve). The quality of the fake D^0 daughters background tracks is not as good as the quality of the signal D^0 daughters' tracks.

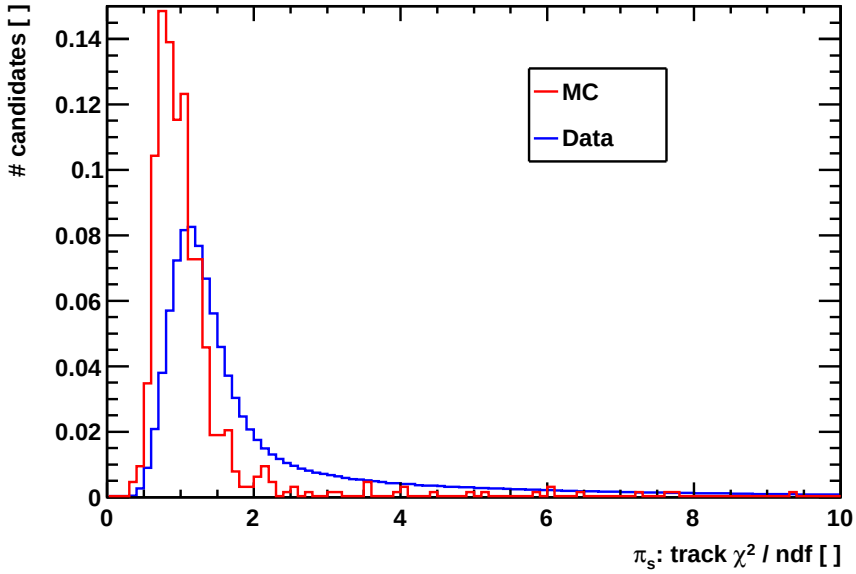

Figure 4.9.: Track χ^2/ndf distributions of MC truth signal soft pions (red curve) and minimum bias data fake soft pions (blue curve). The quality of the fake soft pions background tracks is not as good as the quality of the signal soft pions' tracks.

χ^2/ndf distributions for fake D^0 and D^* compared to the distributions for signal D^0 and D^* are shown in figure 4.10 and figure 4.11. These distributions are not significantly different for signal and fake decays.

Direction Angle

The direction angle, short dira = cos(Θ), is defined as the angle between the momentum and the ideal flight direction of the D^0, see figure 4.12. The ideal flight direction is calculated as the connecting line between the D^0 production vertex and the D^0 decay vertex. Ideally this angle should be zero, meaning dira = 1. Hence, the cut is placed pretty close to 1, in this case 0.99993. The dira distributions for fake D^0 decays compared to signal D^0 decays are shown in figure 4.13. The MC signal D^0 candidates are pointing better back to the primary vertex. Fake D^0 candidates, that do not point back to the primary vertex are most likely produced in displaced B decays.

4.2.3. Particle Identification and Interchanged Mass Assignment Cuts

Delta Log Likelihood

The Delta Log Likelihood, short DLL, is a measure for the relative particle hypothesis probability. Here, the probability to reconstruct a kaon is calculated with respect to the probability a pion is reconstructed. With the help of the information of the particle identification system to each track a certain particle hypotheses is assigned. The particle hypothesis was estimated before in

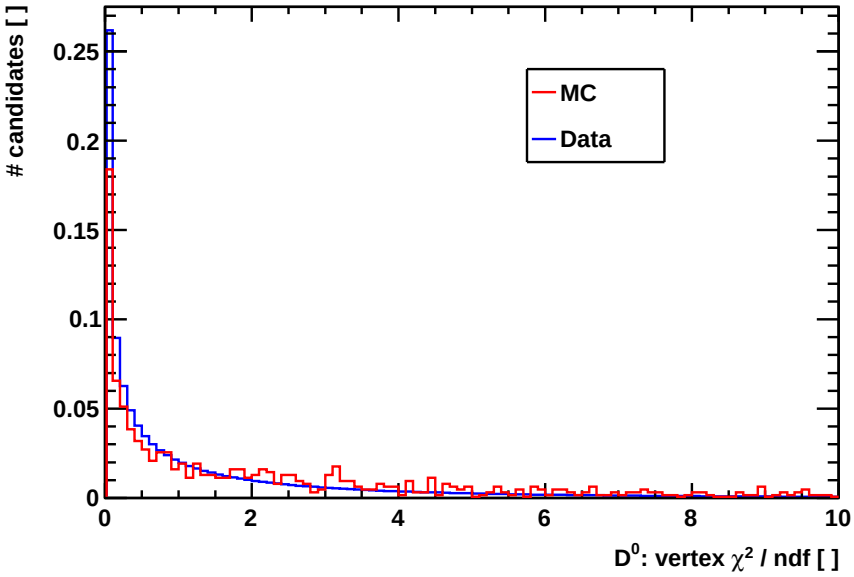

Figure 4.10.: Vertex χ^2/ndf distributions of MC truth signal D^0 (red curve) and minimum bias data fake D^0 (blue curve). The vertex quality for fake D^0 background decays is not significantly worse than for signal D^0 decays.

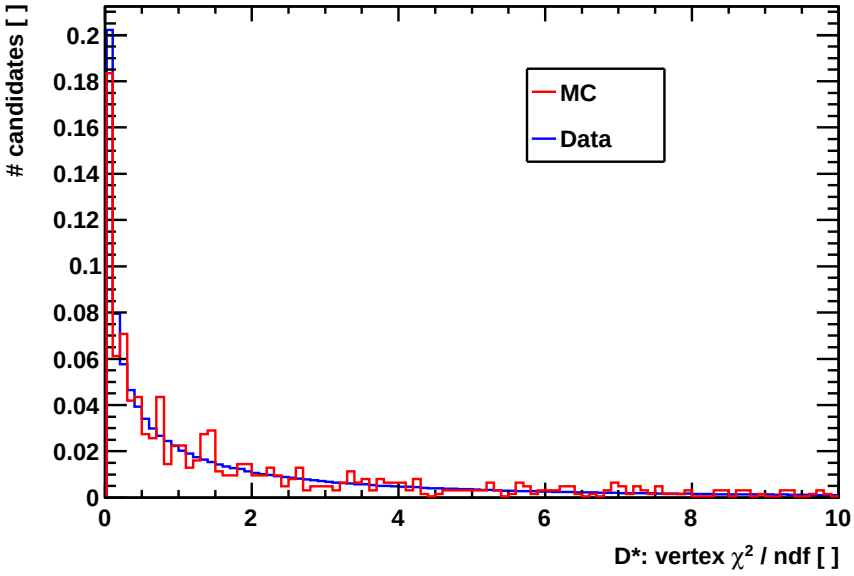

Figure 4.11.: Vertex χ^2/ndf distributions of MC truth signal D^* (red curve) and minimum bias data fake D^* (blue curve). The vertex quality for fake D^* background decays is not significantly worse than for signal D^* decays.

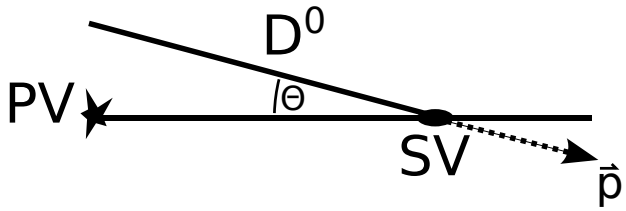

Figure 4.12.: The direction angle, dira = cos (Θ), is defined as the cosine of the angle between the D^0's momentum and the connecting line of the primary and the secondary vertex.

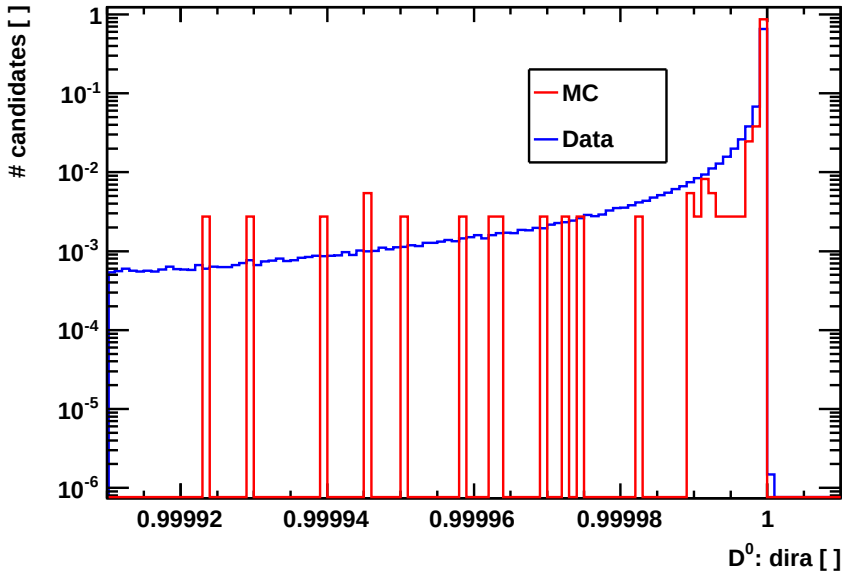

Figure 4.13.: Direction angle (dira) distributions of MC truth signal D^0 (red curve) and minimum bias data fake D^0 (blue curve). Fake D^0 candidates do not point back to the primary vertex. They are most likely produced in displaced B decays.

form of a logarithmic likelihood function, see section 2.2.2. In the case $DLL(K-\pi) > 0$ it is more likely to have reconstructed a kaon, while in the other case $DLL(K-\pi) < 0$ it is more likely to have reconstructed a pion. For the selection of WS events, it is crucial not to misidentify the D^0 daughters, hence, the DLL cuts are important for this selection. Nevertheless, the DLL simulation is not perfect yet. This is a common well known problem among the experiment. The development of a correct simulation of the DLL is still under investigation. The DLL distributions of minimum bias fake D^0 daughters and soft pions compared to the distributions of signal D^0 daughters and soft pions are shown in figure 4.14, figure 4.15 and figure 4.16.

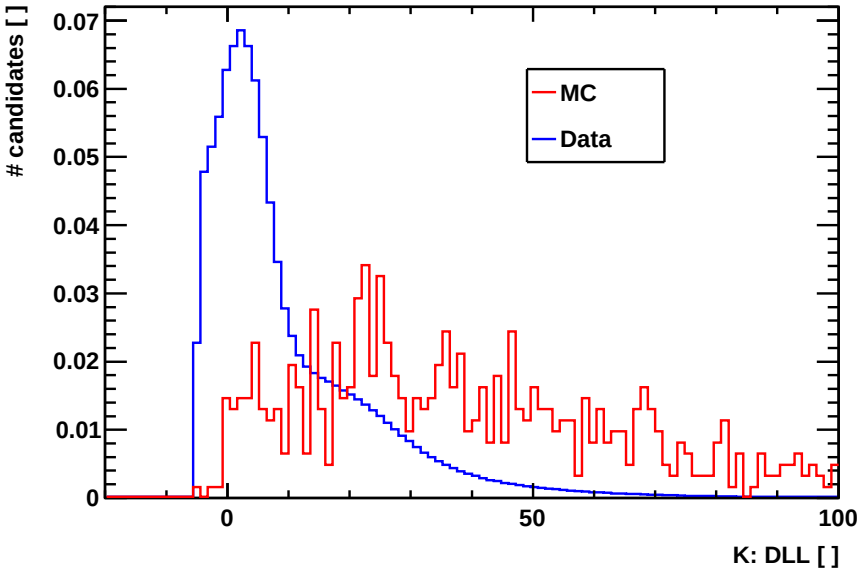

Figure 4.14.: Delta Log Likelihood (DLL) distributions of MC truth signal D^0 daughter kaons (red curve) and minimum bias data fake D^0 daughter kaons (blue curve). The simulation of this particle hypothesis quantity is not perfect yet.

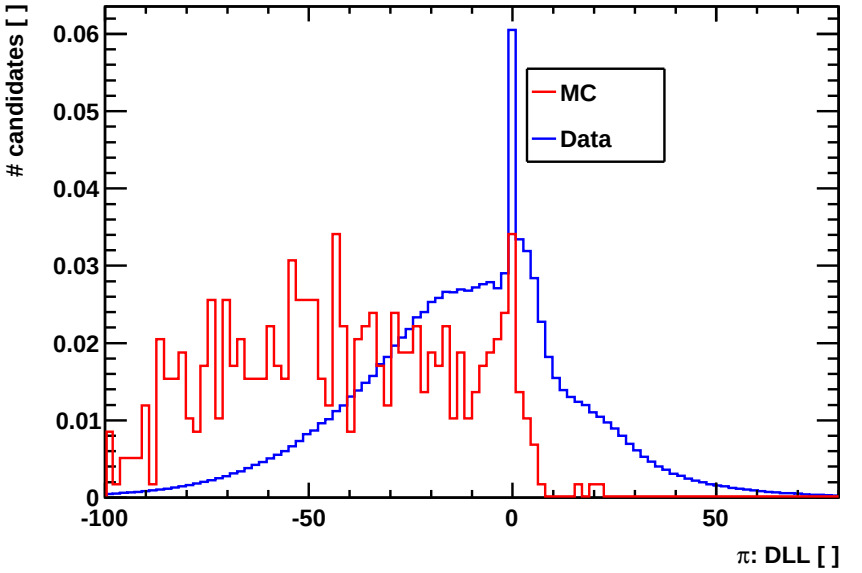

Figure 4.15.: Delta Log Likelihood (DLL) distributions of MC truth signal D^0 daughter pions (red curve) and minimum bias data fake D^0 daughter pions (blue curve). The simulation of this particle hypothesis quantity is not perfect yet.

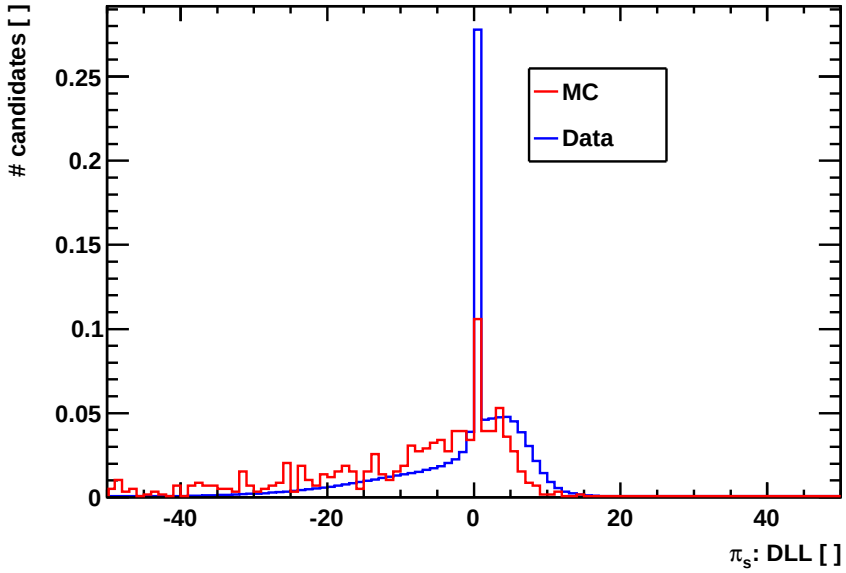

Figure 4.16.: Delta Log Likelihood (DLL) distributions of MC truth signal soft pions (red curve) and minimum bias data fake soft pions (blue curve).

D^0 Mass Swap

A cut on the swapped D^0 mass is an instrument against the double misidentification background, see section 4.1.3. True WS signal D^0 candidates peak very clearly at the D^0 mass resonance. While double misidentified background D^0 candidates, reconstructed from kaons and pions with interchanged mass hypotheses, have a very broad mass distribution around the D^0 mass. The D^0 mass swap cut is applied to D^0 events after their masses are recalculated with the swapped daughters mass hypotheses. Events are vetoed, when their swapped D^0 mass is within $m_{D^0} \pm 2\sigma = [1842, 1881]\,\text{MeV}$. Figure 4.17 shows the recalculated D^0 mass distributions with swapped daughters mass hypotheses. The MC truth signal D^0 mass distribution, before the daughters swapping up to 98% within the $m_{D^0} \pm 2\sigma = [1842, 1881]\,\text{MeV}$ cut interval, becomes after the daughters swapping a very broad distribution, not the scale of the x-axis. The fake D^0 mass distribution does not show clear peaking behavior around the D^0 mass resonance after the daughters swapping, because the double misidentification background is superimposed by the combinatorial fake D^0 background.

4.2.4. Displacement Cuts

The LHC*b* experiment was designed to resolve the displaced vertices of B and D mesons. In hadronic interactions this is an essential feature, because the events are full of prompt hadronic background. By requiring that signal events must have a minimum distance to the primary vertex (PV), the prompt background is rejected.

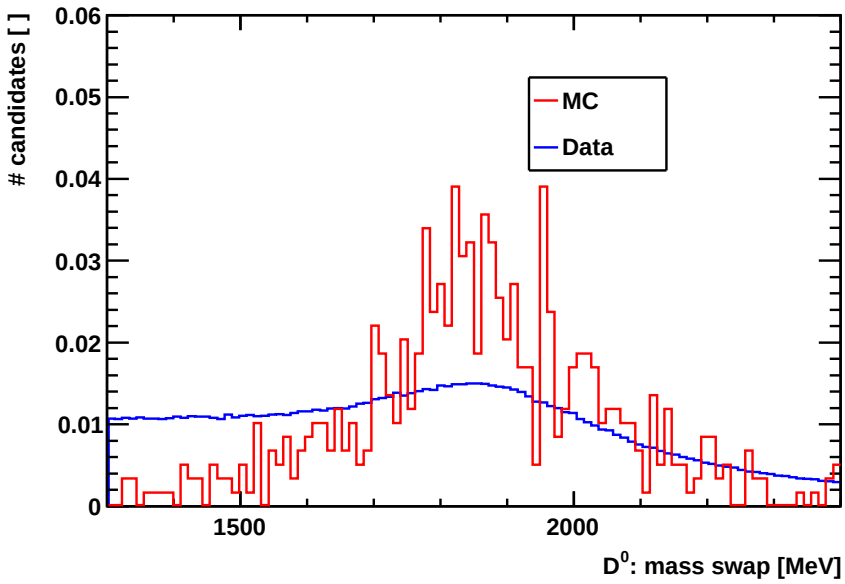

Figure 4.17.: Recalculated D^0 mass distributions after the daughters mass hypotheses are swapped for MC truth signal D^0 (red curve) and minimum bias data fake D^0 (blue curve). The now clearly peaking double misidentification background is superimposed by combinatorial fake D^0 background in data. Note the wide mass range on the x-axis. The cut interval is $m_{D^0} \pm 2\sigma = [1842, 1881]\,\text{MeV}$.

Impact Parameter χ^2

The impact parameter (IP) is defined as the perpendicular distance of the track to the PV, see figure 4.18. To require that the D^0 daughters do not come from the PV but from the displaced D^0 decay vertex a cut on a minimum IP is done. The IP error estimate can be factored into this cut by using not the IP variable itself but the IP significance variable. It is defined as the ratio of the IP divided by the error estimate on the IP fit $\frac{IP}{IP_{error}}$. The IP χ^2 is the squared impact parameter significance. Considering also the IP error the goodness of the IP determination can be evaluated and decided whether to trust or not. Hence, a cut on the IP significance is preferred. The IP χ^2 distributions for MC truth signal D^0 daughters and fake D^0 daughters are shown in figure 4.19. The fake D^0 daughters are mainly prompt, they peak clearly at IP $= 0$. So, this is a very powerful cut to reject prompt combinatorial background. For D^* and π_s the IP significance cut is chosen to be a maximum limit, because the lifetime of the D^* is that short, that it decays prompt. The soft pion then, a decay product of the prompt D^*, seems to be produced directly in the primary vertex. The IP significance distributions for MC truth signal D^* and π_s compared to minimum bias data fake D^* and π_s are shown in figure 4.20 and figure 4.21.

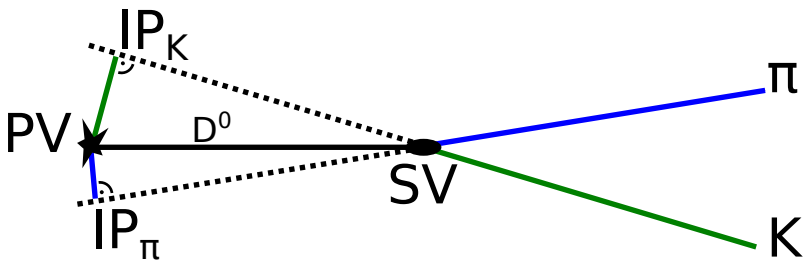

Figure 4.18.: The D^0 daughters K, π are produced in the secondary vertex (SV), that is the decay vertex of the D^0. The K, π tracks are extrapolated backwards to the primary vertex (PV). The minimal (perpendicular) distance between the PV and the extrapolated tracks is defined as the impact parameter (IP) of these tracks.

Primary Vertex displacement χ^2

The Primary Vertex displacement χ^2 (PV disp χ^2) is the squared flight distance significance of the D^0. Due to its non zero lifetime, the D^0 flies a certain distance before it decays. To suppress prompt hadronic background this cut quantity is therefore similar to the IP χ^2 cut on the D^0 daughters. The PV disp χ^2 distributions for MC truth signal D^0 compared to minimum bias data fake D^0 candidates are shown in figure 4.22. The main part of the fake D^0 background is combinatorial prompt background, hence, this is a very powerful cut.

4.2.5. Candidate per Event Selection Criterion

The reconstruction algorithms provide several candidates per event, see figure 4.23, to use all information of the event. If still more than one candidate per event remain after the final signal selection, the one with the best D^0 vertex $\frac{\chi^2}{ndf}$ is chosen. This selection criterion was compared to choosing the candidate with the best D^* vertex $\frac{\chi^2}{ndf}$. No significant difference was observed.

4.3. Signal Significance Optimization

The WS selection is optimized for a maximum signal significance

$$\sigma_{sig} = \frac{\text{signal}}{\sqrt{\text{signal} + \text{background}}} \,. \tag{4.5}$$

Here, the same categories for signal and background are taken as in the previous section, see section 4.4.

The signal significance optimization process is an iterative process. After a set of cut variables is set up, the interplay of these cuts need to be optimized. This is done with the "$n-1$" technique. If the selection has n cuts, $n-1$ cuts are fixed to preliminary values, then the n^{th} cut is varied to find the best σ_{sig}. In this section only the last step's signal significance plots are given, determined with the final cut values, to follow the choice of the final selection cuts. The optimization curves for the cut quantities, that are not included in the final selection, are given in the appendix A.

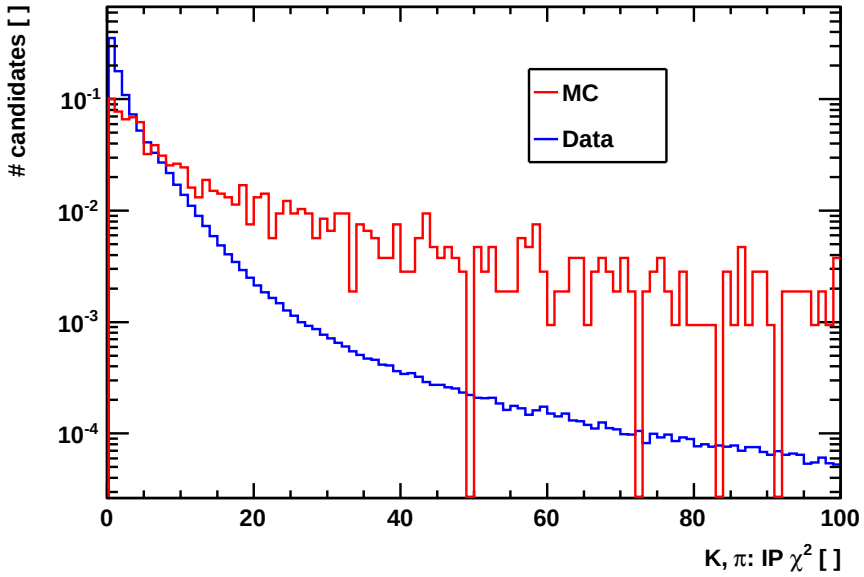

Figure 4.19.: IP χ^2 distributions of MC truth signal D^0 daughters (red curve) and minimum bias data fake D^0 daughters (blue curve). The fake D^0 daughters are mainly prompt background, peaking at an IP $= 0$ value.

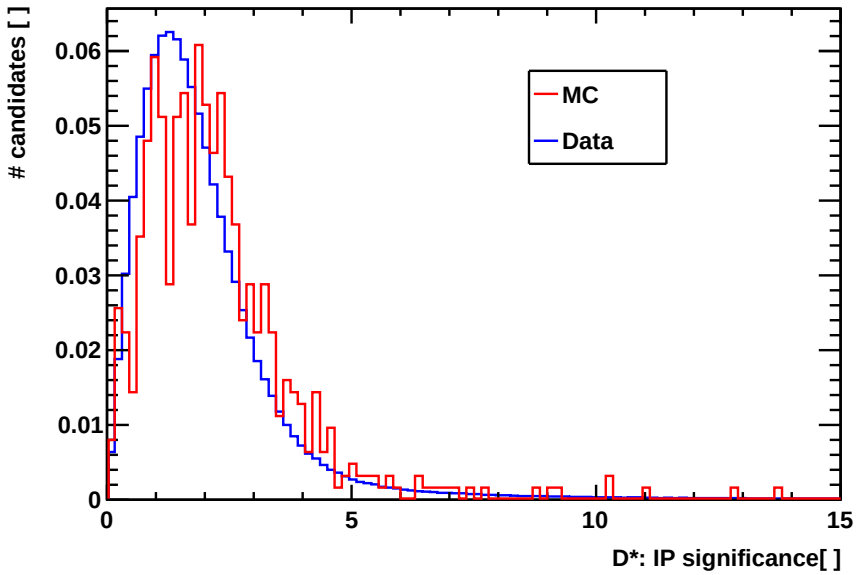

Figure 4.20.: IP significance distributions of MC truth signal D^* (red curve) and minimum bias data fake D^* (blue curve). The signal D^* decays prompt.

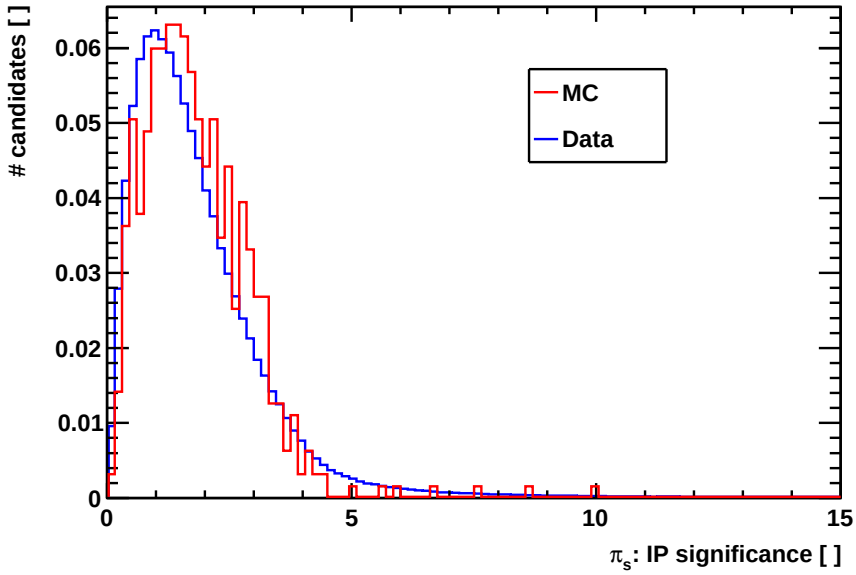

Figure 4.21.: IP significance distributions of MC truth signal π_s (red curve) and minimum bias data fake π_s (blue curve). The π_s is a decay product of the prompt decaying D^*.

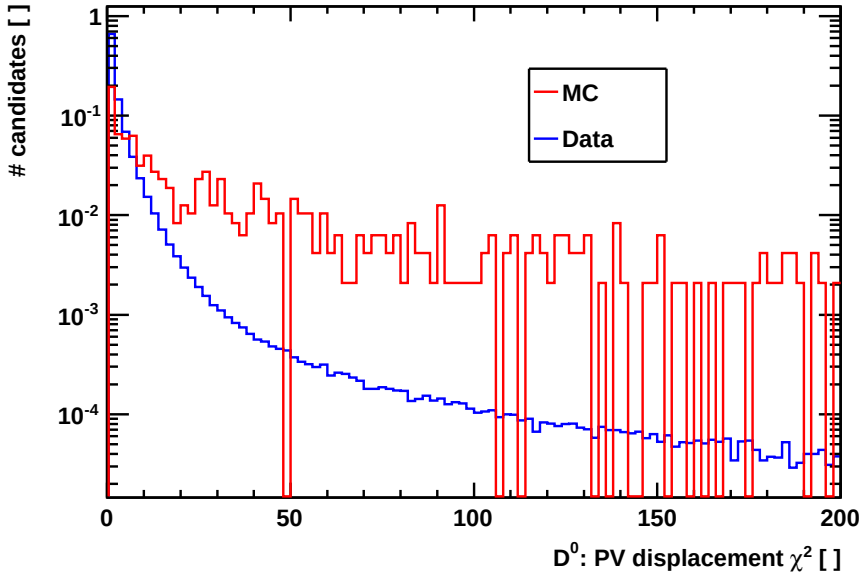

Figure 4.22.: PV disp χ^2 distributions of MC truth signal D^0 (red curve) and minimum bias data fake D^0 (blue curve). The fake D^0 are mainly combinatorial prompt background, they are not signal D^0, flying a certain distance before they decay.

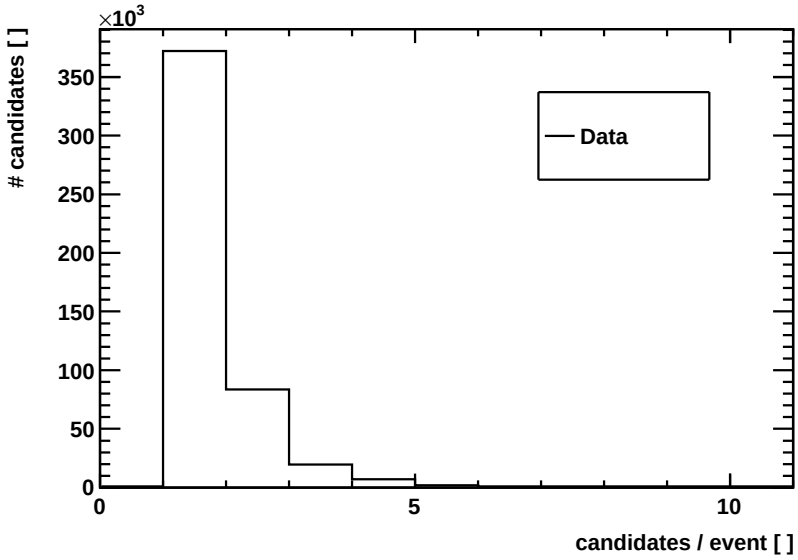

Figure 4.23.: Data: Number of reconstructed D^0 candidates per event. Selected is the D^0 candidate in every event with the best D^0 vertex $\frac{\chi^2}{ndf}$.

The statistics of the signal and background categories are limited. Hence, the signal significance curves have to be treated with care for not being victim of statistical fluctuations. Therefore, the in the previous section, see section 4.4, calculated relative cut efficiencies are given with statistical errors.

Another problem arises during the significance maximization, if the distributions of one quantity look very different in data compared to MC. For this thesis all data and MC candidates are reconstructed with the reconstruction version 04. In this version there are known problems of the particle identification simulation. Hence, this selection optimization will be improved with later alignment and reconstruction versions.

4.3.1. D^0 Daughters Quantities

Figure 4.24 shows the optimization curve corresponding to the transverse momentum distribution p_T of the D^0 daughters K, π. A maximum signal significance is obtained at a p_T cut of around 500 MeV.

Figure 4.25 shows the optimization curve corresponding to the impact parameter χ^2 distribution of the D^0 daughters K and π. For the D^0 daughters, originating in the displaced D^0 vertex, a cut on the IP χ^2 is a minimum requirement. It is a measure on how good the kaons and pions are reconstructed with a clear spacial separation from the primary vertex. Due to the huge amount of hadronic background coming directly from the primary vertex this is a very effective cut. It is placed at $IP\chi^2 > 6$.

Figure 4.26 shows the optimization curve corresponding to the delta log likelihood (DLL) distribution of the kaon, one of the D^0 daughters K and π. Choosing an optimal cut value for the

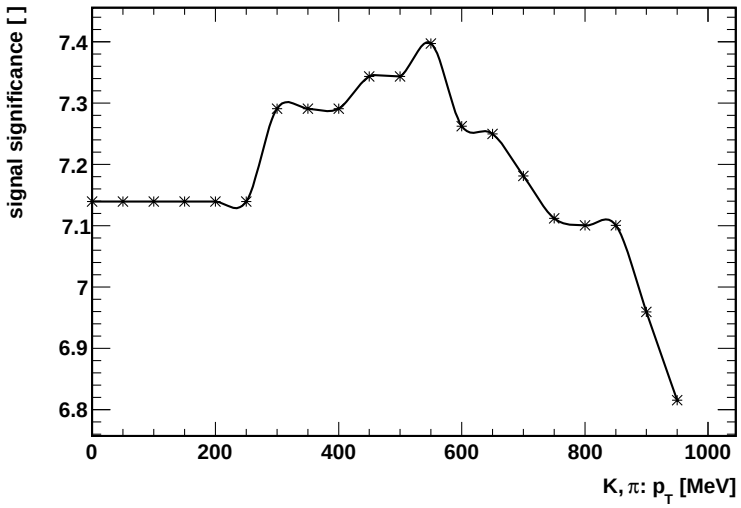

Figure 4.24.: K, π: Cut optimization curve of the transverse momentum (p_T) distribution, maximizing the total signal significance σ_{sig} of the decay. The optimal transverse momentum cut value is chosen at $p_T > 500\,\mathrm{MeV}$.

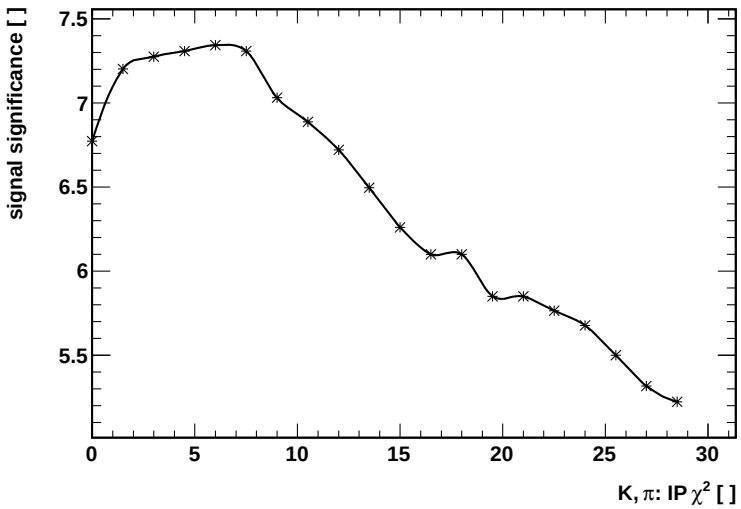

Figure 4.25.: K, π: Cut optimization curve of the impact parameter (IP) χ^2 distribution, maximizing the total signal significance σ_{sig} of the decay. The optimal IP χ^2 cut value is chosen at $IP\chi^2 > 6$.

DLL quantity in this early reconstruction version is not possible, because the distribution shapes in data and MC differ a lot. It cannot be guaranteed, that this quantity is sufficiently described by the MC simulation. Nevertheless, to have a minimum separation power between kaons and pions, the DLL cut for kaons is chosen to be well above zero, while the DLL cut for pions is chosen to be well below zero. Here, the kaon's DLL cut is $DLL(K) > 8$. Figure 4.26 shows for $DLL > 30$ signal significance values of -1. This is a technical solution for the case that the number of signal or background events after the final selection is zero. To calculate in this case the signal significance is not defined mathematically.

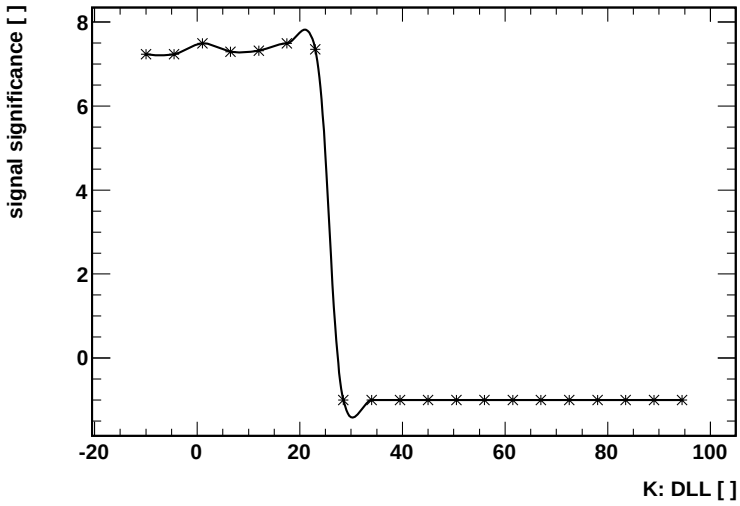

Figure 4.26.: K: Cut optimization curve of the Delta Log Likelihood (DLL) distribution, maximizing the total signal significance σ_{sig} of the decay. The DLL cut value is chosen at $DLL > 8$.

Figure 4.27 shows the optimization curve corresponding to the delta log likelihood (DLL) distribution of the pion, one of the D^0 daughters K and π. As described above for figure 4.26 the simulation of this quantity in MC is not optimal yet, hence, the cut optimization is also not optimal yet. To guarantee a minimum separation power here, the cut is placed well below zero, $DLL(\pi) < -5$.

4.3.2. D^0 Quantities

Figure 4.28 shows the signal significance optimization curve corresponding to the direction angle (dira) distribution of the D^0. This cut has not a good signal significance power, the y-axis is fluctuating in $\sigma_{sig} \pm 0.2$. Nevertheless, the dira cut is included in the final selection, to suppress D^0 from B decays.

Figure 4.29 shows the signal significance optimization curve corresponding to the primary vertex (PV) displacement χ^2 distribution of the D^0. The PV displacement χ^2 cut is set to $\chi^2 > 36$. This cut has a very good background suppression power. It is an indirect D^0 lifetime cut, because it is

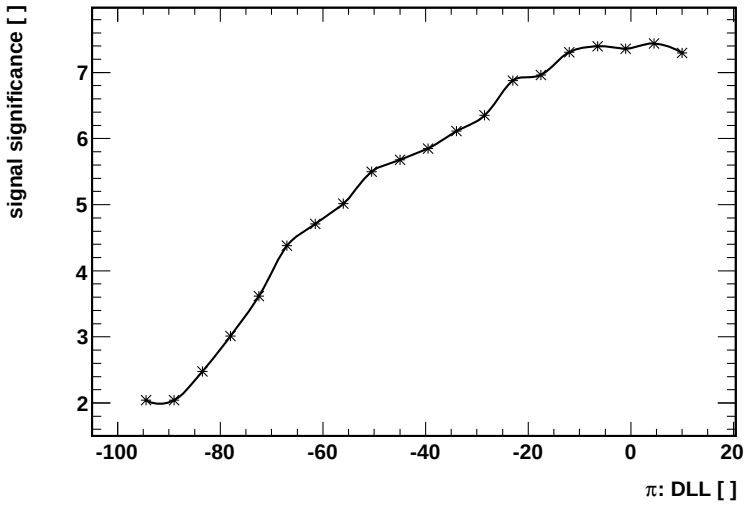

Figure 4.27.: π: Cut optimization curve of the Delta Log Likelihood (DLL) distribution, maximizing the total signal significance σ_{sig} of the decay. The DLL cut value is chosen at $DLL < -5$.

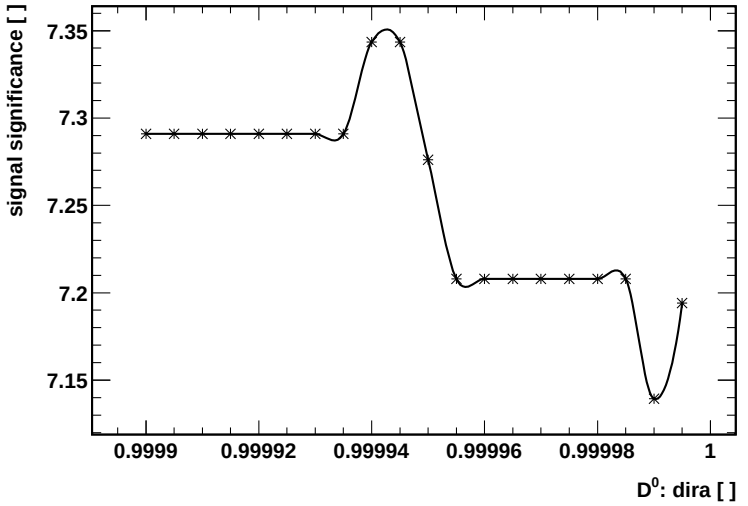

Figure 4.28.: D^0: Cut optimization curve of the direction angle (dira) distribution, maximizing the total signal significance σ_{sig} of the decay. The dira cut value is chosen at $dira > 0.99994$. The significance power of this cut is bad, nevertheless, it is included in the final selection to suppress D^0 from B decays.

proportional to the D^0 flight distance divided by the D^0 flight distance error squared. Requiring a certain proper time or flight length of a D^0 meson, suppresses very good combinatorial background.

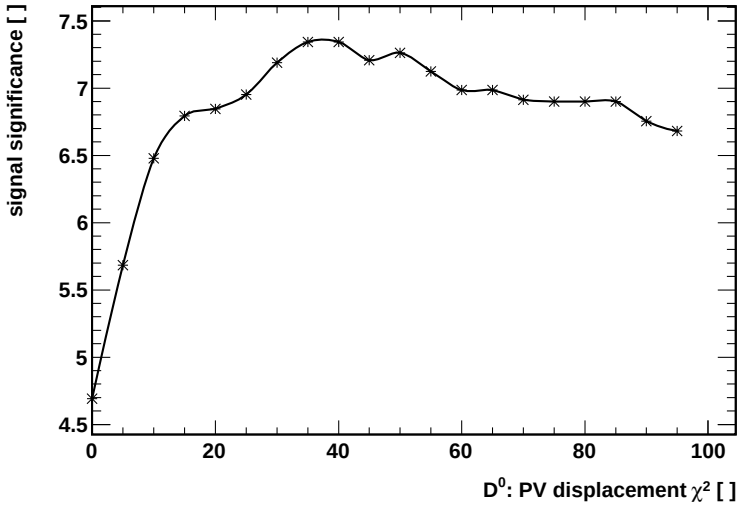

Figure 4.29.: D^0: Cut optimization curve of the Primary Vertex displacement χ^2 distribution, maximizing the total signal significance σ_{sig} of the decay. The χ^2 cut value is chosen at $\chi^2 > 36$. It has an excellent background suppression power.

Figure 4.30 shows the signal significance optimization curve corresponding to the D^0 mass distribution with swapped daughters' mass hypotheses. This cut was developed to suppress physics background, i.e. the double misidentification background, see section 4.1.3. On the x-axis the total cut interval width around the mass mean value, maximum limit minus minimum limit, is shown. The swap cut is chosen to exclude swapped masses in $m_{D^0} \pm 2\sigma = [1842, 1881]\,\mathrm{MeV}$, with the reconstructed mean D^0 mass value of $m_{D^0} = 1862\,\mathrm{MeV}$. The MC truth signal candidates, that enter in the signal significance calculation here, do not contain any background candidates, thus, they do not contain swapped D^0 daughters background. Hence, the choice of the limits of this cut is not determined by the signal significance curve, here, but it is determined by physical reasons. Nevertheless, figure 4.30 shows that the pure signal loss is not too high due to this cut, the significance curve stagnates at high level in the chosen cut region.

4.3.3. D^* and π_s Quantities

Figure 4.31 shows signal significance optimization curve corresponding to the transverse momentum distribution of the D^*. The cut is chosen to be at $p_T > 2200\,\mathrm{MeV}$. Cutting on the transverse momentum of the D^* has quite some background suppression power in this selection configuration. Figure A.3 shows negative values for the signal significance for $p_T > 6000\,\mathrm{MeV}$, because above these cut values, no signal or no background candidates are left over. Hence, the signal significance is mathematically not defined. Here, these undefined values are set to -1 explicitly.

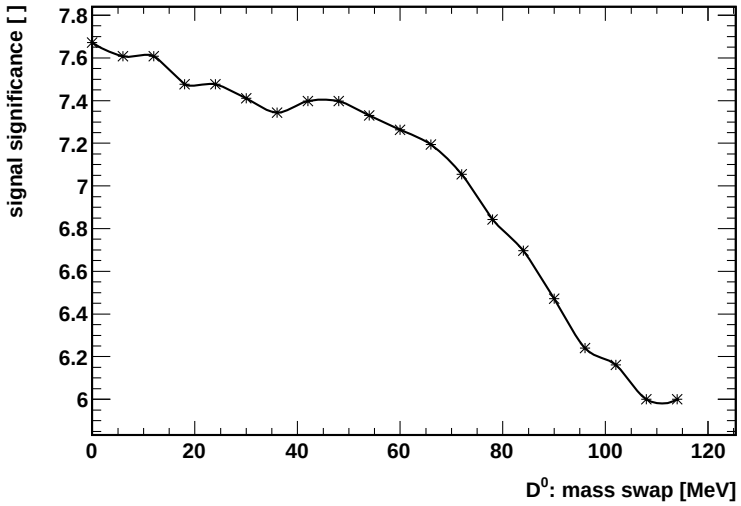

Figure 4.30.: D^0: cut optimization curve of the recalculated D^0 mass distribution with swapped daughters mass hypotheses, maximizing the total signal significance σ_{sig} of the decay. The cut excludes recalculated D^0 masses in $m_{D^0} \pm 2\sigma = [1842, 1881]\,\text{MeV}$. The x-axis shows the difference of the maximum limit minus the minimum cut limit. Hence, the chosen cut is located at $x = 39\,\text{MeV}$. Due to the fact, that the MC signal entries, entering here into the signal significance calculation, are pure signal entries only, containing no double misidentified D^0 daughters, the optimization curve shows signal loss only.

Figure 4.32 shows the signal significance optimization curve corresponding to the impact parameter significance (IP_{sig}) distribution of the D^*. The cut is chosen to be at $IP_{sig} < 5$.

Figure 4.33 shows the optimization curve corresponding to the delta log likelihood (DLL) distribution of the π_s. As described above for figure 4.26 the simulation of this quantity in MC is not optimal yet, hence, the cut optimization is also not optimal yet. The cut is placed at zero, $DLL(\pi) < 0$, because in this case the mix-up of kaons and pions is not as probable as in the D^0 daughters' case.

4.4. WS Selection Efficiency

In the previous section the optimal cuts were found by an iterative optimization process. Thereby it turned out, that the entire selection leads to many correlation affects. Cutting in one variable quite hard makes another cut useless. These correlations can be quantified in the following way. First, to illustrate, that every cut on its own is very effective, a total selection efficiency per cut is calculated. Second, to illustrate, that the cut correlations make some cuts useless, a relative selection efficiency per cut i is calculated. The total selection efficiency per cut i is defined as, see

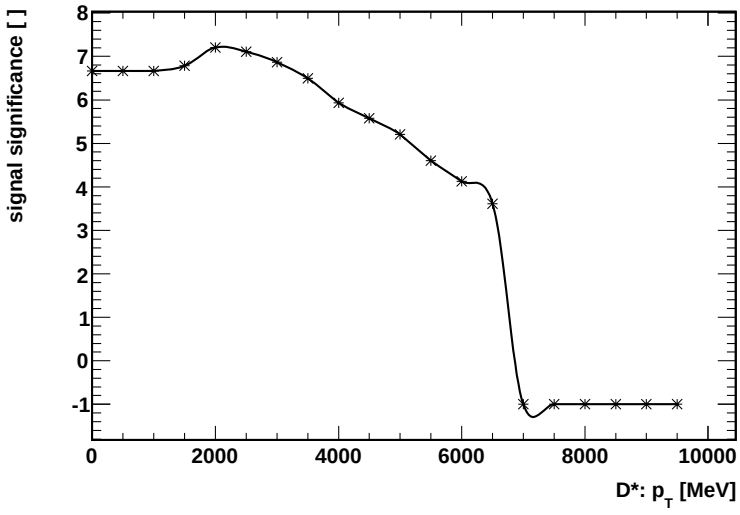

Figure 4.31.: D^*: Cut optimization curve of the transverse momentum (p_T) distribution, maximizing the total signal significance σ_{sig} of the decay. The p_T cut value is chosen at $p_T > 2200\,\text{MeV}$. The signal significance is set to -1, when no signal or background candidates are left over to calculate the significance.

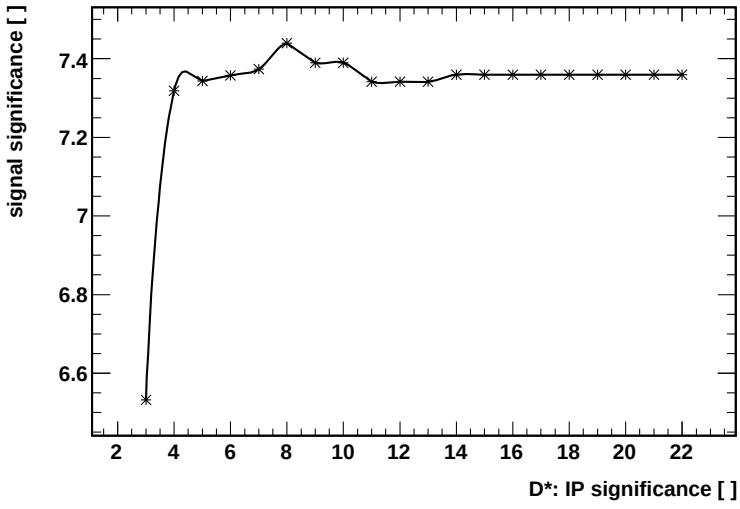

Figure 4.32.: D^*: Cut optimization curve of the impact parameter significance (IP_{sig} distribution, maximizing the total signal significance σ_{sig} of the decay. The IP_{sig} cut value is chosen at $IP_{sig} < 5$.

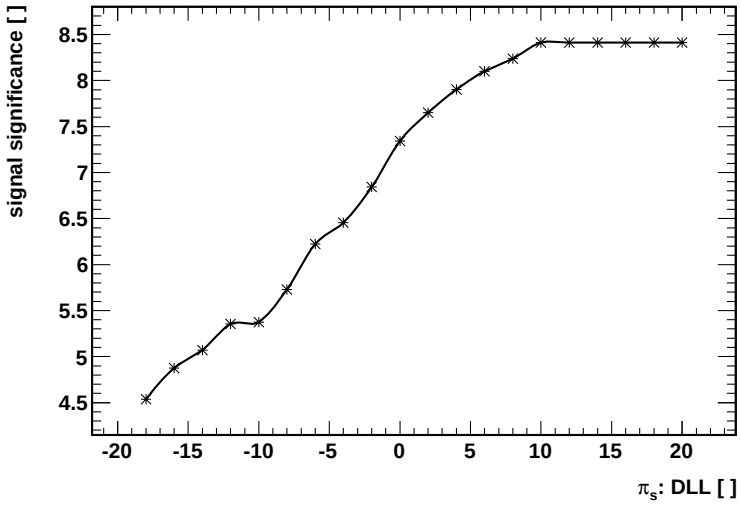

Figure 4.33.: π_s: Cut optimization curve of the Delta Log Likelihood (DLL) distribution, maximizing the total signal significance σ_{sig} of the decay. The DLL cut value is chosen at $DLL < 0$. The DLL simulation in MC is not perfect yet.

equation 4.6:

$$\epsilon_i = \frac{\#\text{ candidates after cut i applied}}{\#\text{candidates after preselection}} \tag{4.6}$$

The total signal loss and background suppression, which is the very same quantity as the signal loss but simply has a different meaning, are defined as $1 - \epsilon_i$. The corresponding numbers are shown in table 4.3. The relative selection efficiency per cut i, while the other $N-1$ cuts are fixed, is defined as, see equation 4.7:

$$\epsilon_i^{N-1} = \frac{\#\text{ candidates after selection applied}}{\#\text{candidates after selection without cut i}} \tag{4.7}$$

The relative signal loss and background suppression, again this is the very same quantity as the signal loss but simply has a different meaning, are defined as $1-\epsilon_i^{N-1}$. The corresponding numbers are shown in table 4.4.

Table 4.3 shows that almost every cut has excellent background suppression power. Nevertheless, table 4.4 demonstrates that there are big correlations between these final cuts. Additionally, during the cut value optimization process it was considered, that in the end, this selection is not applied to minimum bias data, but to signal data, that have passed a certain stripping selection. A stripping selection is comparable with a mediate, not very loose but also not to tight, preselection. To achieve the best selection results on the stripped data, the final selection has to be at least as hard as the stripping selection in every cut. The stripping selection[4] cuts, that filtered

[4]Stripping 07: StrippingDstarPromptWithD02HH.py

Particle	Cut Variable		Cut Value	Signal Loss total	Background Suppression total
hh	p	$>$	5000 MeV	0.10 ± 0.03	0.51 ± 0.00
hh	p_T	$>$	500 MeV	0.19 ± 0.04	0.61 ± 0.00
hh	Track $\chi^2/ndof$	$<$	5	0.01 ± 0.01	0.04 ± 0.00
hh	Ip χ^2	$>$	6	0.51 ± 0.02	0.96 ± 0.00
K	DLL (K-π)	$>$	8	0.11 ± 0.03	0.61 ± 0.00
π	DLL (K-π)	$<$	-5	0.11 ± 0.00	0.43 ± 0.01
D^0	p_T	$>$	1000 MeV	0.01 ± 0.01	0.44 ± 0.00
D^0	Vertex $\chi^2/ndof$	$<$	10	0.01 ± 0.01	0.01 ± 0.00
D^0	dira	$>$	0.99994	0.43 ± 0.04	0.55 ± 0.01
D^0	PV disp χ^2	$>$	36	0.50 ± 0.02	0.98 ± 0.00
D^0	mass swap		$m_{D^0} \pm 2\sigma$	0.10 ± 0.02	0.04 ± 0.00
π_s	DLL (K-π)	$<$	0	0.31 ± 0.01	0.64 ± 0.00
π_s	Track $\chi^2/ndof$	$<$	5	0.02 ± 0.01	0.09 ± 0.00
π_s	p_T	$>$	110 MeV	0.00 ± 0.00	0.00 ± 0.00
π_s	Ip sig	$<$	5	0.01 ± 0.00	0.04 ± 0.00
D^*	p_T	$>$	2200 MeV	0.25 ± 0.03	0.88 ± 0.00
D^*	Vertex $\chi^2/ndof$	$<$	13	0.00 ± 0.00	0.01 ± 0.00
D^*	Ip sig	$<$	5	0.06 ± 0.00	0.05 ± 0.00

Table 4.3.: WS Signal Selection: Total Cut Efficiency. The total Signal Loss and total Background Suppression are calculated in the very same way: $1 - \epsilon_i$. ϵ_i is the total selection efficiency per cut i, given in equation 4.6.

the in this thesis analyzed data are also given in table 4.4. Considering these cut quantities and cut values, will also make the choice of the final selection cuts more comprehensible.

Due to the cut correlations, the total number of cuts was reduced from 18 to 10. It turned out, that cutting on the D^0 daughters p_T, $IP\chi^2$, DLLs, the D^0s dira, PV displacement χ^2, mass swap, the π_s DLL and on the D^* p_T and IP_{sig} is sufficient. Hence, the cuts on all track and vertex χ^2 quantities became useless. Also the cut on the momenta of the D^0 daughters, the p_T cut of the D^0 and the π_s and the IP_{sig} cut of the π_s were not needed any more.

The errors on the total and the relative selection efficiencies were calculated by dividing the entire signal and background samples each into three parts of equal size. For every subsample the selection efficiencies were calculated. The entire sample represents the mean values of the efficiencies, while the subsamples efficiencies represent the statistical deviations from the mean values. The maximum deviation is quoted as the efficiency's error in table 4.3 and table 4.4.

Particle	Cut Variable	Stripping	Cut Value	Signal Loss relative	Background Suppression relative
hh	p	$>$ 5000 MeV	$>$ 5000 MeV	0.00 ± 0.00	0.11 ± 0.14
hh	p_T	$>$ 500 MeV	$>$ 500 MeV	0.00 ± 0.00	0.33 ± 0.17
hh	Track $\frac{\chi^2}{ndof}$	$<$ 10	$<$ 5	0.00 ± 0.00	0.00 ± 0.00
hh	Ip χ^2	$>$ 4	$>$ 6	0.08 ± 0.04	0.72 ± 0.10
K	DLL (K-π)		$>$ 8	0.12 ± 0.11	0.64 ± 0.07
π	DLL (K-π)		$<$ -5	0.05 ± 0.09	0.53 ± 0.20
D^0	p_T	$>$ 1000 MeV	$>$ 1000 MeV	0.00 ± 0.00	0.00 ± 0.00
D^0	Vertex $\frac{\chi^2}{ndof}$	$<$ 10	$<$ 10	0.02 ± 0.03	0.00 ± 0.00
D^0	dira		$>$ 0.99994	0.27 ± 0.09	0.43 ± 0.07
D^0	PV disp χ^2	$>$ 16	$>$ 36	0.09 ± 0.06	0.94 ± 0.01
D^0	mass swap		$m_{D^0} \pm 2\sigma$	0.08 ± 0.02	0.00 ± 0.00
π_s	DLL (K-π)		$<$ 0	0.26 ± 0.11	0.38 ± 0.05
π_s	Track $\frac{\chi^2}{ndof}$	$<$ 10	$<$ 5	0.00 ± 0.00	0.00 ± 0.00
π_s	p_T	$>$ 110 MeV	$>$ 110 MeV	0.00 ± 0.00	0.00 ± 0.00
π_s	Ip sig		$<$ 5	0.00 ± 0.00	0.20 ± 0.20
D^*	p_T	$>$ 2200 MeV	$>$ 2200 MeV	0.08 ± 0.11	0.75 ± 0.08
D^*	Vertex $\frac{\chi^2}{ndof}$		$<$ 13	0.00 ± 0.00	0.00 ± 0.00
D^*	Ip sig		$<$ 5	0.06 ± 0.05	0.47 ± 0.23

Table 4.4.: WS Signal Selection: Relative Cut Efficiency. The relative Signal Loss and relative Background Suppression are calculated in the very same way: $1 - \epsilon_i^{N-1}$. ϵ_i^{N-1} is the relative selection efficiency per cut i, given in equation 4.7.

4.5. Final WS Selection

Figure 4.34 (a) shows again the signal and background samples, the selection was optimized with. Now, having found the optimal final WS selection after this quite long optimization process, figure 4.34 (b) shows the same signal and background samples after they were filtered by the final selection. A clear D^0 mass peak of signal decays remains and almost all fake D^0 decay background is suppressed. This was the goal of the whole selection optimization process.

That the selection optimization has worked can also be expressed in numbers. After the very loose preselection the signal to background ratio in the optimization samples was

$$\frac{\text{Signal}}{\text{Background}}(\text{Preselection}) = \frac{634}{1490198} = 4.3 \cdot 10^{-4}\,, \tag{4.8}$$

while after the events were filtered by the final selection the ratio is improved by a factor of 10^4:

$$\frac{\text{Signal}}{\text{Background}}(\text{Final selection}) = \frac{61}{8} = 7.6\,. \tag{4.9}$$

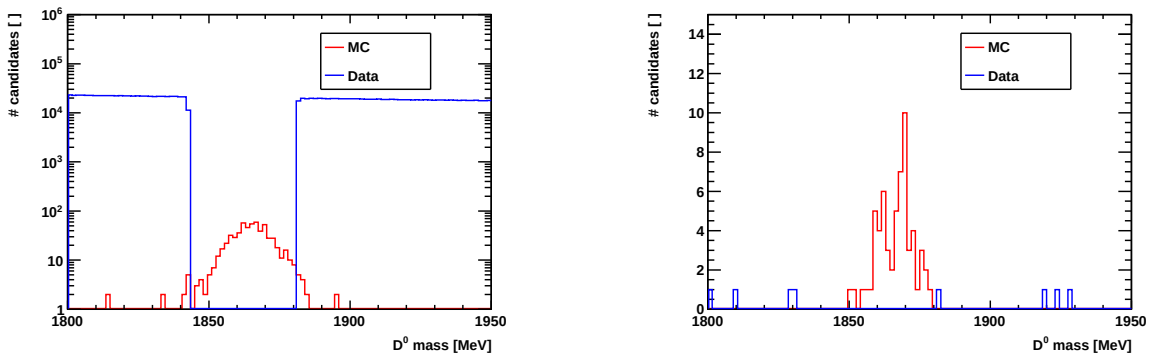

(a) Preselection applied

(b) Final Selection applied

Figure 4.34.: MC truth signal D^0 decays (red curve) and minimum bias data fake D^0 decays background (blue curve). (a) Starting point for the selection optimization process, the candidates were just filtered by the very loose preselection. (b) The final selection was applied. A clear WS signal D^0 decay mass peak remains.

Sure, the signal loss by a factor of 10^1 is not that amazing, but the same selection has suppressed the background by a factor of 10^5. Considering the different integrated luminosities of the samples, mentioned before in the beginning of this chapter, but also the background increasing factors by leaving the D^0 mass and the ΔM window open used here, in data the signal to background ratio is expected to be more like:

$$\frac{\text{Signal}}{\text{Background}}(\text{Final selection}) = \frac{61}{8 \times {}^{500}/_{27}} = 0.4\,. \tag{4.10}$$

Nevertheless, the remaining $8 \times {}^{500}/_{27}$ background events, are flatly distributed in the D^0 mass window, they do not peak within the signal D^0 mass peak. Also estimates concerning the physics background in data can be derived from the MC selection optimization. The number of double misidentification background fake WS decays is after the final selection without applying the mass swap cut reduced by a factor of 98.9 %. The mass swap cut has a double misidentification background rejection of 97 % and an signal efficiency of 85 %. Due to the branching ratios of RS and WS decays, 260 RS decays occur per WS decay. After filtering these events with the final selection without the swap cut, but mainly with the particle identification cuts, this ratio decreases to 2.9 RS decays per WS decay. Considering the efficiencies of the swap cut this ratio is changed to 0.09 RS decays per 0.85 WS decays. Hence, in 10 WS decays 1 RS decay is still expected to occur in data. The random soft pion background is expected to vanish completely in data due to the ΔM sideband subtraction. The final selection is given in table 4.5.

4. $D^{*+} \to D^0(K^+\pi^-)\pi^+$ Wrong Sign Selection

Particle	Cut Variable	Cut Value (final)
hh	p_T	$>$ 500 MeV
hh	Ip χ^2	$>$ 6
K	DLL (K-π)	$>$ 8
π	DLL (K-π)	$<$ -5
D^0	dira	$>$ 0.99994
D^0	PV disp χ^2	$>$ 36
D^0	mass swap	$m_{D^0} \pm 2\sigma$
π_s	DLL (K-π)	$<$ 0
D^*	p_T	$>$ 2200 MeV
D^*	Ip sig	$<$ 5

Table 4.5.: Final Selection to filter WS Signal Events in Data

5. D^0 Wrong Sign Decay Signal Yield in Data

5.1. Fit to the $\Delta M = m_{D^*} - m_{D^0}$ Distribution in MC

To determine the random soft pion background the mass difference ΔM of the D^* mass minus the D^0 mass is fitted. The fit is firstly performed in MC to show its background suppression power, in section 5.3.1 it is applied to $\mathcal{L} = 0.6\,\mathrm{pb}^{-1}$ of data and in section 5.4.1 it is applied to $\mathcal{L} = 37\,\mathrm{pb}^{-1}$ of data. The ΔM distribution is fitted by a probability density function, PDF, that is a composition of a Double-Gaussian (DG) PDF, and a modified Argus PDF, see equation 5.1. The Double-Gaussian distribution, PDF_{sig}, fits the signal decays, while the Argus distribution, PDF_{bkg}, is an appropriate model to fit the random soft pion background decays.

$$PDF(\Delta M) = n_{sig} \cdot \underbrace{DG(\Delta M; f, \mu, \sigma_1, \sigma_2)}_{PDF_{sig}} + n_{bkg} \cdot \underbrace{\mathrm{Argus}(\Delta M; \Delta M|_0, a, b, c)}_{PDF_{bkg}} \tag{5.1}$$

The Double-Gaussian signal PDF consists of two Gaussian distributions layered on top of each other with different widths but the same mean value:

$$PDF_{sig}(\Delta M; \mu, \sigma_1, \sigma_2, f) = f \frac{1}{\sqrt{2\pi\sigma_1^2}} e^{-\frac{(\Delta M-\mu)^2}{2\sigma_1^2}} + (1-f) \frac{1}{\sqrt{2\pi\sigma_2^2}} e^{-\frac{(\Delta M-\mu)^2}{2\sigma_2^2}} \tag{5.2}$$

The modified Argus PDF is implemented in the data analysis toolkit RooFit[1]. The analytical expression for this background PDF is given in equation 5.3:

$$PDF_{bkg}(\Delta M; \Delta M|_0, a, b, c) = \left(\frac{\Delta M}{a}\right)^a \cdot \left(1 - e^{-\frac{\Delta M - \Delta M|_0}{c}}\right) + b \cdot \left(\frac{\Delta M}{\Delta M|_0} - 1\right) \tag{5.3}$$

The signal and background PDF are extended PDF to fit simultaneously the number of signal (n_{sig}) and background (n_{bkg}) candidates, implemented by RooExtendPdf[2], which adds a parametric extended likelihood term to the PDF. The mean value μ of the Double-Gaussian and the turn on parameter $\Delta M|_0$ of the Argus distribution are fixed, to reduce the number of free fit parameters. Both parameters are reconstruction independent, because they rely only on the absolute mass difference of the D^* minus the D^0. Figure 5.1 shows the ΔM fit applied to WS signal decays in MC. To demonstrate the physical random soft pion background in MC, no MC truth signal information is required. The fitted ΔM distribution is divided into three areas, indicated

[1] RooDstD0BG, special PDF shape to model the background of $D^* - D^0$ mass difference distributions, http://root.cern.ch/root/html526/RooDstD0BG.html

[2] http://root.cern.ch/root/html/RooExtendPdf.html

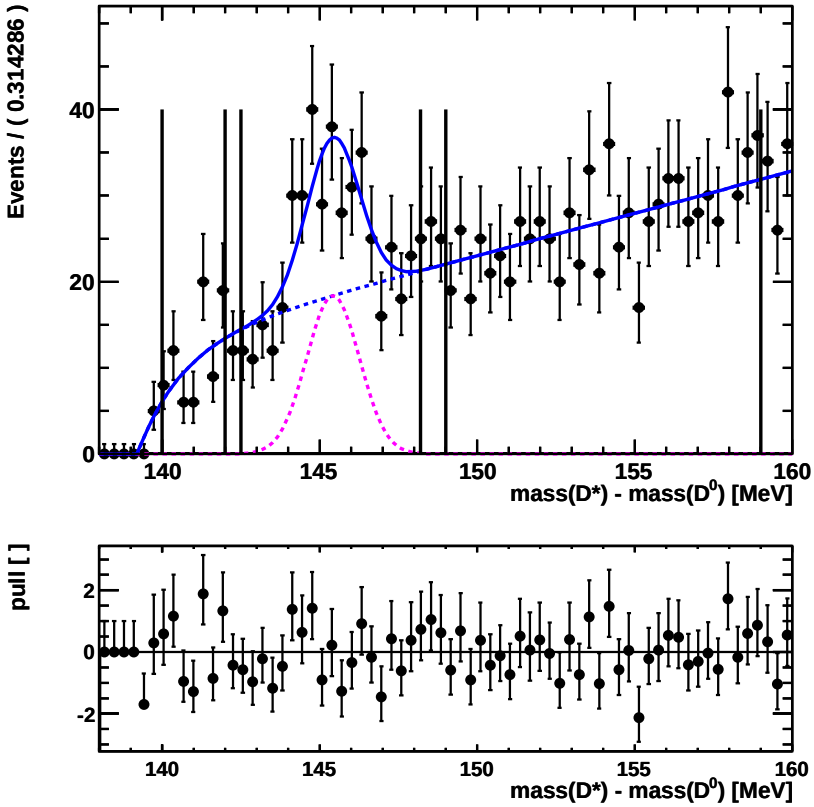

Figure 5.1.: Signal MC (no truth): Fit to the ΔM distribution of WS decays. Three regions are defined, denoted by the vertical lines. The borders of the signal window are $[142.5, 148.2]$ MeV, the first background sideband is defined in $[140.0, 142.0]$ MeV and the second background sideband is defined in $[149.0, 159.0]$ MeV. No MC truth WS signal information was required to demonstrate the physics background.

by the vertical lines in figure 5.1. The signal area is defined for ΔM in $[142.5, 148.2]$ MeV. Two combinatorial background areas are defined on the left and on the right side of the signal area for ΔM in $[140.0, 142.0]$ MeV and for ΔM in $[149.0, 159.0]$ MeV. Additionally, the signal area is divided horizontally by the signal and background components of the PDF, namely PDF_{sig} and PDF_{bkg}. The number of correctly tagged $D^{*+} \to D^0\pi^+$ decays corresponds to the area of PDF_{sig}, while the number of random soft pion decays corresponds to the part of the area of PDF_{bkg} within the signal area. In MC the ΔM fit determines 123 ± 23 signal $D^* \to D^0\pi_s$ decays and 223 ± 20 random soft pion decays. The whole set of fitted parameters is listed in table 5.1.

5.2. Fit to the D^0 Mass Distribution in MC

To separate the WS signal decays from the random soft pion background decays, which are also peaking in the D^0 mass distribution, the D^0 mass distribution is ΔM sideband subtracted.

Fit Parameter	Fitted Value
sig. cand.	122.786 ± 22.764
bkg. cand.	1442.230 ± 41.934
μ [MeV]	145.421 (const.)
σ_1 [MeV]	0.838 ± 0.137
σ_2 [MeV]	1.650 ± 1.151
fraction	1.000 ± 0.422
$\Delta M\|_0$ [MeV]	139.2 (const.)
a	1.000 ± 0.214
b [MeV]	10.000 ± 1.407
c [MeV]	1.410 ± 0.350

Table 5.1.: Parameters of the fit to the ΔM distribution of WS decays in MC. No MC truth WS signal information was required to demonstrate the physics background.

Sideband subtraction is a statistical method to remove background candidates from signal distributions. Here, the fit to the ΔM distribution provides this information to distinguish between signal and background candidates. In section 5.1 the regions of combinatorial and random soft pion background within the fitted ΔM distribution were defined. These regions are integrated, to get the number of random soft pion background events, which are below the signal peak and the number of combinatorial background events, that are in the sidebands. A statistical weight is then calculated using equation 5.4:

$$\text{weight} = \frac{\#\text{bkg. events below signal peak}}{\#\text{bkg. events in sideband(s)}} \tag{5.4}$$

The sideband subtraction is applied to all WS signal decay distributions, e.g. the D^0 mass, in the following way. During the D^0 mass histogram filling, a statistical weight is assigned to every candidate, depending on the corresponding ΔM value. The statistical weight can adopt three values, $+1$, if decay candidate's ΔM value is within the signalband, $(-1)\times$weight of equation 5.4, if the decay candidate's ΔM value is within one of the two sidebands, and 0, if the decay candidate's ΔM value is somewhere between the signal region and the background sidebands.

After the final selection, including the mass swap cut to reject double misidentification physics background, and after the ΔM sideband subtraction, that removed all random soft pion physics background, the remaining reconstructed D^0 WS decays form now a clean signal sample. The D^0 mass distribution of this clean D^0 WS decay signal sample is fitted by a Double-Gaussian distribution and a linear polynomial to describe the remaining small number of combinatorial background events, see equation 5.5:

$$PDF(m) = n_{sig} \cdot \underbrace{DG(m;\mu,\sigma_1,\sigma_2,f)}_{PDF_{sig}} + n_{bkg} \cdot \underbrace{\text{linear(m; slope)}}_{PDF_{bkg}} \tag{5.5}$$

Analogous to the PDF to fit the ΔM distribution, the signal and background PDF to fit the D^0 mass are extended PDFs fitting simultaneously the number of signal (n_{sig}) and background

(n_{bkg}) candidates. Figure 5.2 shows the fit applied to the D^0 mass distribution for MC signal candidates. For the mass distribution, no MC truth WS signal decay information was required, to demonstrate the random soft pion background suppression of the ΔM sideband subtraction in MC.

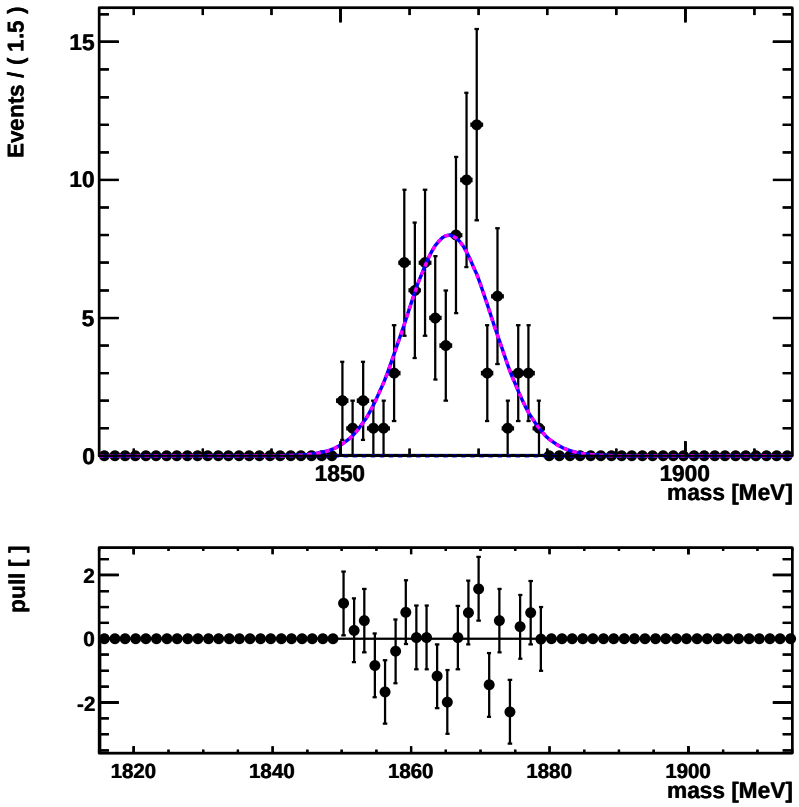

Figure 5.2.: Signal MC (no truth): Fit to the ΔM sideband subtracted D^0 mass distribution of WS decays. No MC truth WS signal information was required to demonstrate the physics background.

The D^0 mass fit determines 85 ± 9 signal $D^{*+} \to D^0\pi_s^+ \to (K^+\pi^-)\pi_s^+$ decays. No combinatorial background remains in this MC sample, because it is an exclusive signal simulation. All fitted parameters are listed in table 5.2. The ΔM fit determined 123 ± 23 signal $D^* \to D^0\pi_s$ decays in MC. Simple counting of MC associated true WS signal $D^{*+} \to D^0\pi_s^+ \to (K^+\pi^-)\pi_s^+$ decays yields 61 signal events, that is compatible with the ΔM and the mass fit result within $2.7\,\sigma$. The fit results are statistically limited. A bigger MC sample would increase the accuracy.

5.3. Stripping 07 Data Set

This section shows the results of the final WS selection applied to LHC*b* data. The data was taken in May and June 2010 with the magnet polarity down. It was preselected by the stripping

Fit Parameter	Fitted Value
sig. cand.	84.979 ± 9.112
bkg. cand.	0.333 ± 0.098
μ [MeV]	1865.730 ± 0.105
σ_1 [MeV]	6.396 ± 0.240
σ_2 [MeV]	12.055 ± 2.877
fraction	1.000 ± 0.003
slope [MeV]	0.670 ± 1.247

Table 5.2.: Parameters of the fit to the ΔM sideband subtracted D^0 mass distribution of WS decays in MC. No MC truth WS signal information was required to demonstrate the physics background.

07 data processing.[3] The recorded integrated luminosity of this data sample corresponds to $\mathcal{L} = (0.61 \pm 0.01)\,\mathrm{pb}^{-1}$.

The measurement of the number of WS signal decays is done as follows. First, the data is selected to reject the combinatorial and the double misidentification background. Second, the ΔM distribution of the remaining WS decay candidates is fitted to determine the statistical weights for the sideband subtraction. Third, the WS decay candidate distributions are sideband subtracted to suppress the random soft pion background. Finally, the D^0 mass distribution of clean WS decay events is fitted to estimate the number of WS events.

5.3.1. Fit to the ΔM Distribution in Data

The PDF to fit the ΔM distribution was introduced in section 5.1. The fit to the ΔM distribution of WS decays in data is shown in figure 5.3. The regions to calculate the statistical weight for the sideband subtraction are indicated by the vertical lines in figure 5.3. They are defined with exactly the same limits as in the MC fit, the signal window is set to $[142.5, 148.2]\,\mathrm{MeV}$ and the sidebands are set to $[140.0, 142.0]\,\mathrm{MeV}$ and $[149.0, 159.0]\,\mathrm{MeV}$.

The fit determines 142 ± 46 true $D^* \to D^0\pi_s$ decays and 713 ± 100 random soft pion background fake $D^* \to D^0\pi_s$ decays. In total 3267 ± 460 background events are fitted. All fitted parameters are listed in table 5.3. The mean value μ of the Double-Gaussian and the turn on parameter $\Delta M|_0$ of the Argus distribution are fixed, to reduce the number of free fit parameters. As explained above, both parameters are reconstruction independent, because they rely only on the absolute mass difference of the D^* minus the D^0. The weight for sideband subtraction, determined in this fit, is 0.331752.

5.3.2. Fit to the D^0 Mass Distribution in Data

The PDF to fit the ΔM sideband subtracted D^0 mass distribution was introduced in section 5.2. The fit to the ΔM sideband subtracted D^0 mass distribution of WS decays in data is shown in

[3] Stripping 07: The output of the StrippingDstarPromptWithD02HH.py line was used.

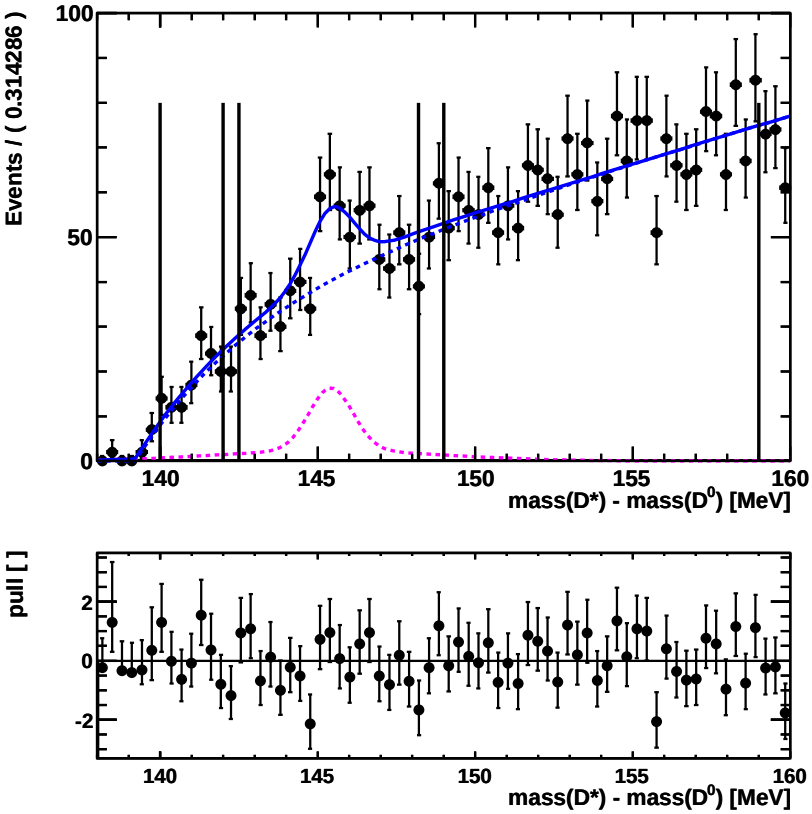

Figure 5.3.: Fit to the $\Delta M = m_{D^*} - m_{D^0}$ distribution of WS decays in $\mathcal{L} = (0.61 \pm 0.01)\,\mathrm{pb}^{-1}$ of data. The vertical lines indicate the areas for sideband subtraction. The borders of the signal window are $[142.5, 148.2]\,\mathrm{MeV}$, the first background sideband is defined in $[140.0, 142.0]\,\mathrm{MeV}$ and the second background sideband is defined in $[149.0, 159.0]\,\mathrm{MeV}$.

figure 5.4. After the final selection and the ΔM sideband subtraction, basically no background candidates remain. Hence, a clear WS $D^{*+} \to D^0\pi_s^+ \to (K^+\pi^-)\pi_s^+$ decay mass peak remains. The fit determines 114 ± 7 signal candidates and 0 ± 1 background candidates. All fit parameters are listed in table 5.4. In the previous fit to the ΔM distribution in data the number of signal $D^* \to D^0\pi_s$ decays was determined with 142 ± 46 candidates. Within the statistical errors, these estimates on the number of signal decays are compatible.

A clear WS decay signal could be measured in early LHC*b* data. With later alignment and reconstruction versions the MC simulation will even better describe the data, so that the selection can be further optimized. Especially the particle identification simulation will be improved. Additionally, the LHC run periods in 2011 and 2012 will provide huge amounts of data.

The data sample also contains the RS $D^{*+} \to D^0\pi_s^+ \to (K^-\pi^+)\pi_s^+$ decays. The fit to the finally selected and ΔM sideband subtracted RS D^0 mass distribution yields 29624 ± 188 signal candidates and 967 ± 81 background candidates. The fitted distribution is shown in figure 5.5.

Fit Parameter	Fitted Value
sig. cand.	141.573 ± 46.373
bkg. cand.	3267.460 ± 74.535
μ [MeV]	145.421 (const.)
σ_1 [MeV]	0.700 ± 0.097
σ_2 [MeV]	3.500 ± 1.298
fraction	0.550 ± 0.429
$\Delta M\|_0$ [MeV]	139.2 (const.)
a	0.247 ± 1.649
b [MeV]	8.350 ± 8.851
c [MeV]	3.763 ± 1.781

Table 5.3.: Parameters of the fit to the ΔM distribution of WS decays in $\mathcal{L} = (0.61 \pm 0.01)\,\mathrm{pb}^{-1}$ of data.

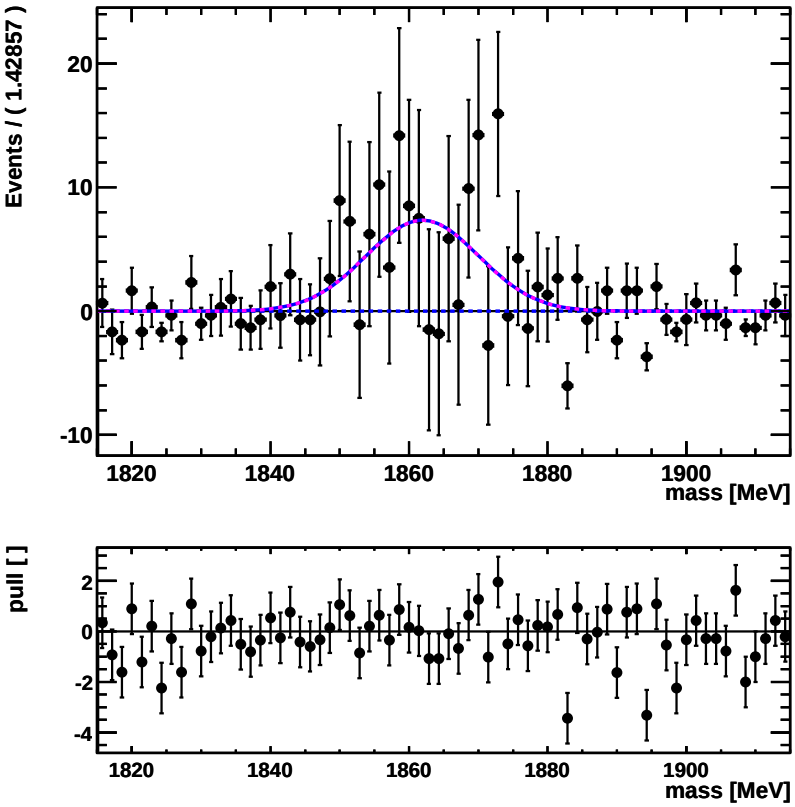

Figure 5.4.: Fit to the ΔM sideband subtracted D^0 mass distribution of WS decays in $\mathcal{L} = (0.61 \pm 0.01)\,\mathrm{pb}^{-1}$ of data.

Fit Parameter	Fitted Value
sig. cand.	113.743 ± 6.720
bkg. cand.	0.333 ± 0.820
μ [MeV]	1861.940 ± 0.197
σ_1 [MeV]	8.139 ± 0.154
slope [MeV]	0.173 ± 0.088

Table 5.4.: Parameters of the fit to the ΔM sideband subtracted D^0 mass distribution of WS decays in $\mathcal{L} = (0.61 \pm 0.01)\,\mathrm{pb}^{-1}$ of data.

All fit parameters are listed in table 5.5. Hence, the ratio of WS to RS decays in LHC*b* data was also measured, see equation 5.6.

$$\frac{\#(\mathrm{WS})}{\#(\mathrm{RS})} = \frac{114 \pm 7}{29624 \pm 188} = (3.85 \pm 0.24) \times 10^{-3} \tag{5.6}$$

This measurement is compatible with the world average measurement [19]: $\mathcal{B}^{(\mathrm{WS})}/\mathcal{B}_{(\mathrm{RS})} = (3.80 \pm 0.19) \times 10^{-3}$ within $1\,\sigma$.

Fit Parameter	Fitted Value
sig. cand.	29624.300 ± 187.917
bkg. cand.	966.823 ± 81.453
μ [MeV]	1862.300 ± 0.058
σ_1 [MeV]	8.244 ± 0.298
σ_2 [MeV]	12.494 ± 0.976
fraction	0.712 ± 0.103
slope [$\times 10^{-3}$ MeV]	6.811 ± 0.126
curvature [$\times 10^{-6}$ MeV^{-1}]	-3.805 ± 0.065

Table 5.5.: Parameters of the fit to the ΔM sideband subtracted D^0 mass distribution of RS decays in $\mathcal{L} = (0.61 \pm 0.01)\,\mathrm{pb}^{-1}$ of data. The background is fitted by a second order polynomial with the fit parameters slope and curvature.

5.4. Stripping 12 Data Set

The presently largest data set, taken by the LHC*b* experiment, is the stripping 12 data set. The recorded integrated luminosity for this stripping 12 data is $\mathcal{L} = (37 \pm 1.5)\,\mathrm{pb}^{-1}$. The WS decay selection was optimized in this thesis on a previous reconstruction version,[4] in which the

[4] The reconstruction version of the data sets to optimize the selection and the reconstruction version of the stripping 07 data set is reco-04. The stripping 12 data set was processed with the reconstruction version reco-06.

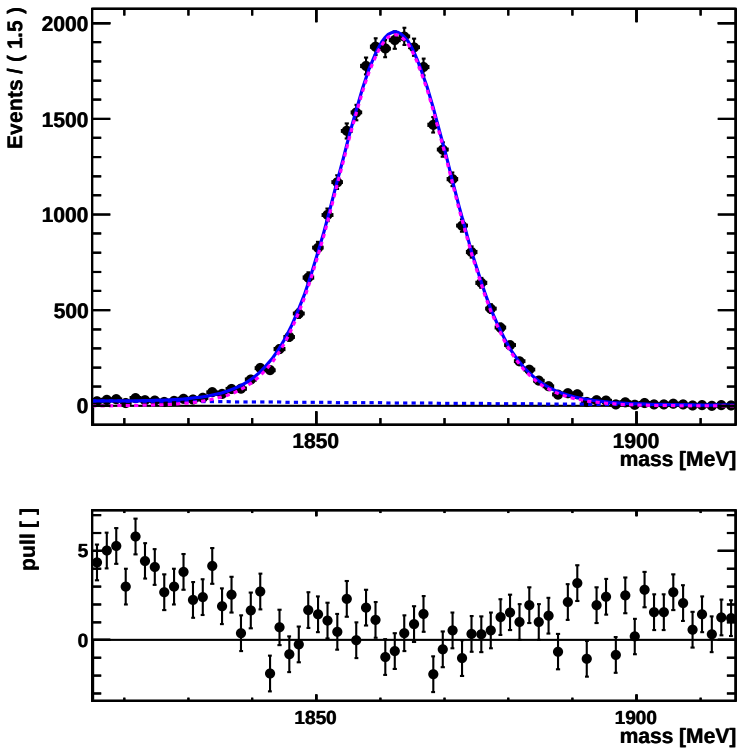

Figure 5.5.: Fit to the ΔM sideband subtracted D^0 mass distribution of RS decays in $\mathcal{L} = (0.61 \pm 0.01)\,\mathrm{pb}^{-1}$ of data. The background is fitted by a second order polynomial.

resolution in data was significantly worse than in MC due to the earlier version of the detector alignment. This difference in the resolution between data and MC becomes smaller with the current reconstruction version. Additionally to the promising potential of this huge data set to filter many signal decays, the sample can be used simultaneously as an independent sample to verify the selection optimization. Around 2000 WS decays are selected. With this amount of WS signal events a mixing analysis is already feasible.

5.4.1. Fit to the ΔM Distribution in Data

The PDF to fit the ΔM distribution was introduced in section 5.1. The Fit to the ΔM distribution of WS decays in stripping 12 data is shown in figure 5.6. The regions to calculate the statistical weight for the sideband subtraction are indicated by the vertical lines in figure 5.6. They are defined with exactly the same limits as in the MC fit, the signal window is set to $[142.5, 148.2]$ MeV and the sidebands are set to $[140.0, 142.0]$ MeV and $[149.0, 159.0]$ MeV. This data sample provides significantly more statistics than the stripping 07 sample. The fit determines 2257 ± 330 signal $D^* \to D^0\pi$ decays and 11813 ± 98 random soft pion background decays. In total 47280 ± 394 background events are determined in this fit. The mean value μ of the Double-Gaussian and the turn on parameter $\Delta M|_0$ of the Argus distribution are fixed, to reduce the number of free fit

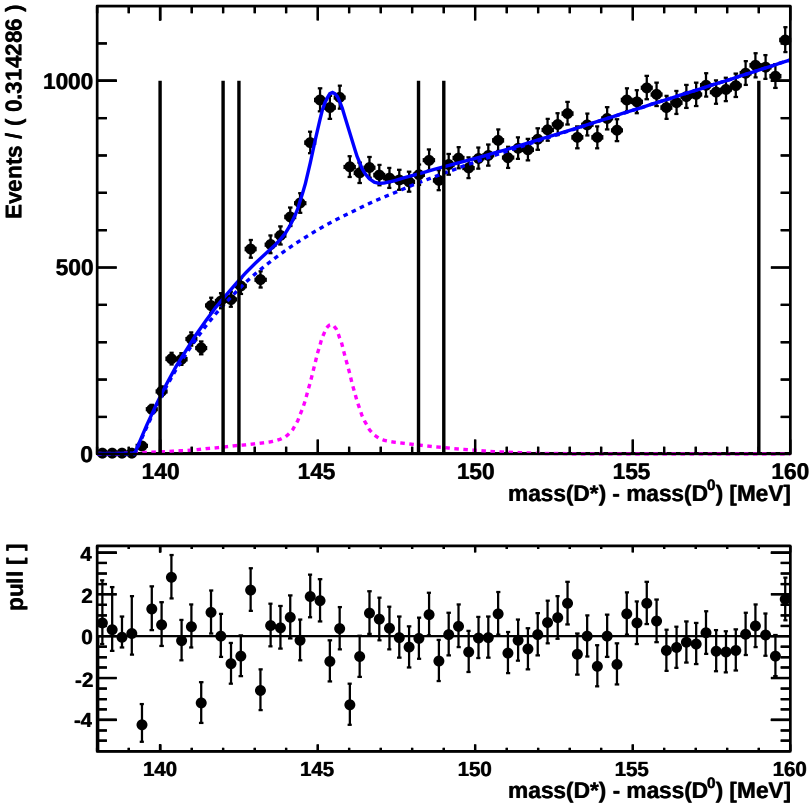

Figure 5.6.: Fit to the ΔM distribution of WS decays in $\mathcal{L} = (37 \pm 1.5)\,\mathrm{pb}^{-1}$ of data. The vertical lines indicate the areas for sideband subtraction. The borders of the signal window are $[142.5, 148.2]\,\mathrm{MeV}$, the first background sideband is defined in $[140.0, 142.0]\,\mathrm{MeV}$ and the second background sideband is defined in $[149.0, 159.0]\,\mathrm{MeV}$.

parameters. As explained above, both parameters are reconstruction independent, because they rely only on the absolute mass difference of the D^* minus the D^0. All fit parameters are listed in table 5.6.

5.4.2. Fit to the D^0 Mass Distribution in Data

The PDF to fit the ΔM sideband subtracted D^0 mass distribution was introduced in section 5.2. The fit to the sideband subtracted D^0 mass distribution of WS decays in $\mathcal{L} = (37 \pm 1.5)\,\mathrm{pb}^{-1}$ of data is shown in figure 5.7. The fit determines 1966 ± 28 WS $D^* \to D^0\pi_s^+ \to (K^+\pi^-)\pi_s^+$ signal decays and 23 ± 0 combinatorial background D^0 decays. The previous fit applied to the ΔM distribution determined 2257 ± 330 signal $D^* \to D^0\pi$ decays. These numbers agree within $1\,\sigma$. All fit parameters are listed in table 5.7.

The amount of Cabibbo favored $D^* \to D^0\pi_s^+ \to (K^-\pi^+)\pi_s^+$ RS decays is again also measured in this data sample. The fit to the finally selected and ΔM sideband subtracted D^0 mass distribution

Fit Parameter	Fitted Value
sig. cand.	2256.960 ± 330.084
bkg. cand.	47280.800 ± 393.852
μ [MeV]	145.421 (const.)
σ_1 [MeV]	0.560 ± 0.059
σ_2 [MeV]	2.725 ± 0.294
fraction	0.606 ± 0.129
$\Delta M\|_0$ [MeV]	139.2 (const.)
a	2.953 ± 0.132
b [MeV]	3.238 ± 0.963
c [MeV]	2.680 ± 0.173

Table 5.6.: Parameters of the fit to the ΔM distribution of WS decays in $\mathcal{L} = (37 \pm 1.5)\,\mathrm{pb}^{-1}$ of data.

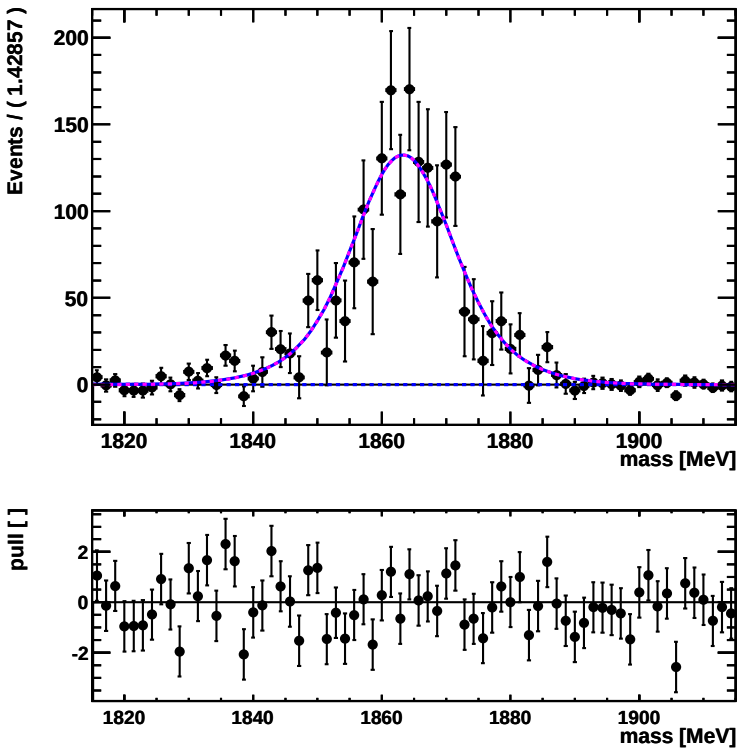

Figure 5.7.: Fit to the ΔM sideband subtracted D^0 mass distribution of WS decays in $\mathcal{L} = (37 \pm 1.5)\,\mathrm{pb}^{-1}$ of data.

Fit Parameter	Fitted Value
sig. cand.	1965.770 ± 27.810
bkg. cand.	22.821 ± 0.316
μ [MeV]	1863.340 ± 0.017
σ_1 [MeV]	6.908 ± 0.001
σ_2 [MeV]	11.918 ± 0.003
fraction	0.536 ± 0.006
slope [$\times 10^{-3}$ MeV]	-0.521 ± 0.000

Table 5.7.: Parameters of the fit to the ΔM sideband subtracted D^0 mass distribution of WS decays in $\mathcal{L} = (37 \pm 1.5)\,\mathrm{pb}^{-1}$ of data.

of RS decays in $\mathcal{L} = (37 \pm 1.5)\,\mathrm{pb}^{-1}$ of data is shown in figure 5.8. It determines 401610 ± 660 RS signal events and 10208 ± 210 combinatorial background events. All fit parameters are listed in table 5.8. The ratio of WS to RS decays in $\mathcal{L} = (37 \pm 1.5)\,\mathrm{pb}^{-1}$ of LHCb data is measured, see

Fit Parameter	Fitted Value
sig. cand.	401610.000 ± 659.996
bkg. cand.	10208.300 ± 210.404
μ [MeV]	1864.110 ± 0.014
σ_1 [MeV]	6.392 ± 0.105
σ_2 [MeV]	9.840 ± 0.085
fraction	0.387 ± 0.025
slope	0.897 ± 0.002
curvature [$\times 10^{-6}$ MeV]	-463.838 ± 0.865

Table 5.8.: Parameters of the fit to the ΔM sideband subtracted D^0 mass distribution of RS decays in $\mathcal{L} = (37 \pm 1.5)\,\mathrm{pb}^{-1}$ of data. The background is fitted by a second order polynomial with the fit parameters slope and curvature.

equation 5.7.

$$\frac{\#(\mathrm{WS})}{\#(\mathrm{RS})} = \frac{1966 \pm 28}{401610 \pm 660} = (4.89 \pm 0.07) \times 10^{-3} \tag{5.7}$$

This measurement is $5.7\,\sigma$ above the world average measurement [19]: ${}^{\mathcal{B}(\mathrm{WS})}/_{\mathcal{B}(\mathrm{RS})} = (3.80 \pm 0.19) \times 10^{-3}$ and above the first measurement in $\mathcal{L} = (0.61 \pm 0.01)\,\mathrm{pb}^{-1}$ of data performed in section 5.3.2: ${}^{\mathcal{B}(\mathrm{WS})}/_{\mathcal{B}(\mathrm{RS})} = (3.85 \pm 0.24) \times 10^{-3}$. This deviation was not expected. The MC prediction, that 10 % double misidentified RS decays are still within the WS signal decays, shown in section 4.5, can not explain this deviation of about 29 %. There are three possibilities, why this deviation occurs here. First, the estimate on the number of WS signal decays is too high. A reasonable explanation could be the following. Due to the significantly lower statistics of the data

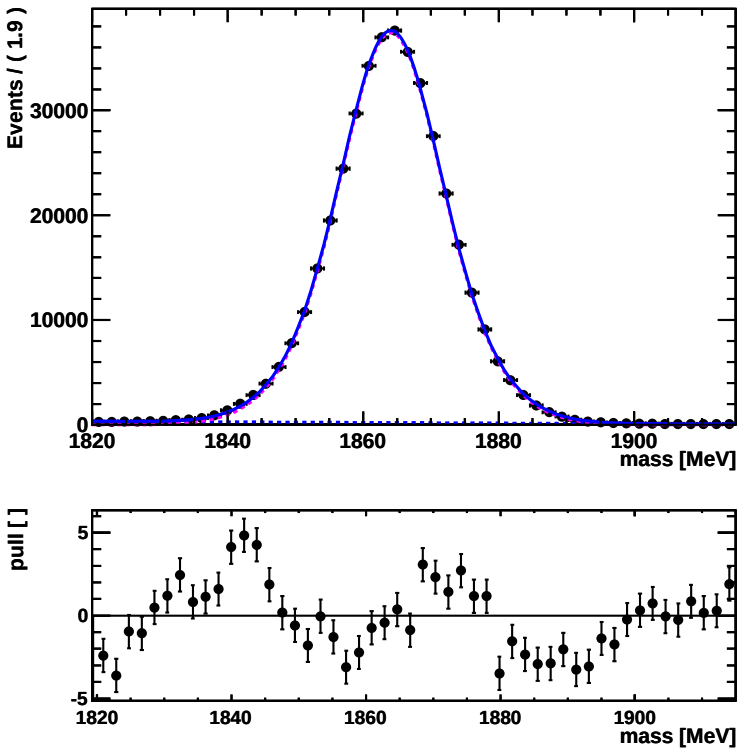

Figure 5.8.: Fit to the ΔM sideband subtracted D^0 mass distribution of RS decays in $\mathcal{L} = (37 \pm 1.5)\,\mathrm{pb}^{-1}$ of data. The background is fitted by a second order polynomial.

and MC samples the selection was optimized with, the development of the physics background suppression reached its statistical limitations. Now, in this huge data set physics background contributions occur that have not been tested on MC sufficiently. Hence, the estimate on the number of WS decays in stripping 12 data would be too high, because they could still contain fake WS decays. Up to now, there was no bigger MC sample available. Second, the estimate on the number of RS decays is too low. In principle, the kinematics of RS and WS decays should be the same. Hence, also the reconstruction efficiency should be the same for RS and WS decays, but then it would not be possible that proportionally less RS events are measured than WS events. Third, the world average value is simply not quite correct. However, before this statement can be made this WS to RS ratio measurement needs to be investigated further with the help of a larger MC sample.

Nevertheless, the estimate on the number of WS decays in the $37\,\mathrm{pb}^{-1}$ of LHCb data is within the correct order of magnitude. Once the reason for the deviation of the measured WS to RS ratio from the world average value is found, with an amount of $\mathcal{O}(10^3)$ WS signal events a mixing analysis will already be feasible.

6. D^0 Lifetime Measurement

In this chapter a method is presented to measure the D^0 lifetime in early LHC*b* data. The decay probability of unstable particles like D^0 mesons is constant. This leads to an exponential proper time distribution with a mean lifetime, while every single particle decays after its individual proper time.

The fully hadronic decay channel $D^* \rightarrow D^0(K^-\pi^+)\pi_s$ is used to measure the D^0 lifetime. In hadronic decays it is a very common and effective method to distinguish signal events from background by cutting on the minimal impact parameter (IP) of final track states. The impact parameter is the shortest distance between an extrapolated track and the primary vertex, see figure 6.1.

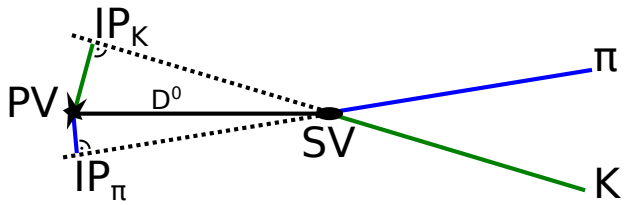

Figure 6.1.: Schematic of the impact parameters (IP) of the D^0 daughters, K and π. The D^0 is produced at the primary vertex (PV) and decays at the secondary vertex (SV). The tracks of K and π are extrapolated backwards. The minimal distance between such a track extrapolation and the primary vertex is called impact parameter.

D^0 mesons have a lifetime of 0.4 ps. Hence, the average IP of the tracks of their decay daughters is significantly non-zero. A minimum requirement on the value of the IP (significance) strongly suppresses promptly decaying background, which is the main background for a fully hadronic decay. These IP cuts are used by the high level trigger. However, a minimum IP cut also rejects true signal events, decaying at short proper times. Hence, cutting on a displacement variable, requiring a minimum distance to the primary vertex, results in distorting the reconstructed proper time distribution of the D^0.

The LHC*b* signal data used in this thesis is first triggered and then stripped by a relatively loose signal selection, that applies exactly the above described displacement cuts. This setup necessitates an acceptance function, which provides information about how many D^0s in what proper time region have a chance to be detected, triggered and stripped and especially how many D^0s cannot be reconstructed. Hence, the acceptance function provides information as a function of the proper time about the particular distortion of the proper time distribution. For this thesis the approach was made, to take the acceptance function from the MC simulation.

There are also possibilities to avoid such lifetime biases. For example in leptonic or semi-leptonic decays a sufficient signal purity can be reached without applying impact parameter cuts,

that are distorting the proper time distribution, but applying particle identification cuts. For fully hadronic decays in the LHC*b* experiment, the only source of particle identification are the two RICH detectors. However, their reconstruction is too time consuming, that makes the particle identification unavailable at trigger level. Hence, using hadronic decays to measure the lifetime suffers from distorted proper time distributions.

An alternative ansatz to correct for the lifetime bias in hadronic decays can be made by taking an event by event acceptance function, determined in data [11]. The basic assumption of this approach is, that the efficiency for detecting and reconstructing an event is independent of the proper time. Hence, the event by event acceptance function becomes a step function and the position of the step is determined by the IP cut. For every D decay this step is determined by varying the position of the primary vertex similar to nested intervals. Thus the method is also called "swimming" method. Some more comments on this method are given in the appendix A.

Within the lifetime measurement performed in this thesis two main issues have to be addressed. First, due to the proper time distribution sculpting IP cuts a proper time acceptance function is derived on Monte Carlo after performing careful data-Monte Carlo comparisons. A track parameter smearing method is developed to compensate for the worse resolution in data due to not yet final alignment and calibration of the LHC*b* detector. Second, due to a significant fraction of D^0 candidates $(5-10\%)$ produced in B decays, the proper time distribution contains a contribution from the B lifetime. This fraction of D from B decays is studied by fitting the logarithmic D^0 impact parameter distribution. Additionally, the associated systematics on the lifetime due to uncertainties in the data-Monte Carlo agreement are determined. Finally the lifetime fit is performed on a data set corresponding to $0.6\,\mathrm{pb}^{-1}$ of early 2010 LHC*b* data.

6.1. Selection

To measure the D^0 lifetime the Cabibbo favored decay channel $D^0 \to K^-\pi^+$ is sufficient. A tagging D^* and slow pion is not necessary. However, the quantity $\Delta M = m(D^*) - m(D^0)$ is a very powerful cut to suppress a lot of combinatorial background. Hence, the previously optimized selection for the $D^* \to D^0(K^+\pi^-)\pi_s^+$ 'Wrong Sign' (WS) decays is resumed and relaxed for the $D^* \to D^0(K^-\pi^+)\pi_s^+$ 'Right Sign' (RS) decays, because due to the branching fractions RS decays are much more likely to reconstruct the right way in terms of tagging and double misidentification than WS decays. The previously used ΔM sideband subtraction to select correctly tagged WS decays, is changed into a simple ΔM cut to suppress the combinatorial background of the D^* decays. Another advantage of taking the same decay channel is, that the same stripping line can be used. The simulation part of the lifetime study is performed on the same Monte Carlo sample, that was used in the WS selection study (see chapter 4), according to an integrated luminosity of $\mathcal{L} = 193.49\,\mathrm{nb}^{-1}$.[1] The lifetime measurement is preformed on magnet down data out of the stripping 07 processing, corresponding to an integrated luminosity of $\mathcal{L} = (0.606 \pm 0.01)pb^{-1}$.[2] The stripping cuts are listed in table 6.1. They are slightly tightened and complemented to achieve a good signal to background ratio and to achieve MC data agreement in all lifetime

[1] MC, 2010, Beam3500GeV-VeloClosed-MagDown-Nu1, 2010-Sim03Reco03-withTruth, $Dst\_D0pi, hh = DecProdCut$. LHC*b* event type number: 27363001, Gauss v38r4.

[2] Stripping 07: StrippingDstarPromptWithD02HH.py

relevant quantities. The additional final selection cuts, which are also listed in table 6.1, will be motivated, when the data-Monte Carlo comparisons are made in section 6.7.

Particle	Cut Variable	Stripping	Final Selection
hh	p	> 5000 MeV	> 5000 MeV
hh	p_T	> 500 MeV	> 500 MeV
hh	Track $\chi^2/ndof$	< 10	< 5
hh	Ip χ^2	> 4	> 4
hh	Ip		> 0.060 mm
hh	Ip error		< 0.030 mm
hh	# VELO hits		> 11
D^0	p_T	> 1000 MeV	> 2000 MeV
D^0	Vertex $\chi^2/ndof$	< 10	< 10
D^0	PV displacement χ^2	> 16	> 16
D^0	flight distance		> 3.2 mm
D^0	flight distance error		< 0.8 mm
D^0	dira	> 0.99993	> 0.99993
π_s	p_T	> 110 MeV	> 110 MeV
D^*	p_T	> 2200 MeV	> 2200 MeV
D^*	Vertex $\chi^2/ndof$	< 13	< 12
D^*, D^0	ΔM		[142.0, 149.0] MeV
event	# primary vertices		< 2

Table 6.1.: Selection to filter $D^{*+} \to D^0\pi_s^+ \to (K^-\pi^+)\pi^+$ RS decays, which are used to measure the D^0 lifetime. The cut values of the used by the stripping preselection and the ones used by the final selection are given.

To demonstrate the content of signal decays of this data set the D^0 mass distribution in data is fitted by a Double-Gaussian distribution for signal and a second order polynomial distribution for background, see figure 6.2. The fit determines 24572 ± 201 signal candidates and 3158 ± 138 combinatorial background candidates. The background contribution is removed through D^0 mass sideband subtraction. All fitted parameters are listed in table 6.2.

6.2. Lifetime Fit Principle

D^0 mesons decay with a constant decay probability. Every single D^0 has its own certain proper time, when it decays, but on average half of the total number of D^0s is decayed after the mean D^0 lifetime. This statistical process is described by the following differential equation 6.1.

$$\frac{dN}{dt} = -\lambda N\,. \tag{6.1}$$

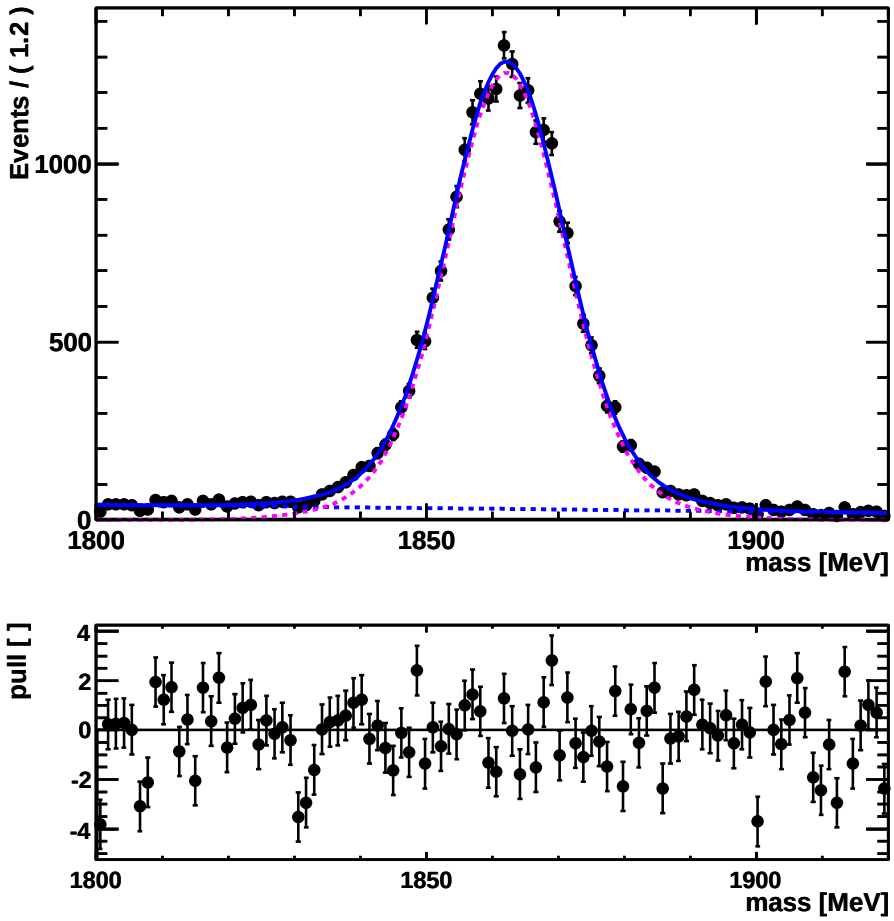

Figure 6.2.: Fit to the D^0 mass distribution of selected $D^{*+} \to D^0\pi_s^+ \to (K^-\pi^+)\pi^+$ RS decays in data.

Fit Parameter	Signal Data
# signal cand.	24600.000 ± 201.000
# bkg. cand.	3160.000 ± 138.000
Mean μ [ps]	1860.000 ± 0.068
σ_1 [ps]	8.460 ± 0.254
σ_2 [ps]	14.900 ± 1.610
Fraction f [%]	0.777 ± 0.068
slope [$\times 10^{-3}$]	1.820 ± 0.176
curvature [$\times 10^{-6}$]	−1.150 ± 0.087

Table 6.2.: Parameters of the fit to the D^0 mass distribution in Data.

The symbol λ denotes the decay constant. The solution of equation 6.2 is the exponential decay law, equation 6.2:

$$N(t) = N_0 \cdot e^{-\lambda t} \,. \tag{6.2}$$

The reciprocal value of λ is the lifetime τ. The lifetime τ is the quantity, that will be measured for D^0s by fitting their proper time distribution, see equation 6.3.

$$PDF(t;\tau_{fit}) = \frac{1}{\tau_{fit}} \cdot e^{-\frac{t}{\tau_{fit}}} \,, \tag{6.3}$$

where t denotes the reconstructed proper time. Measuring the proper time distribution means looking with a certain detector resolution at this quantity. This resolution is convolved into the proper time distribution. The proper time resolution is measured in MC by subtracting the MC truth proper time from the reconstructed MC proper time. It can be described by a Double-Gaussian distribution. The probability density function (PDF) to fit the proper time distribution is then, equation 6.4:

$$PDF(t;\tau_{fit}) = \frac{1}{\tau_{fit}} e^{-\frac{t}{\tau_{fit}}} \otimes DG(t;\mu,\sigma_1,\sigma_2,f) \,. \tag{6.4}$$

Additionally trigger and selection efficiencies have to be considered. To select signal D^0 candidates there are several cuts made by the trigger and the final selection concerning the displacement of the D^0 decay vertex with respect to the primary vertex, e.g. impact parameter cuts on the D^0 daughters and flight distance cuts on the D^0 directly. The total number of reconstructed and accepted D^0s with small proper times is therefore smaller than the one for D^0s with large proper times. To consider this effect an acceptance function is defined, equation 6.5:

$$\epsilon(t) = \frac{t\,\text{distribution of MC candidates passing the selection}}{e^{-\frac{t}{\tau_{true}}} \otimes DG(t;\mu,\sigma_1,\sigma_2,f)} \,, \tag{6.5}$$

with

$$\tau_{true} = (410.1 \pm 1.5)\,\text{fs} \,. \tag{6.6}$$

The above quoted true D^0 lifetime value is the world average of all measurements and is taken from [19]. The acceptance function is calculated on MC. To adapt the fit model on the measurement, the full trigger and selection configuration has to be simulated on MC. The PDF to fit the measured D^0 proper time distribution in data is finally given by equation 6.7:

$$PDF(t;\tau_{fit}) = \epsilon(t) \cdot \left(e^{-\frac{t}{\tau_{fit}}} \otimes DG(t;\mu,\sigma_1,\sigma_2,f) \right) \tag{6.7}$$

6.3. Complete Lifetime PDF

Combinatorial background is removed from the D^0 proper time distribution by D^0 mass sideband subtraction. Thus, the entire PDF to fit the D^0 proper time distribution in data consists only of a signal part, PDF_{prompt}, and a part to fit physical background, PDF_{second}, see equation 6.8.

$$PDF_{fit}(t;\tau_{fit},f) = (1-f)\cdot PDF_{prompt}(t;\tau_{fit}) + f\cdot PDF_{second}(t) \tag{6.8}$$

PDF_{prompt} fits the D^0 lifetime of true signal candidates, D^0s coming from prompt D^*s, that are directly coming from the primary vertex. The second term, PDF_{second}, has to be added, because additionally to the true signal candidates D^0s originating from B decays lie within the signal region. This is non prompt signal and is therefore called secondary D^0s. The fraction f, separating the prompt and the secondaries PDFs, has to be extracted from another fit, described in section 6.8.

6.4. Track Resolution Smearing

To assure data-Monte Carlo comparability, identical reconstruction versions for the MC simulation and real data are taken.[3] The detector was not yet fully aligned and calibrated, which is visible in the track resolution. The resolution in data is significantly worse than in MC. This is a well known problem among the collaboration. The VELO group releases official plots concerning this problem. See figure 6.3.

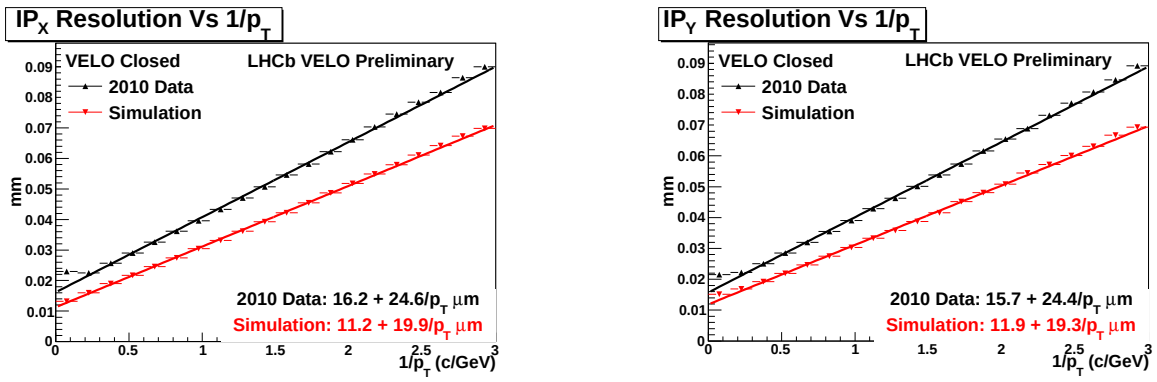

(a) IP_x (b) IP_y

Figure 6.3.: Official VELO plots: IP resolution versus the inverse transverse momentum of the current MC and data reconstruction versions.

For this lifetime fit method, taking the lifetime acceptance function and the proper time resolution from MC, it is necessary to have the track resolution correctly simulated in MC. So the above mentioned MC reconstruction version will be smeared in the track resolution for this analysis.

6.4.1. Smearing Idea

The basic assumption for this smearing method is, that the track resolution is primarily dependent on the transverse momentum. LHC*b* tracks are parameterized in the z coordinate, because of the

[3] MC: simulation 03, reconstruction 04; Magnet Down Data: from the May and June data taking, reconstruction 04, stripping 07.

geometry of B events studied. Hence, resolution corrections in the perpendicular directions, x and y, are propagated equally into the track description. Taking the transverse momentum to parameterize the track resolution guarantees, that the full phase space, determining the resolution, is covered.

To determine the track resolution the impact parameter projections on the x and y axis, IP_x and IP_y, of prompt pions are studied. Therefore, minimum bias samples for data and for MC are taken. The minimum bias data sample was recorded in April 2010[4]. It contains events with at least one proton proton interaction and corresponds to an integrated luminosity of $\sim 400\,\mu\text{b}^{-1}$. The MC minimum bias sample corresponds to an integrated luminosity of $\sim 170\,\mu\text{b}^{-1}$.[5] These samples are triggered by the one track trigger to exclude beam gas events. Pions originating directly from the primary vertex actually have a zero impact parameter. Hence, the IP_x and IP_y distributions of prompt pions represent the track resolution.

The IP projections are fitted by single Gaussian distributions in bins of $1/p_T$. Then the widths of all fitted Gaussians are plotted against $1/p_T$. The track resolution in data is worse, so the data track resolution distribution lies above the MC distribution. To adapt the MC resolution to the data every single MC track has to be smeared by the missing resolution difference. The smearing parameters are determined on the minimum bias samples and then applied to the signal MC tracks, propagating into all reconstructed signal D^0 quantities.

6.4.2. Smearing Technique

The minimum bias track resolution distributions for data and MC are fitted by straight lines, see equation 6.9:

$$f_{x,y}(1/p_T) = a_{x,y} + b_{x,y}/p_T\,. \tag{6.9}$$

The fitted IP_x and IP_y distributions of data and MC are shown in figure 6.4. The fits show, that in data the track resolution curves are more flat than in MC, the fitted values for b are smaller, but the curves start on a higher level, the fitted values for a are bigger. All fitted parameters are listed in table 6.3. Technically the smearing is applied to MC by taking the first track state and

curve	a $[\mu m]$	b $[\mu m\,GeV]$
MC IP_x	18.31 ± 0.42	42.96 ± 0.55
MC IP_y	19.46 ± 0.42	41.80 ± 0.55
data IP_x	52.77 ± 0.75	35.27 ± 1.01
data IP_y	51.92 ± 0.75	34.74 ± 1.00

Table 6.3.: Minimum Bias Data and MC: Track Resolution Fit for Smearing $f(1/p_T) = a + b/p_T$, with p_T in GeV.

adding up Gaussian random numbers to compensate the difference. The widths $\Delta(\sigma)_{x,y}$ to draw

[4] LHC*b* run numbers: 69353 – 71807.
[5] MC, 2010-Sim03Reco03-withTruth, minimum bias, 10699961 events.

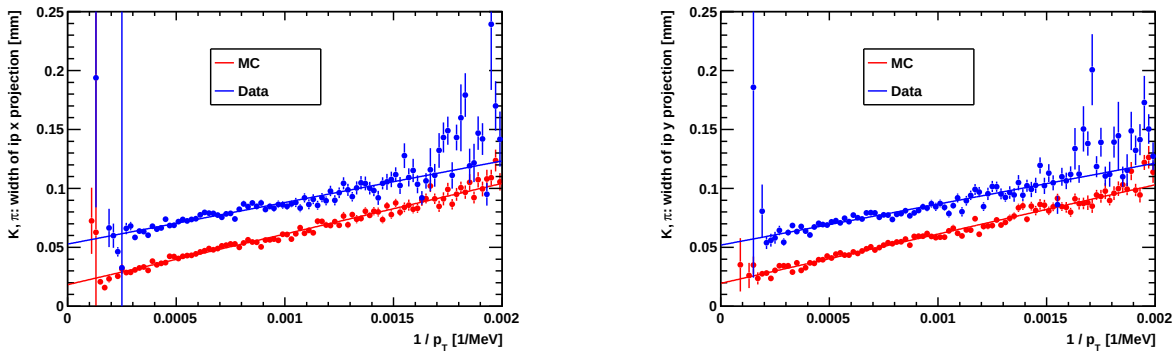

(a) IP_x (b) IP_y

Figure 6.4.: Minimum bias MC and data: The track resolution distributions are fitted. The Gaussian widths of the IP_x and IP_y projections of pion tracks coming from the primary vertex are plotted against the inverse transverse momentum of these tracks.

the Gaussian random numbers for the x and y direction separately are determined in the above shown straight line fits, following equation 6.10.

$$\Delta(\sigma)_{x,y} = \sqrt{IP^2_{x,y}(data) - IP^2_{x,y}(MC)} \tag{6.10}$$

To find the final value to add up on the spacial track coordinates a Gaussian random number is drawn with $\Delta(\sigma)_x$ and $\Delta(\sigma)_y$, see equation 6.11.

$$(x, y)_{rand} = \text{Gauss}(\Delta(\sigma)_{x,y}) / \cos^2(tx, ty) \tag{6.11}$$

The $\cos^2$ term is a small correction to the track slope tx and ty. Finally x_{rand} and y_{rand} are just added up on the original MC track states x and y:

$$state[0] \rightarrow setX(x + x_{rand})\,, \tag{6.12}$$

$$state[0] \rightarrow setY(y + y_{rand})\,. \tag{6.13}$$

The final smearing adjustment is shown in figure 6.5. The MC resolution was not only shifted to higher values, but also corrected in the slope. Especially tracks with a transverse momentum range between 500 and 1500 MeV are important for the D^0 signal candidate reconstruction later on, this corresponds to an inverse transverse momentum range between 0.002 and 0.0007 $\frac{1}{MeV}$.

These smearing parameters are then applied to the signal MC. The track state modification happens in the beginning of the reconstruction chain in DaVinci before the D^0 particles are reconstructed. So once the track positions are smeared all other reconstructed quantities like the proper time resolution and the lifetime, the flight distance and the impact parameter in total are effected. Figure 6.6 and figure 6.7 show the IP resolution distributions before and after the smearing for selected D^0 signal candidates in MC.

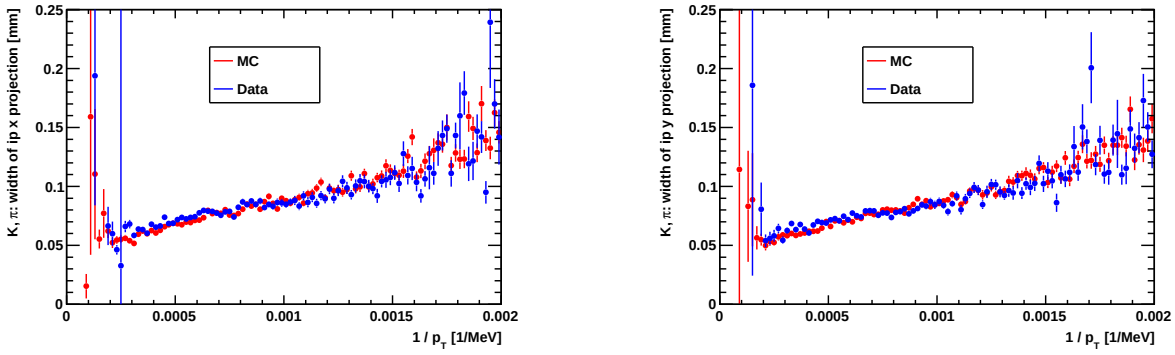

(a) IP_x (b) IP_y

Figure 6.5.: Minimum bias smeared MC and data: track resolution fits. The Gaussian widths of the IP x and y projections of pion tracks coming from the primary vertex are plotted against the inverse transverse momentum of these tracks.

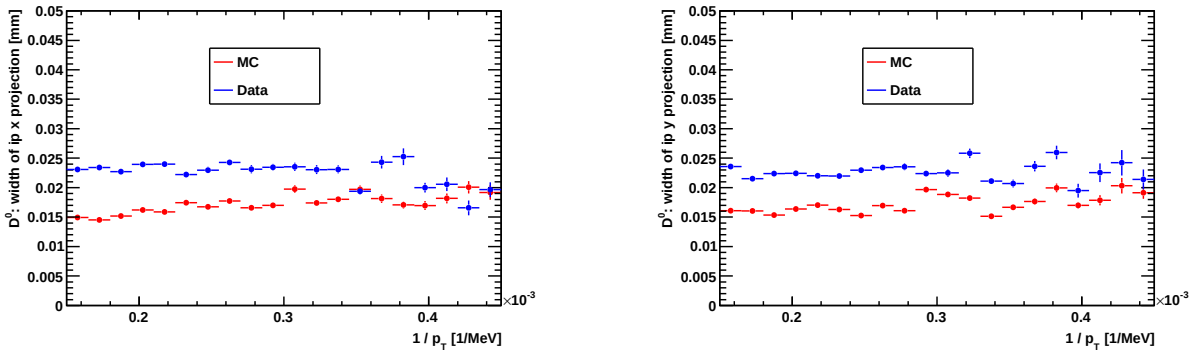

(a) IP_x (b) IP_y

Figure 6.6.: D^0 impact parameter resolution of the original signal MC against signal data, D^0 mass sideband subtracted.

To quantify the MC track resolution smearing impact, the IP_x and IP_y distributions are fitted in signal data (see figure 6.8), in the original signal MC (see figure 6.9) and in the smeared signal MC (see figure 6.10). The fitted PDF is a Double-Gaussian distribution. To better compare the widths an average width $\bar{\sigma}$ is calculated for each Double-Gaussian fit. In data the IP_x average width is fitted with $(1.99 \cdot 10^{-2} \pm 1.54 \cdot 10^{-4})$ mm and the IP_y width is fitted with $(2.05 \cdot 10^{-2} \pm 1.59 \cdot 10^{-4})$ mm. In the original MC the IP_x average width is fitted with $(1.50 \cdot 10^{-2} \pm 2.85 \cdot 10^{-4})$ mm and the IP_y width is fitted with $(1.53 \cdot 10^{-2} \pm 2.95 \cdot 10^{-4})$ mm. While after the track smearing the IP_x average width is fitted in MC with $(2.27 \cdot 10^{-2} \pm 7.24 \cdot 10^{-4})$ mm and the IP_y width with $(2.08 \cdot 10^{-2} \pm 3.84 \cdot 10^{-4})$ mm. The full set of fit parameters is given in table 6.4 for the IP_x

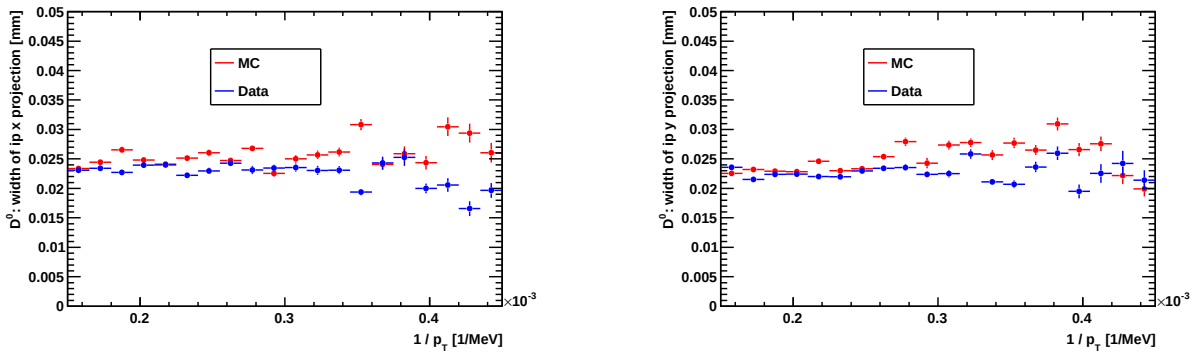

(a) IP_x (b) IP_y

Figure 6.7.: D^0 impact parameter resolution of the smeared signal MC against signal data, D^0 mass sideband subtracted.

fits and in table 6.5 for the IP_y fits. After the MC smearing the track resolution is in agreement between data and MC except for the shift of the mean value of the IP_x distribution in data.

Fit Parameter	Original MC	Smeared MC	Data
Fraction f	0.134 ± 0.005	0.080 ± 0.008	0.111 ± 0.014
Mean μ [µm]	0.063 ± 0.101	0.223 ± 0.174	-7.050 ± 0.157
σ_1 [µm]	58.600 ± 1.680	100.000 ± 15.900	48.200 ± 2.280
σ_2 [µm]	14.700 ± 0.106	23.100 ± 0.202	21.600 ± 0.224
$\bar{\sigma}$ [µm]	15.000 ± 0.285	22.700 ± 0.724	19.900 ± 0.154

Table 6.4.: IP_x Fit Results: Original MC, Smeared MC and Data.

The mean value of the IP_x distribution for signal D^0s in data is shifted, see table 6.4. This is most likely an effect of the beam crossing angle in x direction. Actually this effect should be corrected in the reconstruction process, but since the detector is not optimally aligned yet, it is still present.

To evaluate the impact of the smear parameter determination accuracy two additional MC samples were produced, that are 10% more and 10% less smeared compared to the optimal smearing. These samples are shown with the help of the D^0 logarithmic impact parameter distribution for the three cases: the optimal smearing, the 10% more smearing and the 10% less smearing, see figure 6.11, figure 6.12 and figure 6.13. Figure 6.11 shows data-MC agreement. In figure 6.12 the MC distribution is shifted to larger $\log(IP)$ values with respect to the data distribution, because the track smearing was overdone in MC. A shift of the whole IP distribution occurs and not just a broader IP distribution, because the absolute IP is the spacial integral over its three components in x, y and z direction. In figure 6.13 the MC distribution is shifted to smaller $\log(IP)$ values

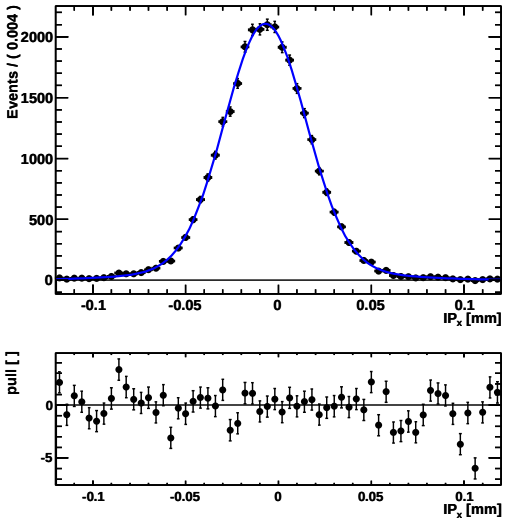

(a) Signal Data: D^0 IP_x

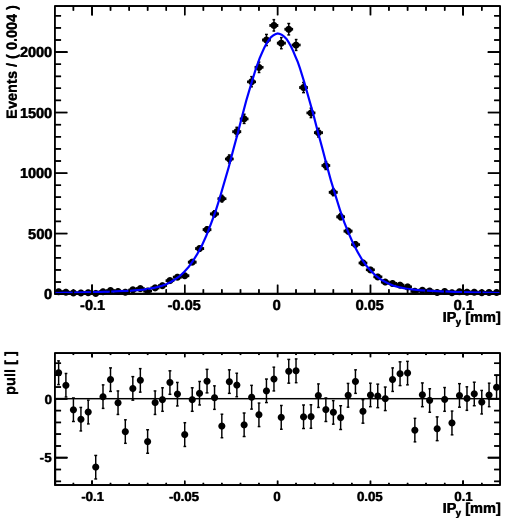

(b) Signal Data: D^0 IP_y

Figure 6.8.: Signal Data: D^0 impact parameter projections on the x-axis (a) and on the y-axis (b). The distribution is D^0 mass sideband subtracted.

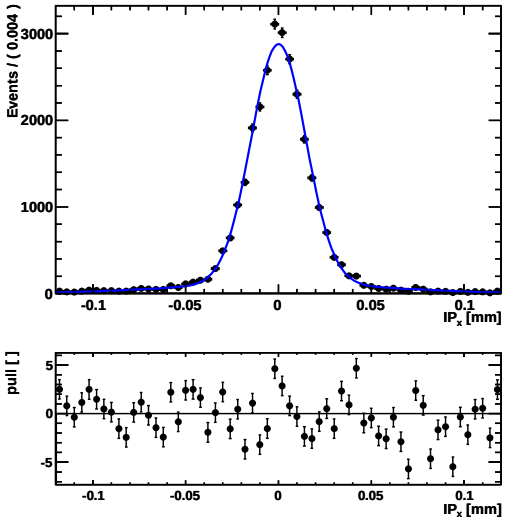

(a) Original Signal MC: D^0 IP_x

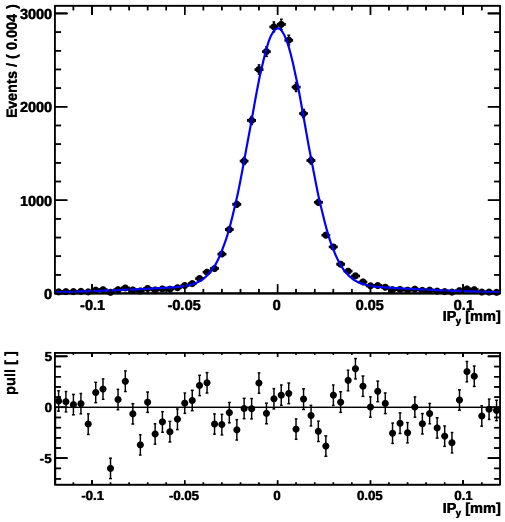

(b) Original Signal MC: D^0 IP_y

Figure 6.9.: Original Signal MC: D^0 impact parameter projections on the x-axis (a) and on the y-axis (b).

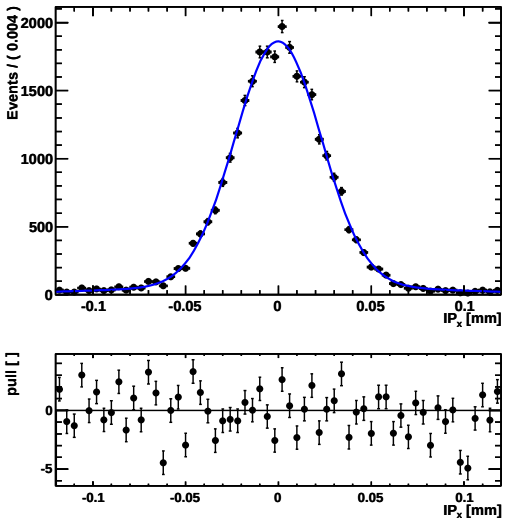

(a) Smeared Signal MC: D^0 IP_x

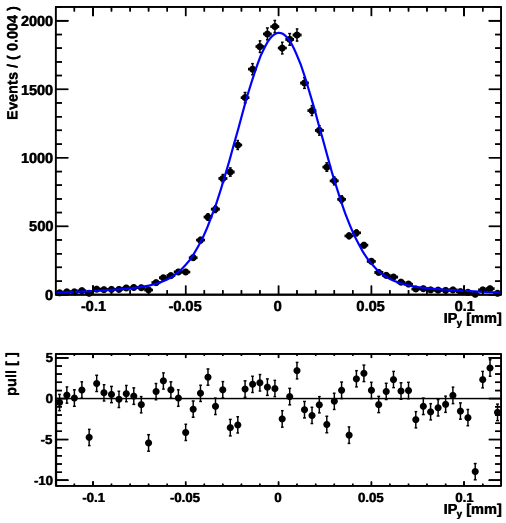

(b) Smeared Signal MC: D^0 IP_y

Figure 6.10.: Smeared Signal MC: D^0 impact parameter projections on the x-axis (a) and on the y-axis (b).

Fit Parameter	Original MC	Smeared MC	Data
Fraction f	0.123 ± 0.005	0.122 ± 0.011	0.072 ± 0.009
Mean μ [µm]	0.151 ± 0.102	0.205 ± 0.171	0.223 ± 0.153
σ_1 [µm]	62.500 ± 2.080	62.400 ± 3.790	59.500 ± 4.340
σ_2 [µm]	15.100 ± 0.107	22.100 ± 0.234	21.600 ± 0.191
$\bar{\sigma}$ [µm]	15.300 ± 0.295	20.800 ± 0.384	20.500 ± 0.159

Table 6.5.: IP_y Fit Results: Original MC and Smeared MC and Data.

with respect to the data distribution, because the track smearing was understated MC. These limits cover the smearing parameter determination accuracy.

6.5. Proper Time Resolution

The above described smearing method was introduced to achieve agreement in the proper time resolution distributions between minimum bias data and minimum bias MC. Due to the displacement cuts of the trigger and the stripping processing on data the proper time resolution is not measurable in signal data. It is measurable in minimum bias data and in minimum bias MC in form of the proper time distribution of fake D^0 decays, that actually have no lifetime. In signal MC the proper time resolution can be determined with the help of MC truth information. The assumption is, that when we are able to simulate the proper time resolution in the smeared

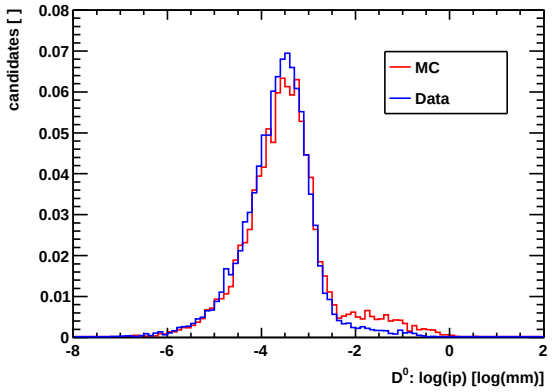

Figure 6.11.: D^0: logarithmic impact parameter distribution. The MC sample is produced with the optimal smearing parameters.

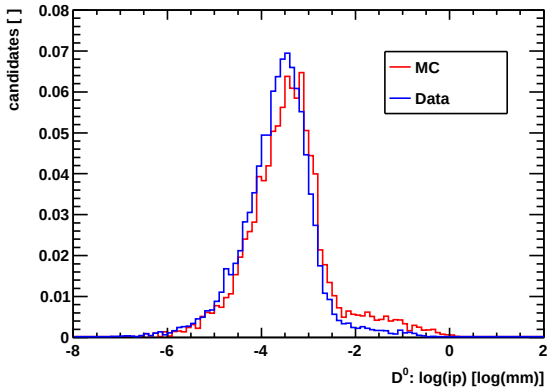

Figure 6.12.: D^0: logarithmic impact parameter distribution. The MC sample is produced with the 10% greater smearing parameters.

minimum bias MC correctly, the smeared signal MC will describe the proper time resolution in signal data. The final signal selection was loosened to select fake D^0 candidates, both selections are listed in table 6.6.

To clarify that the proper time resolution is really measured in data from fake D^0 candidates, that are combinatorial combinations of primary vertex originating tracks, the "mass" distribution of these fake D^0s is shown for minimum bias data and MC in figure 6.14. Consequently, in figure 6.14 is not any mass peak visible, because almost all candidates are background candidates. Figure 6.15 shows the momentum spectra for (a) fake D^0 candidates in minimum bias data and MC and (b) for signal D^0 candidates in signal data and MC. Fake D^0s and signal D^0s do not cover exactly the same phase space, because the momentum spectra for signal D^0s are higher. Hence, the proper time resolution is not exactly the same for fake D^0s and signal D^0s.

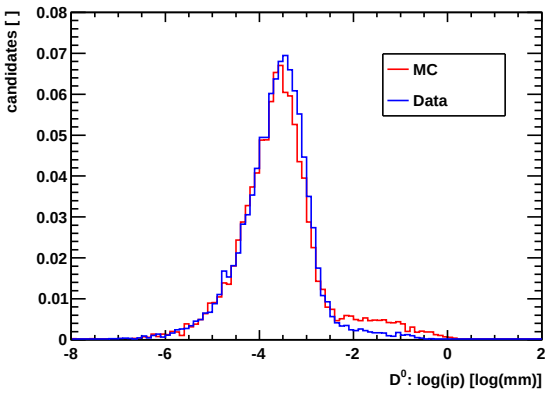

Figure 6.13.: D^0: logarithmic impact parameter distribution. The MC sample is produced with the 10% smaller smearing parameters.

Particle	Cut Variable	Final Signal D^0 Selection	Loose Fake D^0 Selection
hh	p	$>$ 5000 MeV	$>$ 5000 MeV
hh	p_T	$>$ 500 MeV	$>$ 500 MeV
hh	Track $\frac{\chi^2}{ndof}$	$<$ 5	$<$ 5
hh	Ip χ^2	$>$ 4	
hh	Ip	$>$ 0.060 mm	
hh	Ip error	$<$ 0.030 mm	
hh	# VELO hits	$>$ 11	
D^0	p_T	$>$ 2000 MeV	$>$ 1000 MeV
D^0	Vertex $\frac{\chi^2}{ndof}$	$<$ 10	$<$ 10
D^0	PV disp χ^2	$>$ 16	
D^0	flight distance	$>$ 3.2 mm	
D^0	flight distance error	$<$ 0.8 mm	
D^0	dira	$>$ 0.99993	
π_s	p_T	$>$ 110 MeV	$>$ 110 MeV
D^*	p_T	$>$ 2200 MeV	$>$ 2200 MeV
D^*	Vertex $\frac{\chi^2}{ndof}$	$<$ 12	$<$ 13
D^*, D^0	ΔM	$<$ [142.0, 149.0] MeV	
event	# primary vertices	$<$ 2	

Table 6.6.: $D^* \to D^0(hh)\pi_s$ fake signal selection. The cut values of the final signal selection and of the loosened fake D^0 selection are given.

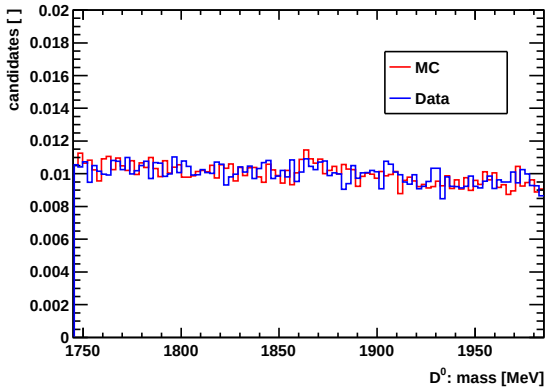

Figure 6.14.: Fake D^0's mass, minimum bias data and minimum bias MC. No D^0 mass peak is visible, because almost all candidates are background candidates.

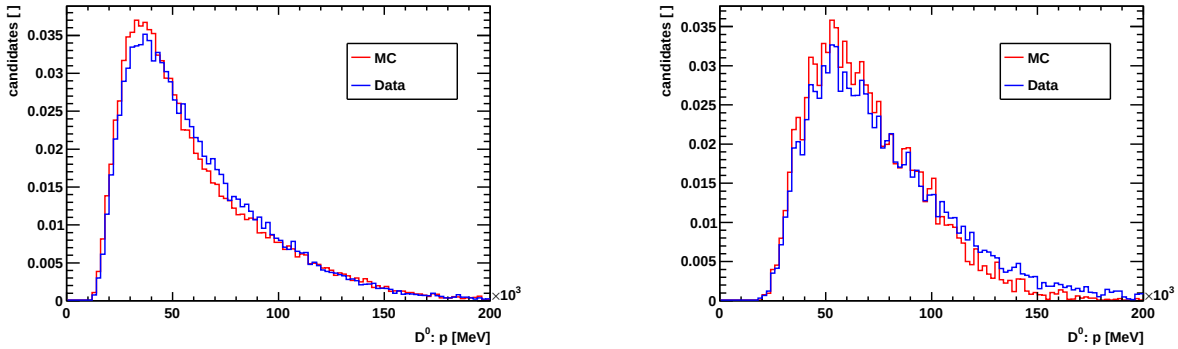

(a) Minimum Bias Data / MC: p spectra

(b) Signal Data / MC: p spectra

Figure 6.15.: Fake D^0's (a) and signal D^0's (b) momentum spectra.

The proper time resolution distributions in data and MC are fitted by Double-Gaussian distributions. The fit applied to the proper time distribution in minimum bias data is shown in figure 6.16. In data the proper time distribution is fitted with (69.26 ± 3.84) fs, in the original minimum bias MC it is fitted with (47.47 ± 2.96) fs and in the smeared minimum bias MC it is fitted with (68.92 ± 5.00) fs, see figure 6.17. A comparison of these values leads to the statement, that before the track resolution was smeared in MC the proper time resolution was significantly too good in the minimum bias MC, while after the track smearing the proper time resolution distributions in data and in minimum bias MC do agree very well. Hence, the track resolution smearing method works.

In the signal MC the D^0 proper time resolution is determined by subtracting the MC truth proper time from the reconstructed proper time. The track resolution smearing significantly changes the proper time resolution, from (33.68 ± 3.91) fs to (50.89 ± 11.38) fs, see figure 6.18. All values for the average width of the proper time resolution in minimum bias data, minimum

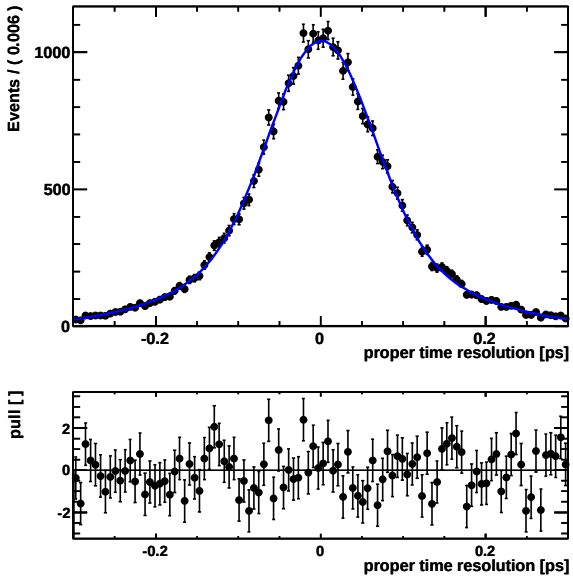

Figure 6.16.: Fake D^0's proper time resolution for minimum bias data. The distribution has an average width of (69.26 ± 3.84) fs.

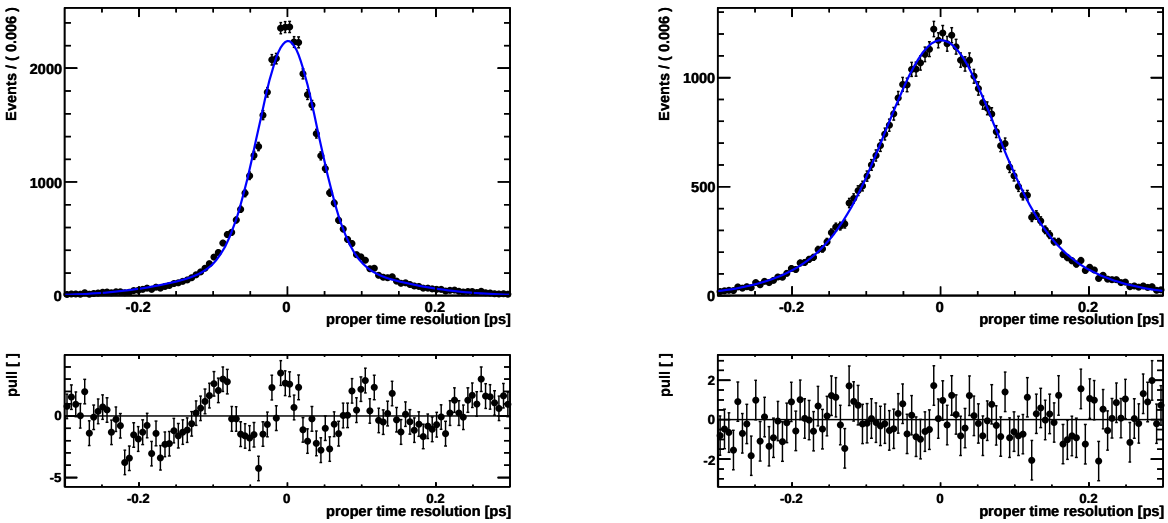

(a) MC minimum bias: original

(b) MC minimum bias: smeared

Figure 6.17.: Fake D^0's proper time resolution, minimum bias MC (a) original, (b) smeared. The original distribution has an average width of (47.47 ± 2.96) fs, while the smeared distribution has an average width of (68.92 ± 5.00) fs.

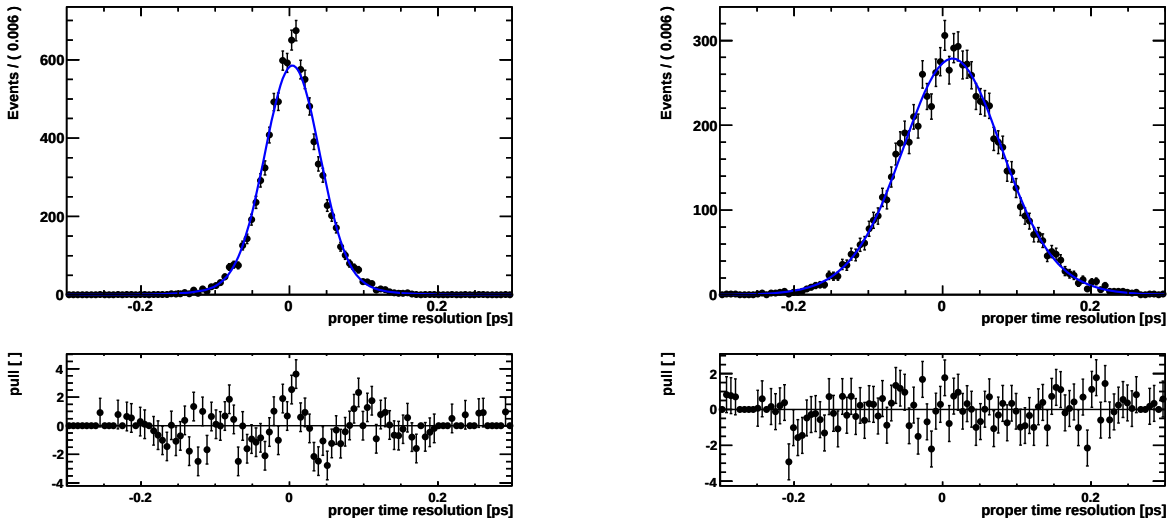

(a) MC signal: original

(b) MC signal: smeared

Figure 6.18.: True D^0's proper time resolution, MC (a) original, (b) smeared. The original distribution has an average width of (33.68 ± 3.91) fs, while the smeared distribution has an average width of (50.89 ± 11.38) fs.

bias MC and in the signal MC, both MC samples before and after the track resolution was smeared, are given in table 6.7a. The parameters of the fits to the minimum bias data proper time resolution and to the two smeared MC samples are given in table 6.7b. The proper time resolution distributions of the original MC samples are fitted by the same Double-Gaussian fit model as the smeared MC and the data proper time resolution distributions to demonstrate the track resolution smearing impact on the proper time resolution. As visible in the corresponding pull distributions, this fit model does not perfectly suit these narrow distributions.

6.6. Systematical Uncertainties

The systematical uncertainties due to the method of taking the proper time acceptance function from the MC simulation, are tested within three different MC samples, that differ slightly in the track resolution smearing around the optimal smearing, because the main uncertainty arises from the determination of the smearing parameters. The three MC samples were introduced in section 6.4.2.

The starting point is taking the proper time resolution, the proper time acceptance and the proper time distribution to be fitted from the same signal MC. The lifetime fit result is then the PDG lifetime, which was placed in the MC simulation. This is the reference value to compare the deviating fit results in "data" with, here $\pm 10\%$ smearing varied MC samples. The absolute deviation is then given as systematical uncertainty.

sample	resolution, original	resolution, smeared
data minimum bias [fs]	(69.26 ± 3.84)	—
MC minimum bias [fs]	(47.47 ± 2.96)	$(68.92\pm\ 5.00)$
MC signal [fs]	(33.68 ± 3.91)	(50.89 ± 11.38)

(a) Average widths of the proper time resolution in data, minimum bias MC and signal MC. The proper time resolutions of the minimum bias data sample and of the smeared minimum bias MC sample are in very good agreement.

Fit Parameter	Minimum Bias Data	Minimum Bias MC	Signal MC
Fraction f	0.429 ± 0.024	0.470 ± 0.043	0.449 ± 0.262
Mean μ [fs]	0.821 ± 0.492	0.793 ± 0.467	13.300 ± 0.804
σ_1 [fs]	139.000 ± 3.670	125.000 ± 3.630	85.400 ± 7.710
σ_2 [fs]	62.000 ± 1.300	68.400 ± 1.980	60.800 ± 6.630

(b) All parameters of the fits applied to the proper time resolution distributions in data, smeared minimum bias MC and smeared signal MC.

Table 6.7.: Table (a) gives an overview of the average proper time resolution fitted in minimum bias data, minimum bias MC and signal MC (both MC samples are fitted twice: before and after the track resolution was smeared). Table (b) summarizes the parameters fitted to the smeared MC proper time resolution distributions and to the proper time resolution in minimum bias data.

Due to the very tight signal selection, especially the requirement to have only one primary vertex per event, the statistics of the MC signal candidates go down rapidly. The statistical error on the lifetime fit result in MC is given in equation 6.14.

$$\Delta(\tau_{fit})(\text{stat.}) = \pm 4.5\,\text{fs} \tag{6.14}$$

6.6.1. Smearing Accuracy

The overall smearing accuracy effect is tested by taking the proper times of the optimal smeared MC sample to determine the proper time resolution and calculate the acceptance function. Then the proper times of the $\pm 10\%$ more or less smeared MC samples are fitted. This configuration covers the case, that the track resolution in data is within $\pm 10\%$ different compared to the smeared MC track resolution. To illustrate this test, the vice versa case, taking the resolution and acceptance function from the $\pm 10\%$ more or less smeared MC samples and the proper times to fit from the optimal smeared MC sample, is demonstrated below. The different acceptance functions for $\pm 10\%$ more or less smeared MC samples in comparison to the acceptance function of the optimal smeared MC sample are shown in figure 6.19. The overall smearing accuracy window of $\pm 10\%$ leads to an systematical uncertainty on the lifetime fit result, see equation 6.15:

$$\Delta(\tau_{fit})(syst.) = ^{+5.9}_{-2.3}\ \text{fs}\,. \tag{6.15}$$

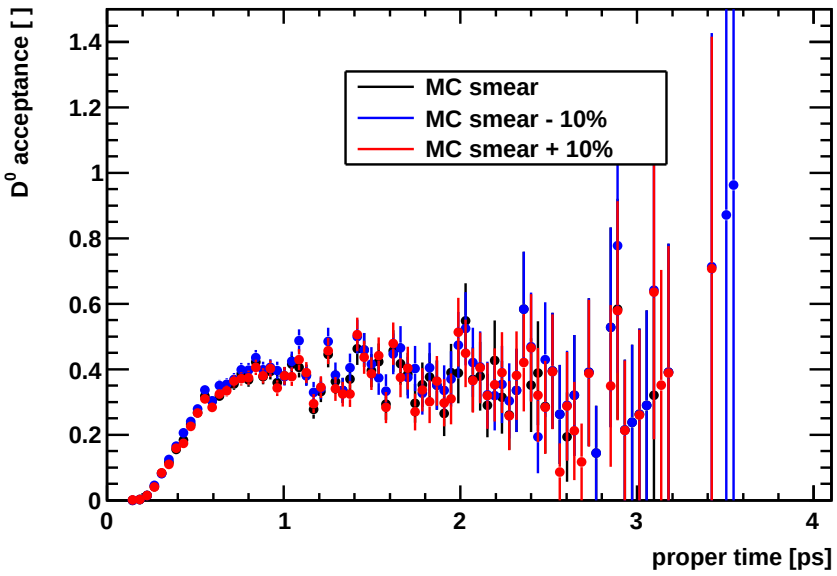

Figure 6.19.: D^0 proper time acceptance functions, the track resolution smearing parameters are varied with $\pm 10\%$ around the optimal values.

Due to the statistical uncertainty of the fit of 4.5 fs the upper uncertainty is most likely a statistical fluctuation. This track resolution smearing study was performed on an early reconstruction version. With later alignment and a bigger MC sample, this uncertainty is expected to decrease significantly.

6.6.2. Proper Time Resolution Bias

The proper time resolution mean value for signal candidates is not centered around zero like the proper time resolution distributions of the minimum bias MC and data samples, but it is biased to positive values, due to the displacement cuts of the trigger and the stripping selection that distort the proper time distribution especially for small proper times. To study, whether this bias is correctly simulated in MC, the proper time resolution is fitted in bins of the proper time: $[0.0, 0.1]$ ps, $[0.1, 0.2]$ ps, ..., $[0.8, 0.9]$ ps, shown in figure 6.20. The bias decreases with increasing proper times. This is illustrated in figure 6.21, where the bias is plotted as a function of the proper time. The proper time resolution bias is at the maximum, around 0.2 ps, at small proper times between $0.0 - 0.1$ ps. It vanishes for proper times greater than 0.8 ps. In between it decreases continuously. This bias occurs due to the displacement cuts of the signal selection. The impact parameter cuts on the D^0 daughters and the flight distance cuts on the D^0 require a minimum separation distance to the primary vertex. For D^0s with very short proper times these cuts make statistical fluctuations apparent. Proper times fluctuating to smaller values are discriminated, the ones fluctuating to greater values are accepted. Especially for small proper times these fluctuations preponderate. This is a so called "edge effect".

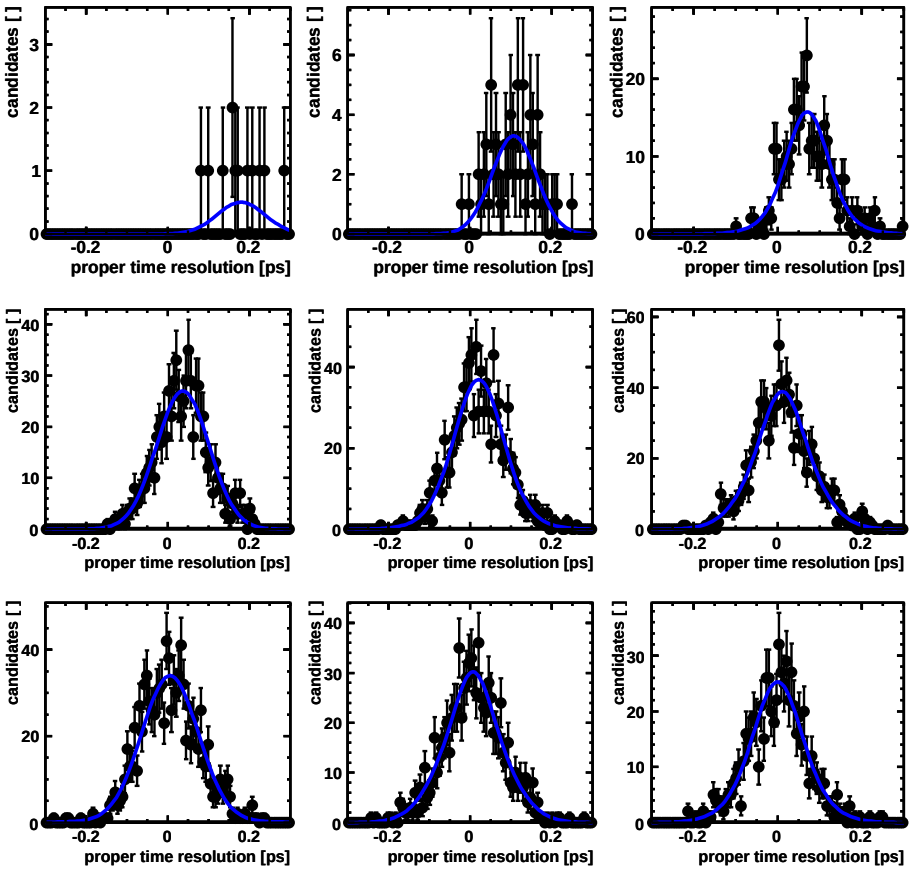

Figure 6.20.: D^0 proper time resolution in bins of the D^0 proper time. The upper left plot shows the proper time bin $[0.0, 0.1]$ ps, the upper middle plot shows the proper time bin $[0.1, 0.2]$ ps, ..., the lower right plot shows the proper time bin $[0.8, 0.9]$ ps.

To test the impact on the lifetime fit result, if the resolution bias in data is different to the bias in MC, values for the resolution bias are calculated in bins of the proper time for the optimal smeared MC and the $\pm 10\%$ more and less smeared MC samples. Then the bias values are subtracted from each other. The differences are shown in figure 6.22. As expected, the bias is overall smaller in the 10% less smeared MC sample, hence the relative bias is negative, shown in figure 6.22 (a). It is overall bigger in the 10% more smeared MC sample, hence the relative bias is positive, shown in figure 6.22 (b). Each bias difference as a function of the proper time is taken as a Gaussian width to draw a Gaussian random number t_{random}. Then t_{random} is added on the optimal smeared MC proper times. These modified proper times are fitted by the proper time resolution and acceptance function determined on the optimal smeared MC sample.

The proper time resolution mean bias uncertainty leads to a systematical uncertainty on the lifetime fit result of, equation 6.16:

$$\Delta(\tau_{fit}) = ^{+2.4}_{-2.7} \text{ fs}\,. \tag{6.16}$$

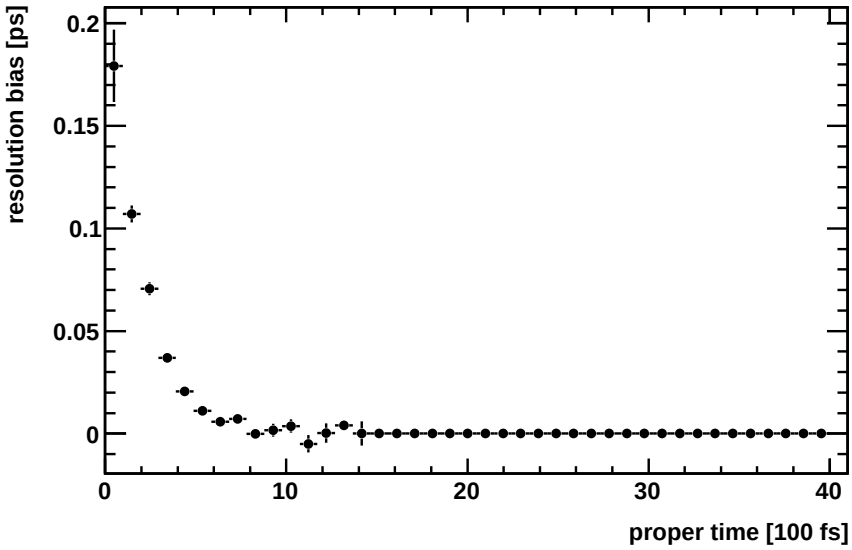

Figure 6.21.: D^0 proper time resolution mean values plotted against D^0 proper time bins. Each point is placed at the upper lifetime bin border.

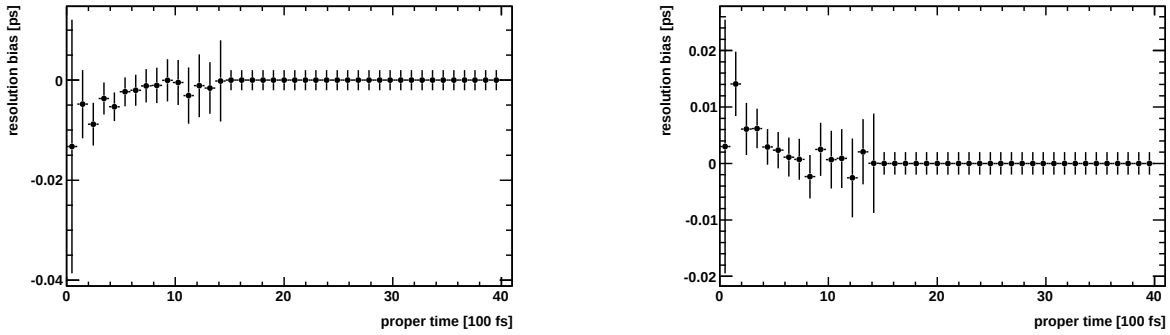

(a) bias: MC(smear - 10%) - MC(smear)

(b) bias: MC(smear + 10%) - MC(smear)

Figure 6.22.: Proper time resolution bias differences for (a) the 10% less smeared MC relative to the optimal smeared MC, (b) the 10% more smeared MC relative to the optimal smeared MC.

6.6.3. Lifetime Resolution Width

Without being able to measure the proper time resolution in signal data, the following assumption was made. The smeared signal MC proper time resolution describes the data distribution acceptably, due to the fact that the fake D^0s proper time distributions agree between the smeared MC and the data. To test now the impact on the lifetime fit result, when the true signal data proper time resolution width differs within the $\pm 10\%$ track resolution frame from the smeared signal MC proper time resolution width, the differences between the optimal smeared MC resolution average width and the ones of the $\pm 10\%$ more and less smeared MC samples are computed. See equation 6.17 and equation 6.18.

$$\sigma_+ = \sqrt{|\bar{\sigma}^2(MC_{opt}) - \bar{\sigma}^2(MC_{+10\%})|} \tag{6.17}$$

$$\sigma_- = \sqrt{|\bar{\sigma}^2(MC_{opt}) - \bar{\sigma}^2(MC_{-10\%})|} \tag{6.18}$$

However, this is only an estimation for the case that the proper time resolution will be broader in data than in MC. To test this case, the maximum of σ_+ and σ_- is taken to draw Gaussian random numbers. The random numbers are then added on the proper times of the optimal smeared MC sample. With these modified MC proper times an acceptance function is computed, as shown in figure 6.23. To demonstrate the change in the acceptance function when the proper time resolution width is slightly different, the optimal acceptance function is also plotted.

This technique gives only an estimate on the upper limit of the uncertainty. Nevertheless, it can be assumed, that the uncertainty is symmetric. Hence, the resolution width uncertainty leads to an systematical uncertainty on the lifetime fit result of, equation 6.19:

$$\Delta(\tau_{fit}) = \pm 0.5\,\text{fs}\,. \tag{6.19}$$

6.6.4. Summary

The data track resolution could be achieved in MC by the smearing method up to an uncertainty of $\pm 10\%$. In this range it is assumed that the signal data and smeared MC proper time resolutions agree. The lifetime fit method is tested for systematical uncertainties due to this track resolution uncertainty. The difference in the acceptance function due to the smearing uncertainty gives a systematical uncertainty of $^{+5.9}_{-2.3}$ fs. The signal proper time resolution bias gives a systematical uncertainty of $^{+2.4}_{-2.7}$ fs. Finally, the difference in the signal proper time resolution width gives a systematical uncertainty of ± 0.5 fs. However, the statistical error of the MC test sample is ± 4.5 fs. Thus, the upper limit of the systematical uncertainty due to the smearing accuracy is most likely a statistical fluctuation. The study should be definitively repeated on a bigger MC sample, that was at the time of this thesis not available. Additionally, toy studies should be done on MC to determine the limiting factor of this method with a better significance. The total systematical uncertainty of this method is, equation 6.20:

$$\Delta\tau(syst.) = \sqrt{5.9^2 + 2.7^2 + 0.5^2}\,\text{fs} = 6.5\,\text{fs} \tag{6.20}$$

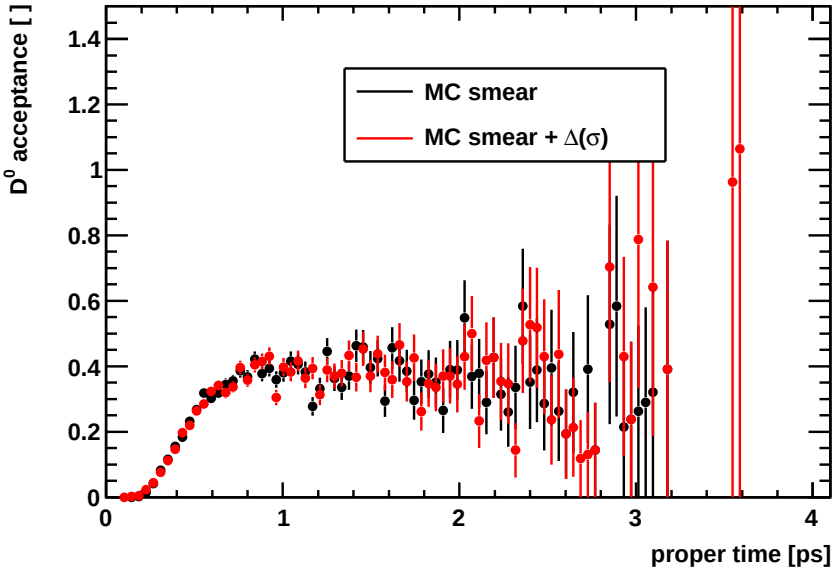

Figure 6.23.: D^0 proper time acceptance functions. The red function tests the case, that the proper time resolution in data is 10% broader in data than in MC. The black function represents the case, that the proper time resolution is exactly the same in data and the optimal smeared MC.

With later alignment versions the smearing accuracy will be improved. Most likely, then this method won't be systematically limited. The current world average uncertainty on the D^0 lifetime is 1.5 fs [19].

6.7. Selection Fine Tuning

A very powerful cut to reject hadronic background is the IP significance and the flight distance significance. These cuts require a minimum distance to the primary vertex and an maximum error estimate on this distance. In this thesis the mean track resolution in MC was adapted to the worse track resolution in data. However, the error estimate were not affected by this corrective method. They are determined by the number of hits per track and the hits' errors. Hence, in data the error estimates are still slightly bigger than in MC. In principle, this instance does not disrupt the lifetime measurement. Only to assure that the same events are selected in data and MC the error estimates in MC are scaled or reweighted to imitate the shape of the error distribution in data. The stripping selection cuts on the squared IP significance of the D^0 daughters and on the squared flight distance significance of the D^0. Additionally, the final selection cuts harder in the daughters' IP and IP error distributions and in the D^0's flight distance and flight distance error distributions to redo the stripping cuts with the adapted error distributions in MC.

6.7.1. D^0 Daughters IP Error Scaling

The impact parameter error estimate for the D^0 daughters is slightly different in the smeared signal MC and in signal data due to the different detector performance of data taking and simulation conditions. Figure 6.24 shows the IP error distributions of the D^0 daughters before and after this distribution was corrected in MC. To correct for this difference, the IP errors are fitted by

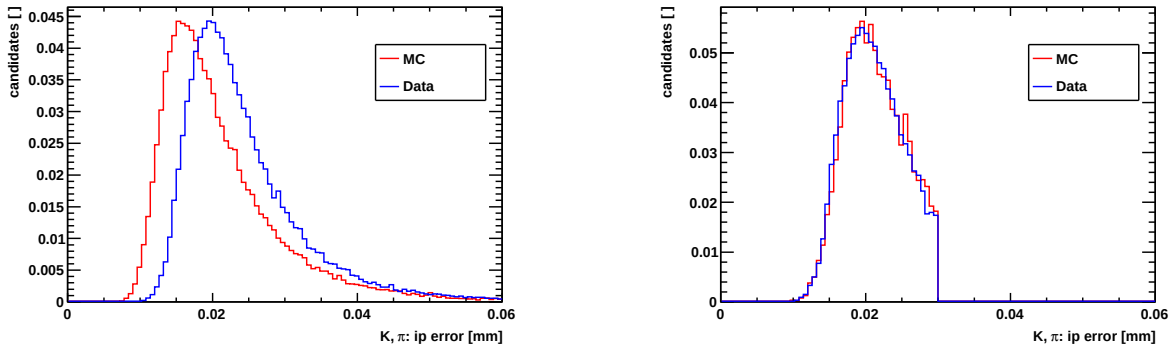

(a) D^0 daughters IP_{error} distributions before scaling

(b) D^0 daughters IP_{error} distributions after scaling

Figure 6.24.: D^0 daughters impact parameter error distributions (a) before scaling, (b) after scaling.

single Gaussians in bins of the inverse transverse momentum. The mean values of these Gaussians are then plotted against the inverse transverse momentum. To calculate a scaling factor for the daughter's impact parameter error the IP error Gaussian mean values of the data are divided by the MC IP error Gaussian mean values as a function of the inverse transverse momentum. Then this ratio is fitted by a quadratic polynomial:

$$f(x) = a + bx + cx^2 \,. \tag{6.21}$$

The fitted scaling factors as a function of the inverse transverse momentum are shown in figure 6.25. The parameters corresponding to the fits applied to the IP error scaling distributions are listed in table 6.8. The D^0 daughter's IP errors in MC are scaled by the fitted polynomial

particle	a	b	c
K	1.4299 ± 0.0034	-625.311 ± 13.212	302622 ± 12043
π	1.4082 ± 0.0041	-550.667 ± 14.512	285333 ± 11023

Table 6.8.: Fitted parameter for the D^0 daughters IP error scaling.

before the final selection selects the signal candidates.

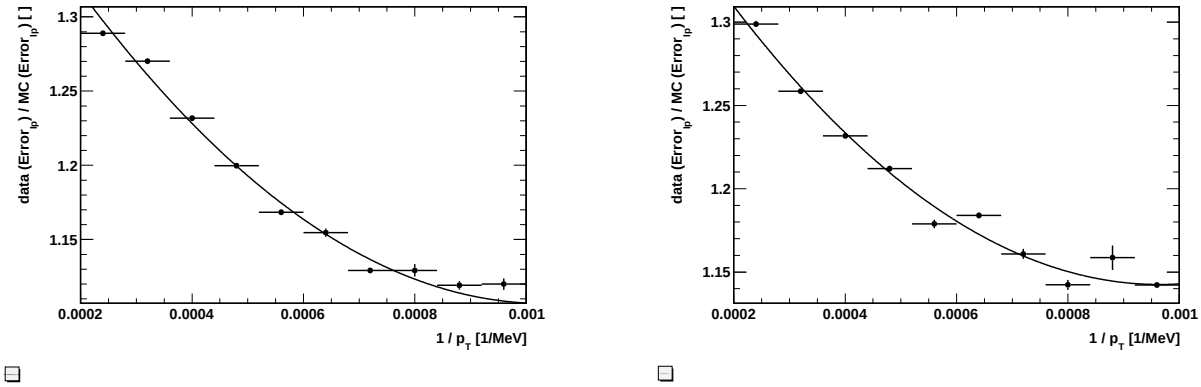

(a) K: IP error scale

(b) π: IP error scale

Figure 6.25.: Fitted IP error scaling factors for the D^0 daughters K (a), π (b).

6.7.2. 2D Reweighting: D^0 Momentum Versus Flight Distance Error

The D^0 momentum spectrum is higher in data than in MC, see figure 6.26. So all MC quantities need to be reweighted by a data MC momentum ratio. As mentioned above also the flight

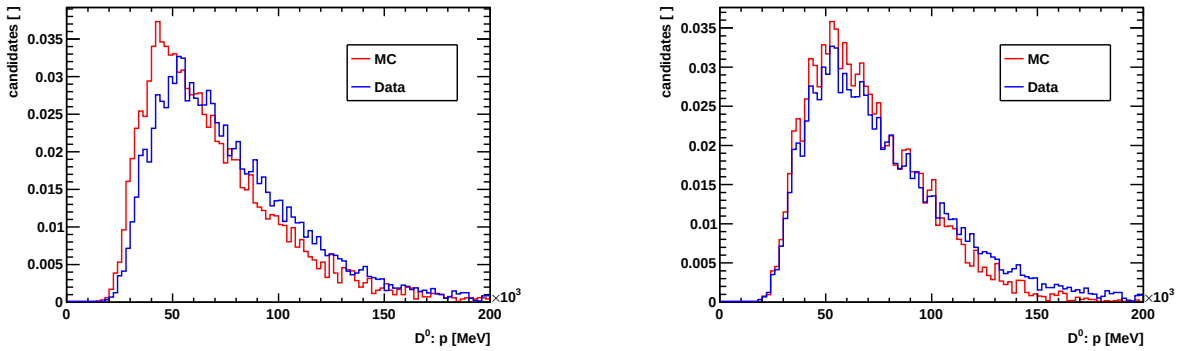

(a) D^0 momentum spectrum before reweighting

(b) D^0 momentum spectrum after reweighting

Figure 6.26.: D^0 momentum distributions for data and MC, (a) before MC reweighting, (b) after MC reweighting. The data momentum distribution is mass sideband subtracted.

distance error prediction in MC is slightly too small compared to data, see figure 6.27. Hence, in MC it also needs to be corrected, because in the stripping selection contains a squared flight distance significance cut. To treat correlations between the D^0 momentum and the flight distance error distributions correctly two-dimensional weights corresponding to these quantities are calculated. The two-dimensional histograms of D^0 p versus D^0 fD_{error} for data and MC are shown in figure 6.28. The ratio of these two two-dimensional histograms yields the two-dimensional weighting histogram, shown in figure 6.29. All MC distributions are reweighted by the above defined

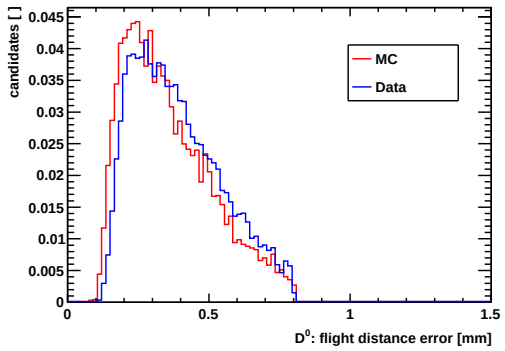

(a) D^0 flight distance error before reweighting

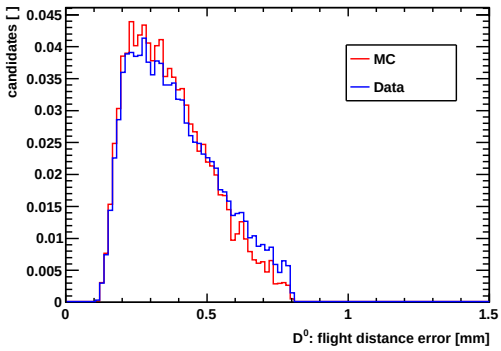

(b) D^0 flight distance error after reweighting

Figure 6.27.: D^0 flight distance error distributions for data and MC, (a) before reweighting, (b) after reweighting. The smearing did not affect the MC error estimates. The data flight distance error distribution is mass sideband subtracted.

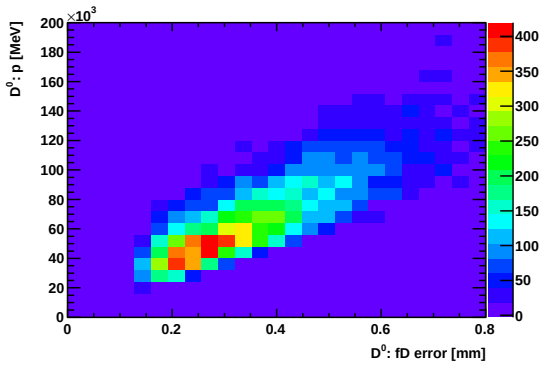

(a) Data: 2D histogram for D^0 momentum vs flight distance error

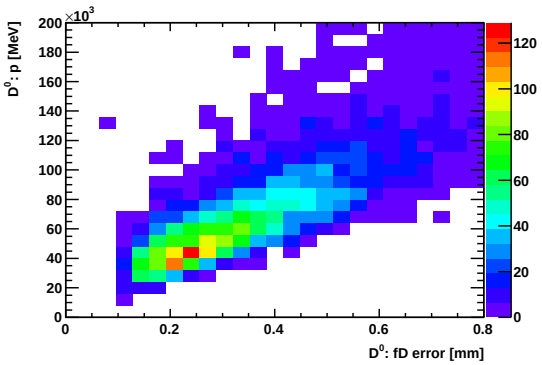

(b) MC: 2D histogram for D^0 momentum vs flight distance error

Figure 6.28.: D^0 momentum versus flight distance error, (a) data, (b) MC.

two-dimensional weighting histogram. After the fine tuning procedure on MC all lifetime related quantities agree in data and MC.

In the following, all the quantities correlated to the lifetime are shown in form of data-MC comparisons. First, the quantities of the D^0 daughters are shown, second, the quantities of the D^0 itself are shown. The momentum spectrum of the D^0 daughters agrees in data and MC, see figure 6.30. The daughters impact parameter distribution is in agreement due to the track smearing method and the IP error distribution is now in agreement due to the IP_{error} scaling method, see figure 6.31.

Due to the agreement in the IP and IP error distributions the IP χ^2 distribution is now also in agreement for the D^0 daughters, see figure 6.32. The agreement in this quantity is essential for

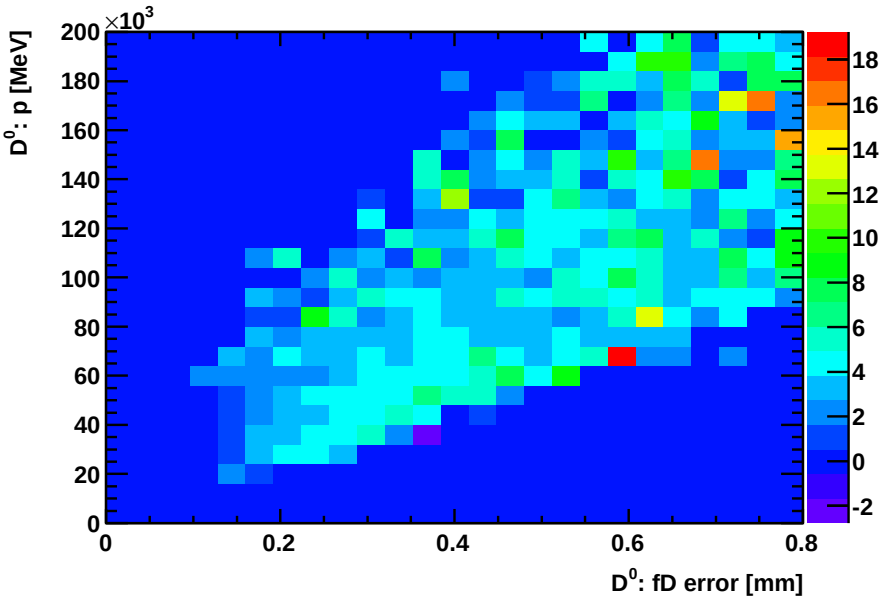

Figure 6.29.: D^0 momentum versus flight distance error weights. The data 2D histogram was divided by the MC 2D histogram.

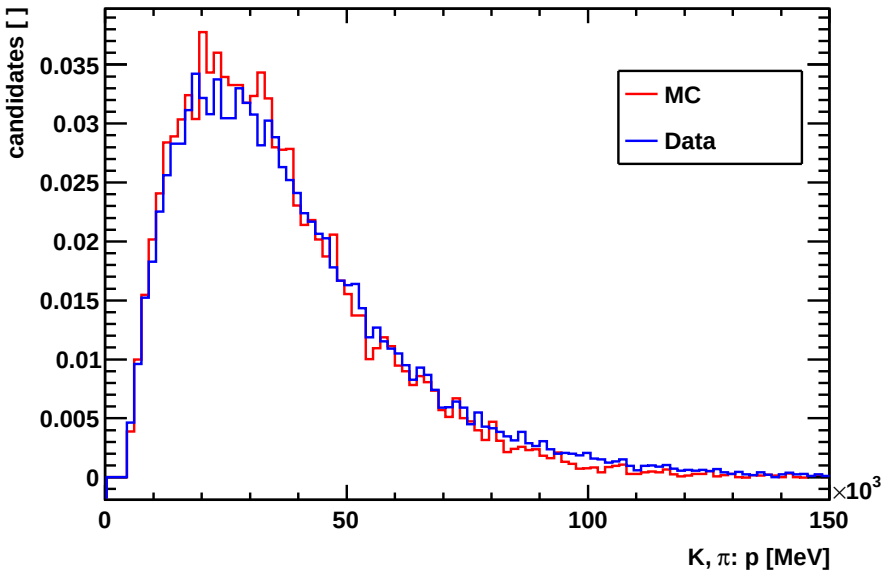

Figure 6.30.: K, π: momentum distribution.

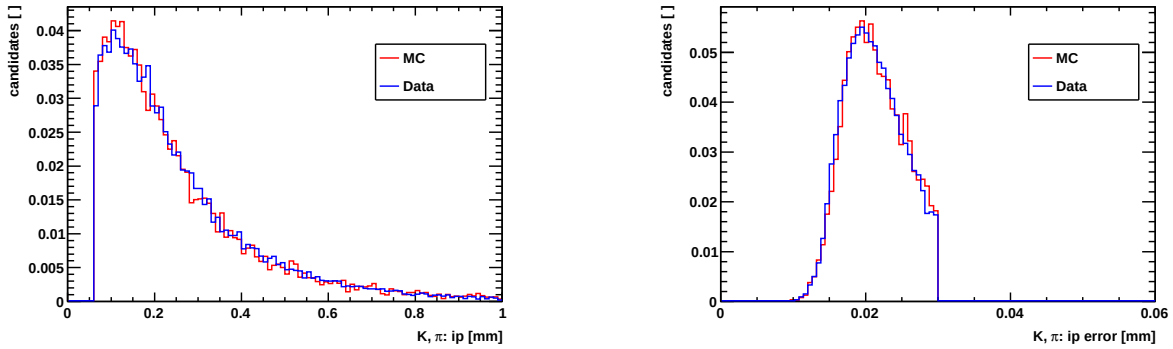

(a) K, π: impact parameter

(b) K, π: impact parameter error (scaled)

Figure 6.31.: K, π: impact parameter (a) and impact parameter error (b). After the impact parameter error scaling we observe good agreement.

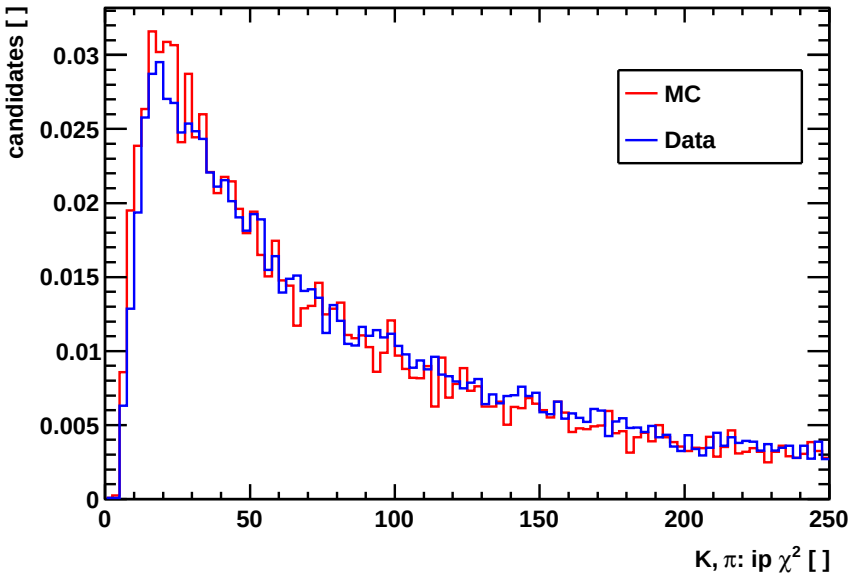

Figure 6.32.: K, π: impact parameter χ^2 distribution after reweighting. Agreement in this quantity is essential to model the lifetime acceptance function correctly in MC, due to the selection effects.

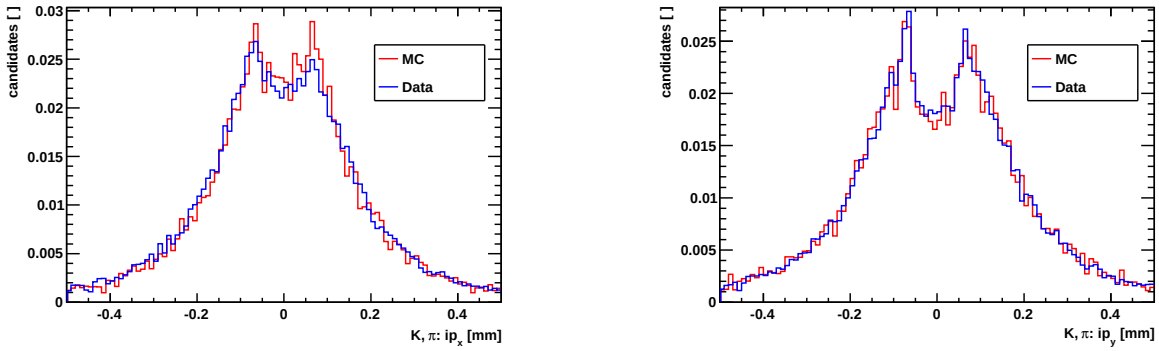

(a) K, π: IP_x distribution

(b) K, π: IP_y distribution

Figure 6.33.: K, π: impact parameter projection on the x axis (a) and on the y axis(b) after the reweighting. The distributions are in good agreement. The dip in their maxima around zero, because the kaons and pions are produced in the displaced D^0 decay vertices.

the analysis modeling the lifetime acceptance in MC, because cutting on the daughters impact parameter directly distorts the D^0 proper time distribution. While the IP χ^2 cut requires also a maximum limit on the IP error estimate, the bias in MC was different from the one in data, if the error estimate was different. Hence, by scaling the IP error and smearing the track resolution the same proper time distorting effect can be modeled in MC. The daughters IP_x and IP_y projections are in good agreement, see figure 6.33. The dip in the IP_x and IP_y distributions is due to the fact that the daughters are produced in the displaced D^0 decay vertex, not in the primary vertex.

Additionally a cut was done to require a minimum number of VELO hits per daughters track, see figure 6.34. If we have less than 4 hits on a track the IP resolution is dominated by the scaling between the first hit and the point of closest approach. Thus with a minimum requirement on the number of VELO hits the selection is independent of these resolution effects. In this selection the cut requires a minimum of eleven hits. The impact parameter distributions of the D^0 are

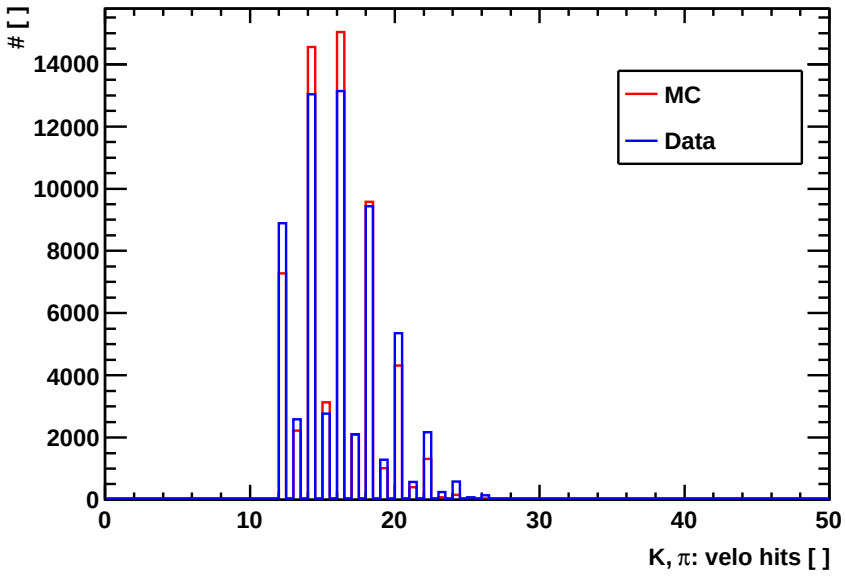

Figure 6.34.: K, π tracks: number of VELO hits per track.

after reweighting also in agreement in MC and data, while the IP error estimate is not. However, this does not matter, because there is no cut on the D^0s IP significance. Both distributions are shown in figure 6.35. The impact parameter projections on the x and y axis of the D^0 are given in figure 6.36. These distributions are not affected by the momentum reweighting. The IP_x distribution in data is not centered around zero. This is an effect of the beam crossing angle, which is not properly described in MC. The D^0 flight distance distribution is the quantity most correlated to the lifetime. Due to the primary vertex displacement cut of the stripping selection, which requires a minimum flight distance significance limit, the flight distance error estimate has to be treated with most care. Hence, additionally to the D^0 momentum the flight distance error is used for reweighting. After reweighting the flight distance and flight distance error distribution agree in data and MC, see figure 6.37. The D^0 primary vertex displacement distributions for data

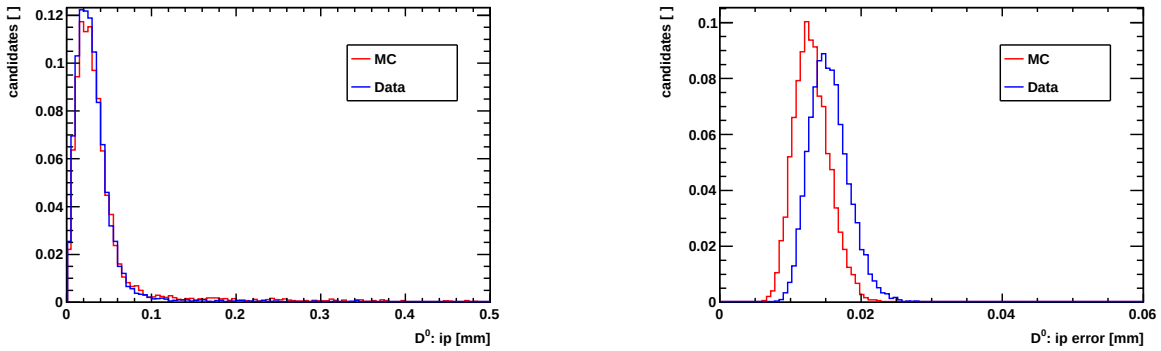

(a) D^0: impact parameter (b) D^0: impact parameter error (scaled)

Figure 6.35.: D^0: impact parameter (a) and impact parameter error (b). After reweighting the IP also agrees, the IP error does not, nevertheless it is not used.

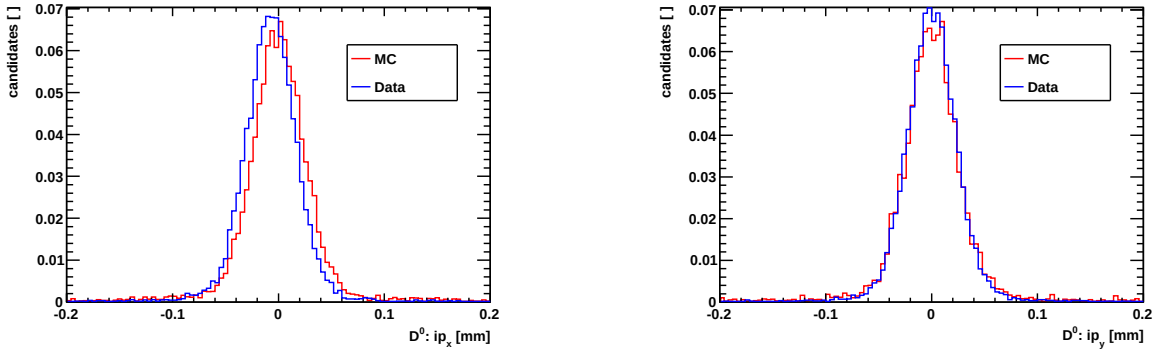

(a) D^0: IP_x distribution (b) D^0: IP_y distribution

Figure 6.36.: D^0: impact parameter projections on the x (a) and y (b) axis. The IP resolution is not affected by the momentum reweighting. The IP_x distribution in data is not centered around zero. That is an effect of the shifted beam position, which is not properly described in MC.

and MC are shown in figure 6.38.

This section showed, that data-MC comparisons have to be treated very careful to achieve agreement. Several corrective measures were necessary to guarantee that the same distortion of the proper time distribution is simulated in MC. Having achieved this agreement it is now possible to perform the fits on data, which use MC templates.

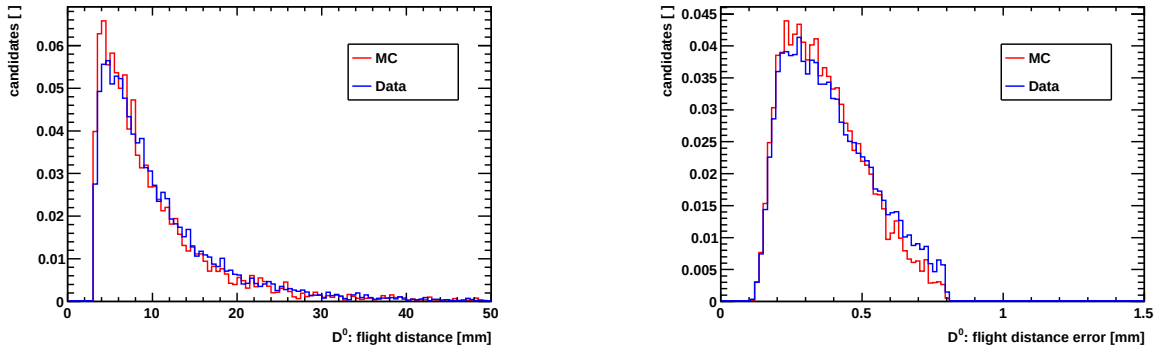

(a) D^0: flight distance

(b) D^0: flight distance error

Figure 6.37.: D^0: flight distance (a) and flight distance error estimate (b) distributions after reweighting. The flight distance error contributes in the two-dimensional reweighting.

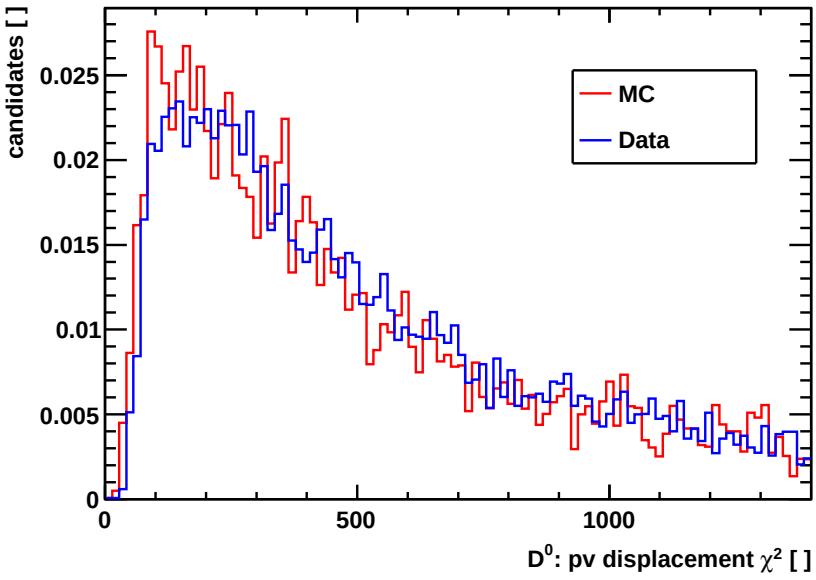

Figure 6.38.: D^0: primary vertex displacement distributions (squared flight distance significances) after reweighting.

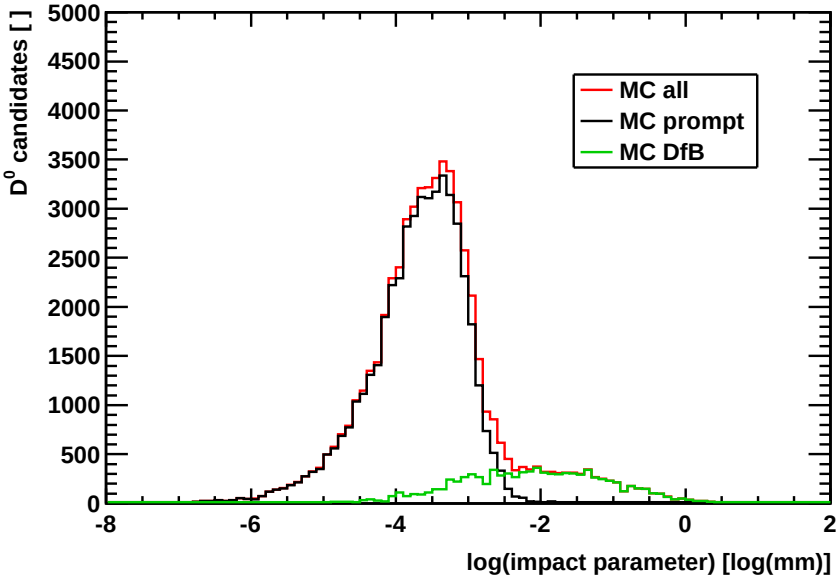

Figure 6.40.: Logarithmic IP distributions of the D^0 with MC truth information: the red curve is a composition of the D^0 from B curve (green) and the prompt D^0 curve (black).

6.8. Prompt and Secondary D^0s Separation

Most of the reconstructed signal D^0s are decay products of D^*s that are coming directly from the primary vertex. These D^0s are called prompt D^0s. Besides, there is a certain fraction of D^0s, that are misreconstructed as prompt D^0s, but this fraction is composed of D^0s that are decay products of B mesons. The B mesons are not reconstructed, otherwise the D^0s coming from Bs could be marked as background. These camouflaged background D^0s are called secondaries. For a lifetime measurement it is necessary to separate the prompt and secondary D^0s, because the secondaries are biased to longer lifetimes due to the undetected B mesons, that have a certain lifetime themselves. The impact parameter (IP) of the D^0 with respect to the closest primary vertex gives a handle on the prompt and secondaries separation. Secondary D^0s have larger impact parameters than prompt D^0s, clearly visible as a small bump next to the main peak in the $\log(Ip)$ distribution, shown in figure 6.39. Additionally, the D^0 $\log(IP)$ distribution of the

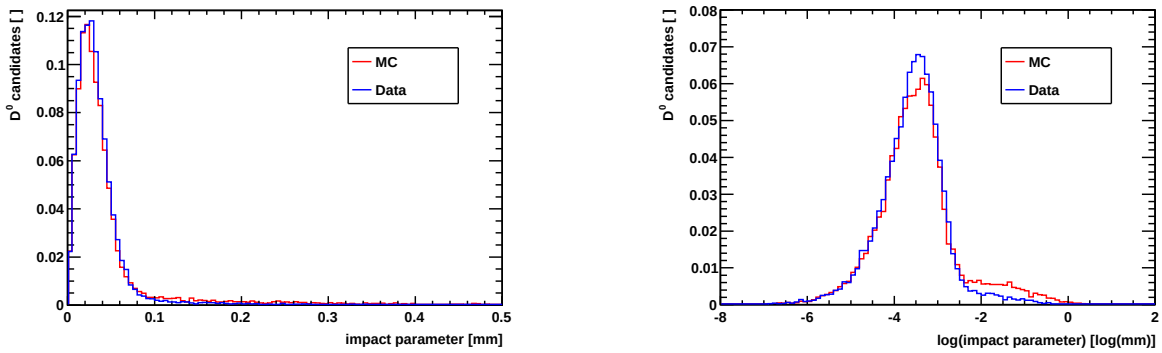

(a) IP D^0 (b) $\log(IP)$ D^0

Figure 6.39.: Normalized impact parameter distributions of the D^0. (a) IP, (b) $\log(IP)$.

smeared MC is a sensitive probe to the track smearing. Due to the fact, that the absolute IP is the spacial integral over its three components in x, y and z direction, shown in figure 6.39, it is shifted relative to the data distribution, if the components do not agree in data and MC. On MC the full history of the particles is written out. With the help of MC truth information, it is possible to look up whether the D^0 is prompt or secondary (called D from B, short DfB), see figure 6.40. To get the DfB fraction from data, the $\log(Ip)$ distribution has to be fitted. This is done within two steps. The entire PDF is composed of two parts, the prompt part and the secondaries part, connected through the DfB fraction f, see equation 6.22.

$$PDF(\log(IP)) = (1-f)\cdot PDF_{\text{prompt}} + f \cdot PDF_{\text{secondaries}} \tag{6.22}$$

The prompt PDF is a composition of three Bifurcated-Gaussian (BG) distributions, see equation 6.23:

$$PDF_{\text{prompt}}(\log(IP)) = (1-f_2)\cdot((1-f_1)\cdot BG_1 + f_1 \cdot BG_2) + f_2 \cdot BG_3 \tag{6.23}$$

A Bifurcated-Gaussian distribution is defined as a normal Gaussian distribution but with different widths on each side of the mean value μ, see equation 6.24:

$$BG(x;\mu,\sigma_L,\sigma_R) \sim \begin{cases} e^{-\frac{(x-\mu)^2}{2\sigma_L^2}} & \text{if } x < \mu \\ e^{-\frac{(x-\mu)^2}{2\sigma_R^2}} & \text{if } x > \mu \end{cases} \tag{6.24}$$

The parameters of the triple BG in PDF_{prompt} are the following: one mean value μ, two fractions f_1 and f_2, three left widths $\sigma_{L,1}$, $\sigma_{L,2}$ and $\sigma_{L,3}$ and three right widths $\sigma_{R,1}$, $\sigma_{R,2}$ and $\sigma_{R,3}$. They are determined by the fit to the MC prompt D^0 $\log(IP)$ distribution. Due to the MC truth information, no background has to be included in the fit routine. The secondaries PDF is taken directly from MC as a histogram shape. The fit to the prompt D^0 $\log(IP)$ distribution is shown in figure 6.41. The corresponding fitted parameters are listed up in table 6.9.

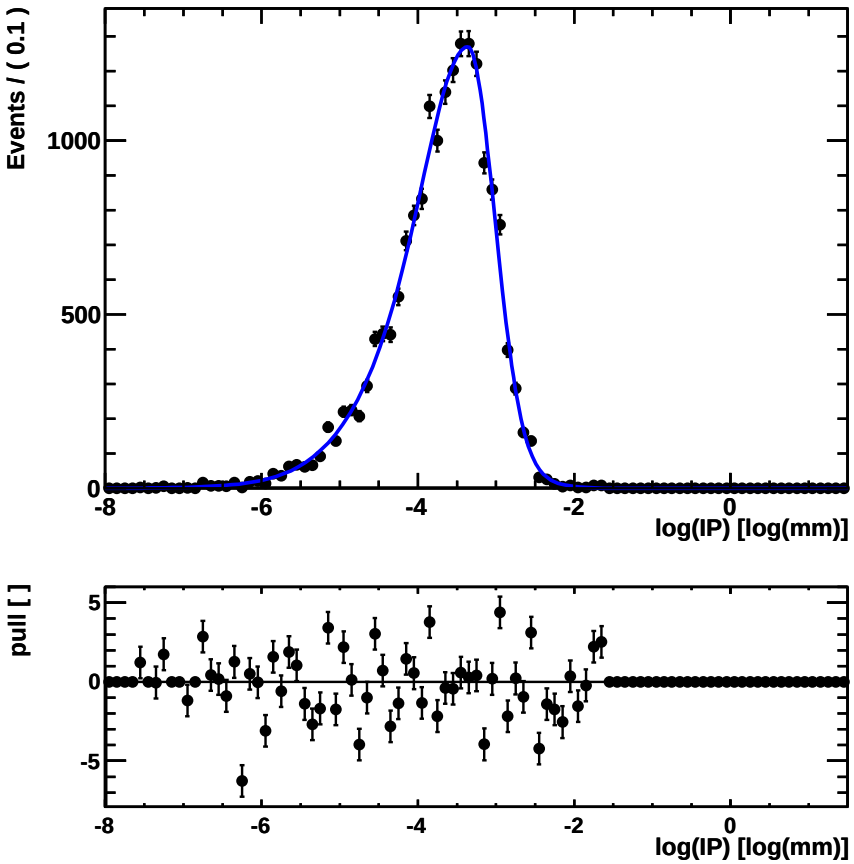

Figure 6.41.: Prompt fit: D^0s from prompt D^*s MC truth, no B in the decay chain. In this MC prompt fit the fit parameters are determined and later on fixed.

To fit the data distribution the prompt PDF (with fixed parameters) is added up by the DfB histogram PDF, that is a spline to the $\log(IP)$ distribution in MC of the D^0s coming from

Fit Parameter	Fitted Value
f_1	0.701 ± 0.038
f_2	0.949 ± 0.007
μ [log (mm)]	-3.360 ± 0.009
$\sigma_{L,1}$ [log (mm)]	0.684 ± 0.021
$\sigma_{L,2}$ [log (mm)]	1.243 ± 0.037
$\sigma_{L,3}$ [log (mm)]	0.263 ± 0.065
$\sigma_{R,1}$ [log (mm)]	0.339 ± 0.011
$\sigma_{R,2}$ [log (mm)]	0.339 ± 0.033
$\sigma_{R,3}$ [log (mm)]	0.600 ± 0.032

Table 6.9.: D^0 Prompt log (Ip) Fit. The fit is performed on MC, to determine the fit parameters for prompt D^0s.

B decays. The DfB histogram was shown (as a green curve) in figure 6.40. The D^0 log (IP) distribution is D^0 mass sideband subtracted. So the only fit parameter left free to be fitted in data is then the DfB fraction between the prompt and the secondaries PDF.

Counting the number of D^0 from B decays in MC yields a DfB fraction of 13.31%. The log (IP) fit applied to MC is shown in figure 6.42. It determines in MC a DfB fraction, given in equation 6.25,

$$(12.44 \pm 0.27)\% \,, \tag{6.25}$$

which is significantly smaller. The log (IP) fit applied to data is shown in figure 6.43. It might have also underestimated the DfB fraction in data, which is determined to be, see equation 6.26,

$$(5.16 \pm 0.20)\% \,. \tag{6.26}$$

Nevertheless, this systematical uncertainty of the fit method of about 1% can not explain the huge difference between the MC and the data DfB fractions, that differ more than a factor of 2. Even by eye this difference was already visible in figure 6.39 (b). So most likely the DfB fraction was not correctly simulated. Unfortunately the lifetime fit is very sensitive to the DfB fraction. So this quantity yields a large systematic uncertainty for the lifetime determination, and also for further D mixing analyses.

6.9. Trigger on Data

In the early data taking period, the trigger settings were changed several times. The data used in this thesis was fortunately triggered by almost one trigger configuration.[6] However, the trigger configuration only is not sufficient to simulate the trigger cuts in MC completely. It is also important to know, which event did release the trigger, if it was the D^0 decay or another event and the D^0 decays was recorded as well. To investigate this effect a study of the composition of

[6] 3/4 of the Stripping 07 magnet down data was taken with the Trigger Configuration Key (TCK) 17001F.

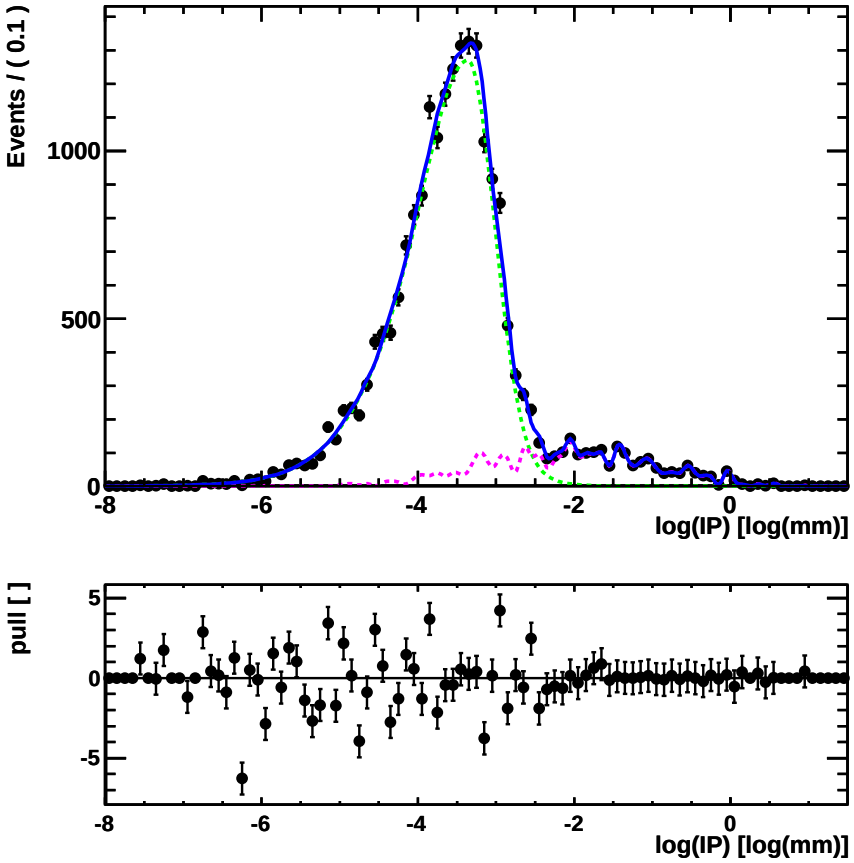

Figure 6.42.: $D^0 \log(Ip)$ Fit in MC. The entire distribution, containing the prompt and the secondaries part, is fitted by the solid blue line. The dashed green line indicates the prompt part and the dashed magenta line indicates the secondaries (DfB) part.

the trigger decisions is necessary. Unfortunately, the complete trigger simulation was not available at the time of this thesis.

6.10. Fit Procedure

This section shortly summarizes the steps, which are necessary to perform the final fit to the D^0 proper time distribution in data. First, the proper time resolution parameters are fitted in MC. Second, the proper time acceptance function is calculated in MC using the proper time resolution fit results, see figure 6.44. In MC the acceptance distribution is calculated by dividing the reconstructed MC D^0 proper time distribution by the lifetime exponential convolved with the proper time resolution. The lifetime fit uses a spline to this distribution as an average proper time acceptance function. Third, the D^0 from B proper time distribution is taken from MC as a histogram PDF, shown as a green curve in figure 6.45. Additionally, the D^0 from B fraction in

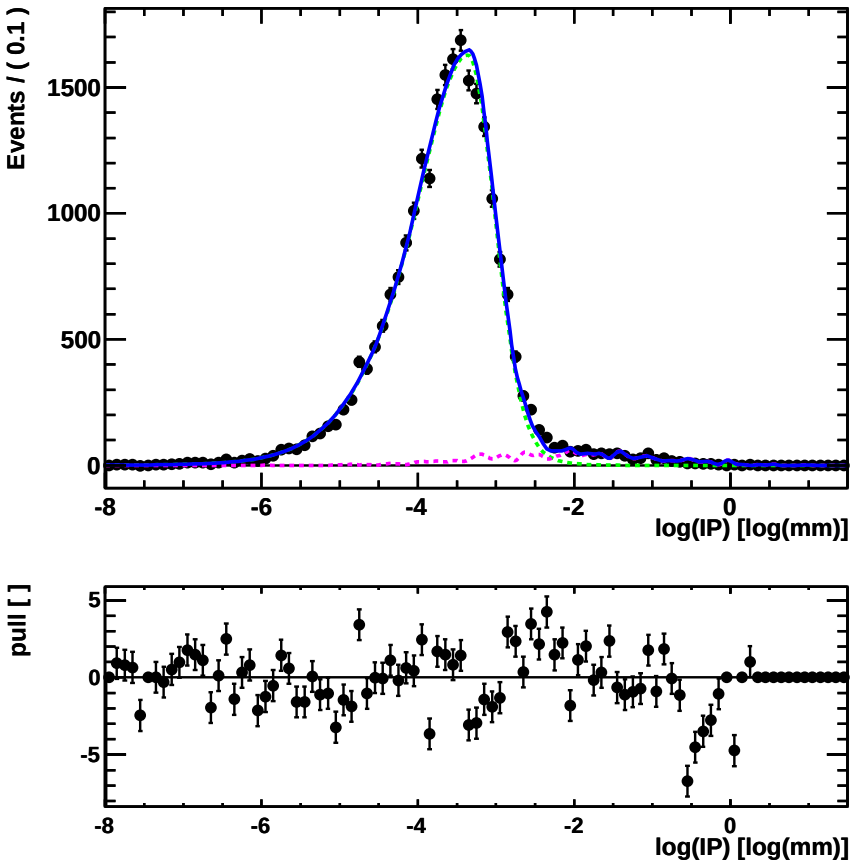

Figure 6.43.: D^0 $\log(Ip)$ Fit in Data. The entire distribution, containing the prompt and the secondaries part, is fitted by the solid blue line. The dashed green line indicates the prompt part and the dashed magenta line indicates the secondaries (DfB) part.

data is determined in the separate fit to the D^0 $\log(IP)$ distribution in data. Finally, all parts are put together, the resolution parameters, the acceptance function, the DfB fraction f and the $PDF_{secondary}$ to fit the only parameter left in data τ_{fit} in data.

6.11. Lifetime Fit Results on Data

The entire fit procedure is validated on MC, see figure 6.46. The fit result for the D^0 lifetime in MC is $\tau_{fit} = (408.809 \pm 3.142)\,\text{fs}$. Within the statistical error this is exactly the lifetime, which was put into the simulation. The pull distribution in figure 6.46 clearly shows this correlation. The proper time acceptance function was determined on the same MC sample as this validation fit. An improvement of the method will be to replace the acceptance spline by a smooth function that is fitted to the acceptance distribution.

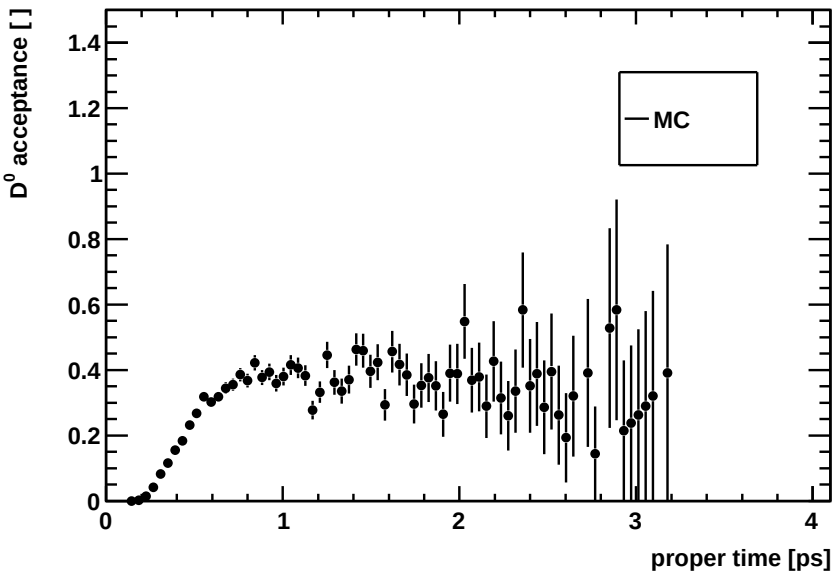

Figure 6.44.: D^0 proper time acceptance distribution.

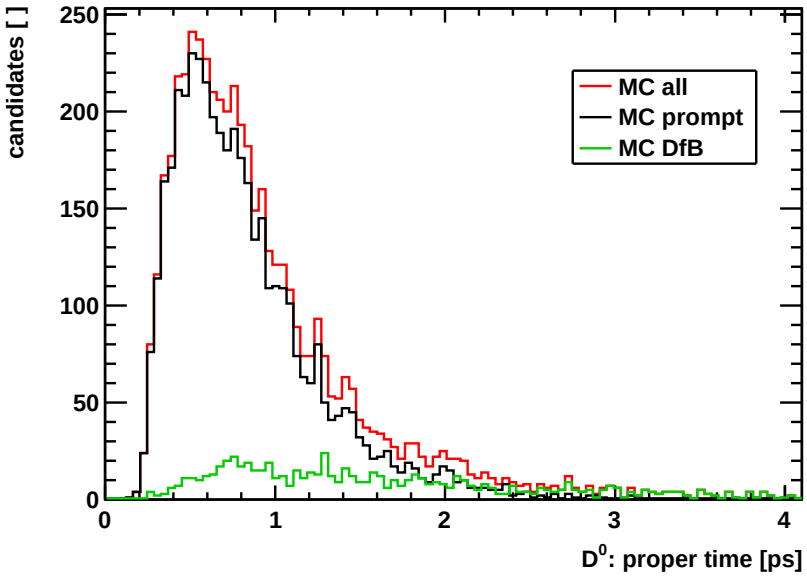

Figure 6.45.: D^0 proper time distribution in MC. The proper time distribution of all D^0 is shown in black, the part of prompt D^0 only is shown in red and the part of D^0 from B decays is shown in green.

The final D^0 lifetime fit result determined in data, see figure 6.47, is given in equation 6.27:

$$\tau_{fit} = (451.8 \pm 3.1 \pm 6.5)\,\text{fs}\,. \tag{6.27}$$

The firstly quoted error is the statistical error, the second one is the systematical error. The study of the systematical uncertainties due to the method of taking an average proper time acceptance function from MC has shown, that the current uncertainty estimate is determined by the statistical uncertainty of the MC reference fit. The pull distribution in figure 6.47 shows that all deviations are within at least $^{+6}_{-8}\,\sigma$. Due to the bad statistics of the MC sample the acceptance function is fluctuating very much. As already mentioned, an improvement of this lifetime fit method will be to fit the acceptance distribution by a smooth curve.

Obviously the final D^0 lifetime fit result is biased by 40 fs. Many investigations have been made to understand this bias. Varying the D from B fraction even by a factor of 2, see table 6.10, could at least explain a variation of $10 - 20$ fs, but not 40 fs. Another effort was made, looking at bad

DfB fraction (%)	Data τ fit [fs]
1.0×5.16	451.769 ± 3.081
2.0×5.16	433.525 ± 3.113
0.5×5.16	461.788 ± 3.058

Table 6.10.: D^0 lifetime fit results in data for different D from B fractions to test the size of the impact on the lifetime fit result.

reconstructed D^0s in MC, that are not MC associated particles but still true signal candidates. However, the fraction of these events is too small to explain the observed difference.

The next step will be to redo the full method, track resolution smearing to achieve data-MC agreement and the D^0 lifetime fit, on the stripping 12 data sample and the latest MC simulation sample. With better alignment and more continuous trigger settings the initial difference between MC and data will become smaller. Then less smearing will be necessary and less restrictive cuts used for the fine tuning of data-MC agreement will be necessary, which will decrease the systematical error, and by knowing exactly the trigger settings of data taking the bias will probably vanish completely or can be definitively better understood. Additionally, enough statistics in data due to the LHC run period in 2011 and 2012 will be available to restrict the analysis to a few very well understood trigger configurations. At the moment it is most likely, that the trigger is the source of the 40 fs bias.

Nevertheless, this thesis established a method to evaluate the proper time acceptance function in MC. The corresponding systematic uncertainties were found to be ± 6.5 fs. Most likely they will significantly decrease with later alignment versions, because less track resolution smearing is necessary. The stripping 12 data sample already provides a factor of 60 more statistics than the stripping 7 data sample, used to measure the D^0 lifetime in this thesis. A reliable method to separate the D from B background still needs to be established. At the moment this background uncertainty limits all D^0 lifetime measurements at LHCb. Perhaps this uncertainty will decrease also once the trigger is fully simulated in MC.

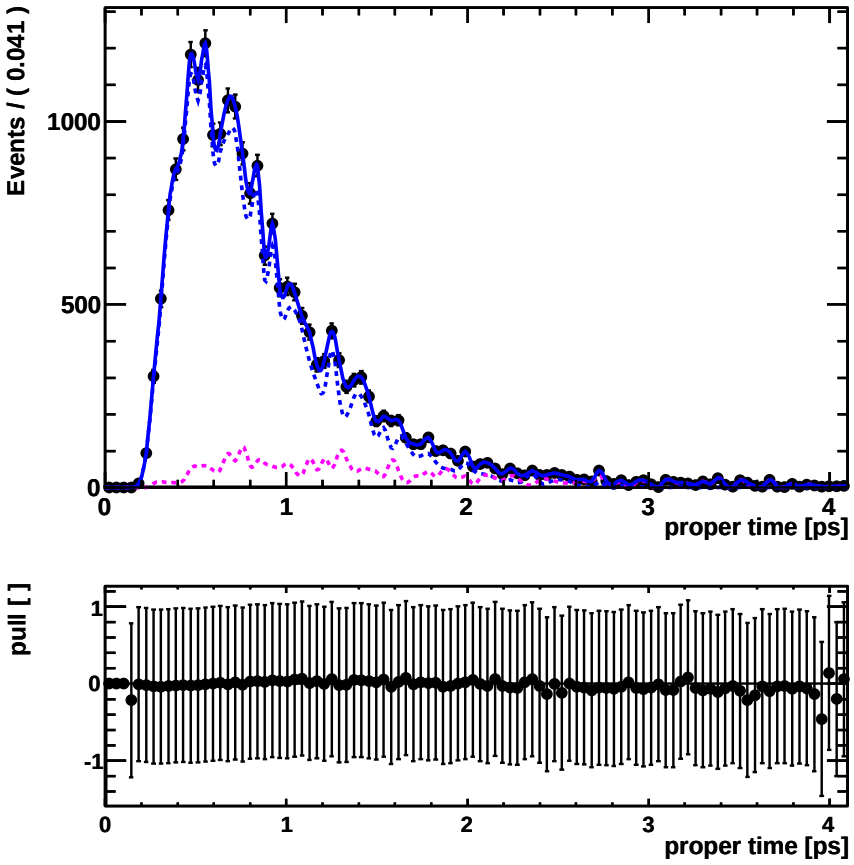

Figure 6.46.: Final Lifetime Fit in MC determining $\tau_{fit} = (408.809 \pm 3.142)\,\text{fs}$. The total proper time distribution, including D^0 coming from B, is fitted by the solid blue curve. The agitated structure is due to the low statistics of the MC sample, the acceptance function was calculated with. The dotted blue curve indicates the prompt D^0 proper time distribution part and the dotted magenta curve indicates the D^0 proper time distribution part for secondary D^0, the DfB part. The pull distribution in this MC reference fit is exactly within $1\,\sigma$, because the acceptance function was calculated on the same MC sample. Also the D^0 lifetime value was put into the simulation.

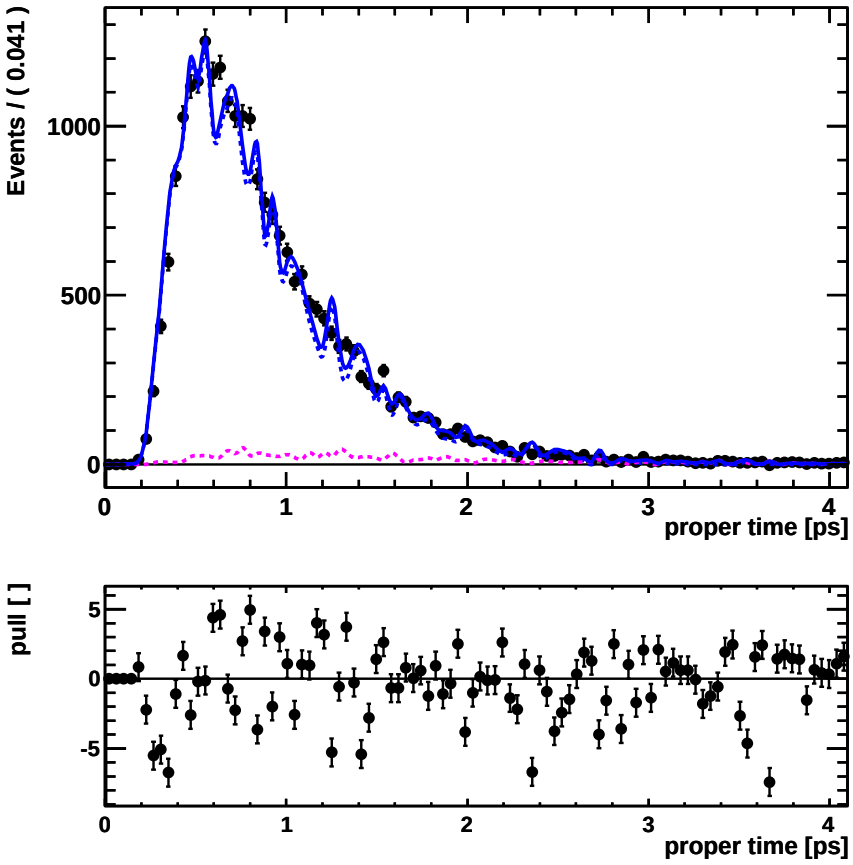

Figure 6.47.: Final Lifetime Fit in Data determining $\tau_{fit} = (451.8 \pm 3.1)\,\text{fs}$. The total proper time distribution, including D^0 coming from B, is fitted by the solid blue curve. The agitated structure is due to the low statistics of the MC sample, the acceptance function was calculated with. The dotted blue curve indicates the prompt D^0 proper time distribution part and the dotted magenta curve indicates the D^0 proper time distribution part for secondary D^0, the DfB part. There are big deviations between the data distribution and the fit model, visible in the pull distribution. This lifetime fit can be improved, once the trigger is fully understood.

7. Summary and Conclusion

The Standard Model predicts very small mixing parameters for the D^0 system. So far, only the combination of the measurements of several experiments could establish a significant non-zero mixing signal. Due to the high $c\bar{c}$ cross-section and luminosity the LHCb experiment has the unique potential to establish the first single experiment observation of D mixing and to increase the accuracy of the mixing parameters.

The mixing frequency in the D system is very slow, thus the rate of D mesons which mix is very low compared to the unmixed decays. In this thesis the self tagging 'Wrong Sign' decay $D^{*+} \to D^0\pi^+ \to (K^+\pi^-)\pi^+$ was used, where the $D^0 \to K^+\pi^-$ decay is Doubly Cabibbo Suppressed. The most challenging physics background in this analysis is the D^0 daughters double misidentification background, while the D^0 candidate is still consistent with the D^0 mass. A fake non-mixed $D^0 \to K^-\pi^+$ decay then looks like a mixed $D^0 \to \pi^-K^+$ decay. A veto against these D^0 candidates, which are assuming mistakenly interchanged mass hypotheses of their daughter particles, has been proven to be a powerful tool to reject 97% of the double misidentification background while keeping 85% of the $D^0 \to K^+\pi^-$ signal. The second source of physics background comes from random soft pions, which are accidentally associated to the D^0 to form a D^*. These fake D^* decay events peak in the D^0 mass, but since this background increases with the interaction rate of the event this background is categorized as combinatorial background. Here, it was demonstrated that using the distribution of the mass difference $m(D^*) - m(D^0)$ allows to statistically separate the signal from this random soft pion background. A minimum bias sample in data and a signal Monte Carlo sample were used to perform a multidimensional cut optimization on the first $400\,\mu\text{b}^{-1}$ of data. The found selection was then applied to the full 2010 data set of $37.7\,\text{pb}^{-1}$. 1966 signal candidates, 11813 candidates from physics background due to wrongly matched soft pions and 23 combinatorial background events have been selected. The ratio of WS to RS events has been measured with $^{\#WS}/_{\#RS} = (4.89 \pm 0.07) \times 10^{-3}$. This ratio is $5.7\,\sigma$ above the world average value. The MC study showed that maximally 10 % double misidentified RS decays remain in the WS signal. The signal established in this thesis is sufficiently large and clean enough to perform the first measurement of D^0 mixing and CP violation in the D system. It serves as starting point of the analysis which will be presented at this years winter conferences.

A crucial ingredient to any proper time dependent quantity such as the mixing or the CP asymmetry is a good description of the proper time distribution. Within this study two main issues have been addressed. First, the on- and offline selection of D^0 candidates exploits the non-zero D^0 lifetime to reject combinatorial background. That leads to a distortion of the proper time distribution. Second, a significant fraction of D^0 candidates (between 5 and 10%) are not directly produced in the proton-proton collision. They originate from B decays, thus their measured proper time distribution contains a contribution from the B lifetime. The first issue was addressed by using a proper time acceptance function derived on Monte Carlo after performing careful data-Monte Carlo comparisons. A track parameter smearing method was developed to

compensate for the worse resolution in data due to not yet final alignment and calibration of the LHC*b* detector. It was shown that associated systematics on the lifetime due to uncertainties in the data-Monte Carlo agreement result in a systematic uncertainty of $< 6.5\,\text{fs}$ on the D^0 lifetime. This uncertainty is expected to go further down on later data sets, which have been processed with an improved detector alignment. The fraction of the D from B decays has been studied by fitting the logarithmic impact parameter distribution of the D^0 . It was found to be $(12.44 \pm 0.27)\,\%$ in Monte Carlo, however only $(5.16 \pm 0.20)\,\%$ in data. In this thesis it was demonstrated that the uncertainty on the fraction of D from B is the limiting factor in the lifetime analysis. Currently $10 - 15\,\text{fs}$ have to be assigned to this source. Finally the lifetime fit was performed on a data set corresponding to $0.6\,\text{pb}^{-1}$ of early 2010 LHC*b* data, taken in May and June 2010. A D^0 lifetime of $\tau = (451.8 \pm 3.1(\text{stat.}) \pm 6.5(\text{syst.})\,\text{fs}$ was measured. Unfortunately the trigger configuration for this data taking period changed frequently and is not modeled in Monte Carlo. Therefore the found fit result is as expected not consistent with the PDG value within the uncertainties. We are optimistic that this problem is solved automatically by moving to a later data set, which however was not available in time to be analyzed in this thesis.

The Large Hadron Collider will continue data taking in 2011/2012 at a center-of-mass energy of 7 TeV. About $1 - 3\,\text{fb}^{-1}$ of data are expected to be taken, which would be a large enough sample to perform the competitive charm physics programme outlined in this thesis.

A. Appendix

A.1. Additional Selection Optimization Curves

Figure A.1 shows the optimization curve corresponding to the momentum distribution p of the D^0 daughters K and π. The small rise in the signal significance at $p > 5000\,\text{MeV}$ is due to statistical fluctuations. Hence, this cut does not improve the signal significance. It is not included in the final selection.

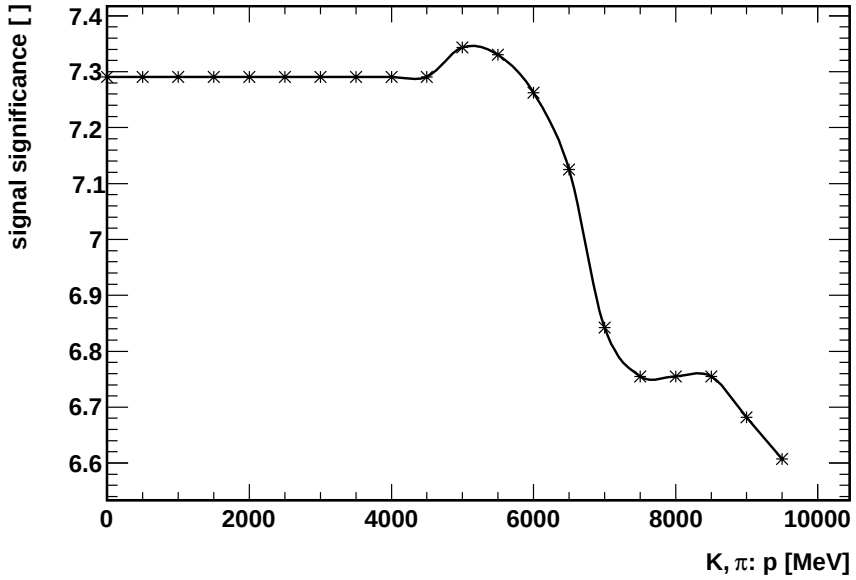

Figure A.1.: K, π: Cut optimization curve of the momentum (p) distribution, maximizing the total signal significance σ_{sig} of the decay. The apparent signal significance maximum at $p > 5000\,\text{MeV}$ is due to statistical fluctuations. This cut is not included in the final selection.

Figure A.2 shows the optimization curve corresponding to the track χ^2/ndf distribution of the D^0 daughters K, π. A cut on the track $\chi^2/ndf < 5$ is required by the tracking group to obtain a good track quality, that is necessary to perform the track smearing method. Nevertheless, the signal significance optimization curve shows, that due to the other cuts a good track quality is guaranteed without cutting explicitly on this variable. Only at track $\chi^2/ndf < 3$ the signal significance starts to rise, but this is a limit case. Because, a requirement of track $\chi^2/ndf < 2$

is comparable to reject every second track by chance. Thus, this cut is not included in the final selection.

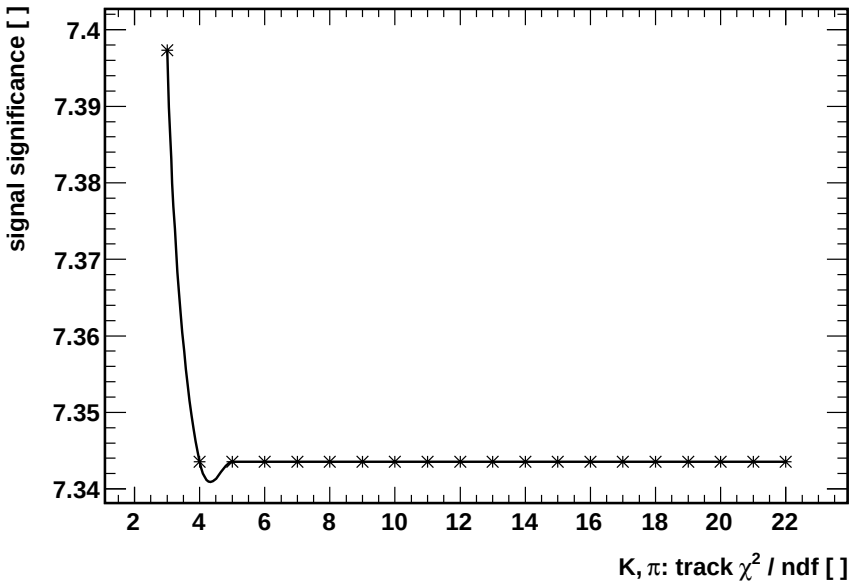

Figure A.2.: K, π: Cut optimization curve of the track χ^2/ndf distribution, maximizing the total signal significance σ_{sig} of the decay. This cut is not included in the final selection.

Figure A.3 shows the signal significance optimization curve corresponding to the transverse momentum distribution of the D^0. Due to the other cuts, the D^0 p_T cut, chosen at $p_T > 1000\,\mathrm{MeV}$, is useless. The small rise in σ_{sig} at $p_T = 2000\,\mathrm{MeV}$ is treated as statistical fluctuation. Figure A.3 shows, that within this set of cuts a higher choice of the D^0 p_T cut value will lead to loosing more signal than it suppressing background. The D^0 p_T cut is not included in the final selection.

Figure A.4 shows the signal significance optimization curve corresponding to the vertex χ^2/ndf distribution of the D^0. Due to the other cuts, also the D^0 vertex χ^2/ndf cut, chosen at $\chi^2/ndf < 10$, is useless. The small bump in σ_{sig} at $\chi^2/ndf = 10\,\mathrm{MeV}$ is treated as statistical fluctuation. A tighter D^0 vertex χ^2/ndf cut leads to more signal loss than background suppression. The D^0 vertex χ^2/ndf cut is not included in the final selection.

Figure A.5 shows the signal significance optimization curve corresponding to the transverse momentum distribution of the π_s. In this set of selection variables, the cut on the transverse momentum of the slow π is counterproductive. Increasing the cut limit leads to more signal loss than background suppression.

Figure A.6 shows the signal significance optimization curve corresponding to the vertex χ^2/ndf distribution of the D^*. The signal significance curve stagnates until vertex χ^2/ndf cut values of 10. For smaller cut values, more signal is lost than background suppressed. In this selection a loose cut on the D^* vertex $\chi^2/ndf < 13$ was considered, but in the final selection, this cut is obviously not included any more.

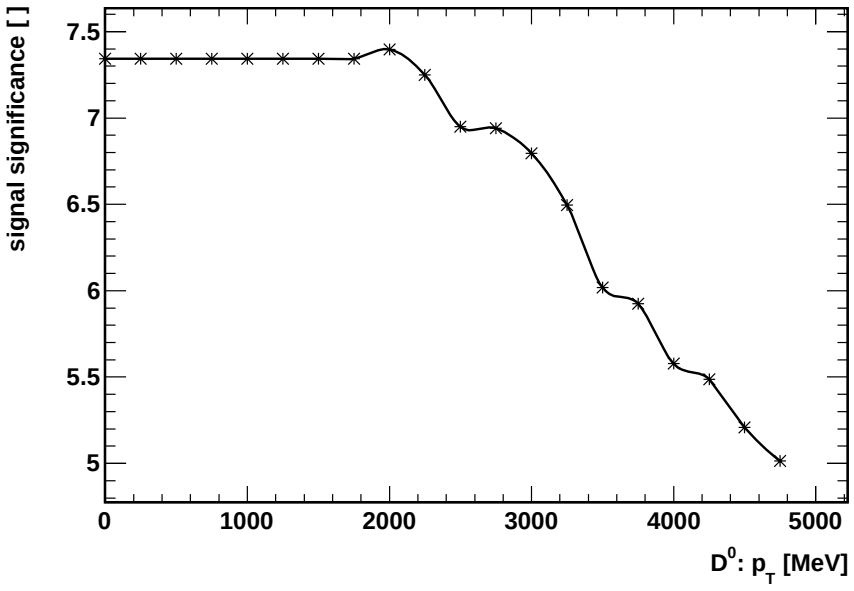

Figure A.3.: D^0: Cut optimization curve of the transverse momentum p_T distribution, maximizing the total signal significance σ_{sig} of the decay. The p_T cut value was initially chosen at $p_T > 1000\,\mathrm{MeV}$, but it is useless for this selection. It is not included in the final selection.

Figure A.7 shows the signal significance optimization curve corresponding to the track χ^2/ndf distribution of the π_s. The signal significance curve stagnates until track χ^2/ndf cut values of 4. For smaller cut values, more signal is lost than background suppressed. The tracking group recommends a track $\chi^2/ndf < 5$ cut to obtain a good track quality, which is also necessary for the track smearing method. In the final selection, this cut is obviously not included any more.

Figure A.8 shows signal significance optimization curve corresponding to the impact parameter significance (IP_{sig}) distribution of the π_s. The signal significance curve stagnates until IP_{sig} cut values of 4. Here, it was tested to improve the signal significance through an $IP_{sig} < 5$ cut. This cut is totally useless within this selection. It is not included in the final selection.

A.2. Additional Remarks On An Alternative Lifetime Fit Approach

An alternative ansatz to correct for the lifetime bias in hadronic decays can be made by taking an event by event acceptance function, determined in data [11]. The argument using an event by event acceptance function and not an average MC simulation acceptance function is, that there is no straightforward relation between the impact parameter cuts, made by the trigger, and the resulting average lifetime acceptance function. The trigger cuts are applied to a simplified reconstruction for reasons of the computing time available. Hence, the trigger cuts are called online, while the stripping selection cuts are done on the full reconstruction information, they are called offline.

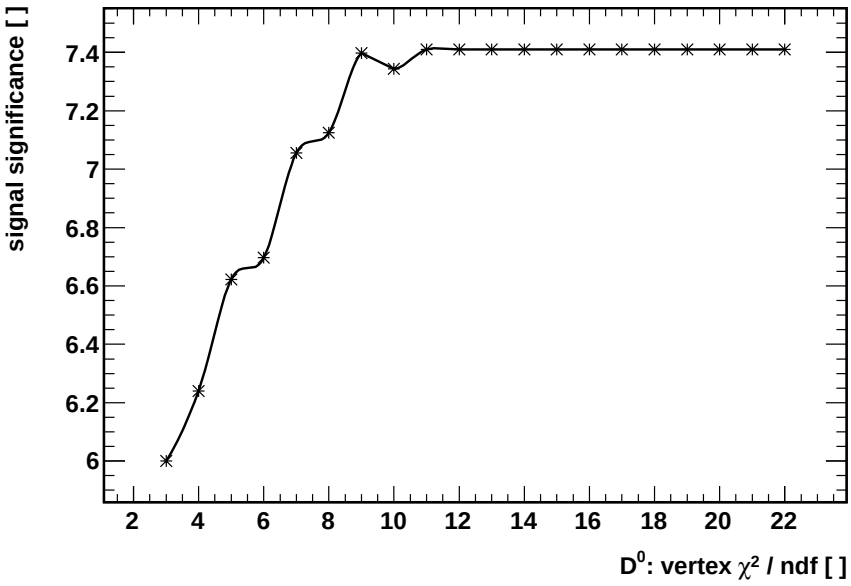

Figure A.4.: D^0: Cut optimization curve of the vertex χ^2/ndf distribution, maximizing the total signal significance σ_{sig} of the decay. The vertex χ^2/ndf cut value was initially chosen at $\chi^2/ndf < 10$, but it is useless for this selection. It is not included in the final selection.

The online quantities cannot be directly linked to those from the offline reconstruction. The event by event acceptance function method follows the principle that the probability density for observing a decay with a set of kinematic variables kin at time t, $f(t, kin)$, can be factorised as

$$f(t, kin) = f(t|kin) \cdot f(kin)\,. \tag{A.1}$$

The key argument is, that the probability density of the event kinematics, $f(kin)$, is independent of the measured proper time. The event kinematics rather depend on the phase space of the decay and on potential form factors describing non-uniformities in the decay distributions. Nevertheless, the connection between the measured proper time and the event kinematics is made by selection cuts, e.g. at the trigger level. Due to these cuts, the event kinematics enter as a condition in $f(t|kin)$.

The efficiency for detecting and reconstructing an event is independent of the proper time. Hence, an event by event acceptance function acquires values of either zero (rejected) or one (accepted). For an event with given kinematics, i.e. fixed track slopes and momenta, there is a direct relation between the proper time and the impact parameters of the tracks. Thus, cuts on impact parameters directly translate into a discrete decision about acceptance or rejection of an event as a function of its proper time. Therefore, the event by event acceptance function takes the shape of a step function. The method to determine the event by event acceptance function is, evaluating the trigger decisions for all proper times. Since the acceptance function here is a step

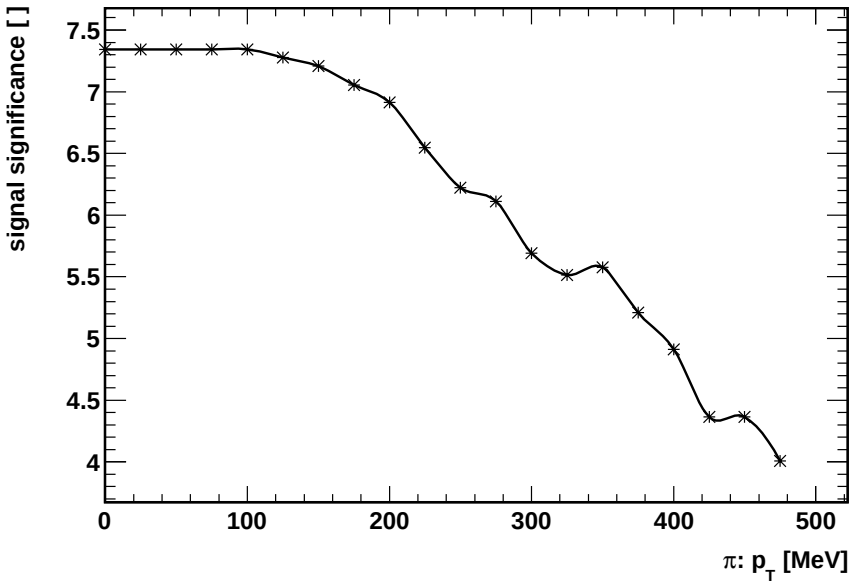

Figure A.5.: π_s: Cut optimization curve of the transverse momentum (p_T) distribution, maximizing the total signal significance σ_{sig} of the decay. The p_T cut value was initially chosen at $p_T > 110\,\text{MeV}$. Increasing the cut value within this selection is counterproductive.

function, only the position of the step has to be determined. This is done in the following way using an interface to the LHC*b* trigger software implemented for this purpose. The tracks used to reconstruct the decay offline have to be associated to their counterparts in the online environment. This can be done with special associator tools. The position of the primary vertex as reconstructed in the trigger is changed along the flight direction of the particle, defined as the connecting line between the primary vertex and the decay vertex of the particle. The trigger decision is then evaluated for each new PV position using only the tracks from the signal decay. Once a change in the trigger decision, i.e. a step in the acceptance, is found the procedure is repeated around this position with a refined step size to increase precision. Varying the primary vertex positions and not the tracks themselves is done to simplify the implementation. The differences are small and therefore neglected. Also for simplification reasons events with only one primary vertex are taken. The proper time bias caused by the offline selection is treated in the same way. After having obtained the event by event acceptance function for a data sample the average lifetime acceptance function can also be extracted:

$$\text{Acceptance}(t) = \frac{\sum_i \Theta(t - t_{min}) e^{t_{min,i}/\tau}}{\sum_i e^{t_{min,i}/\tau}}\,. \tag{A.2}$$

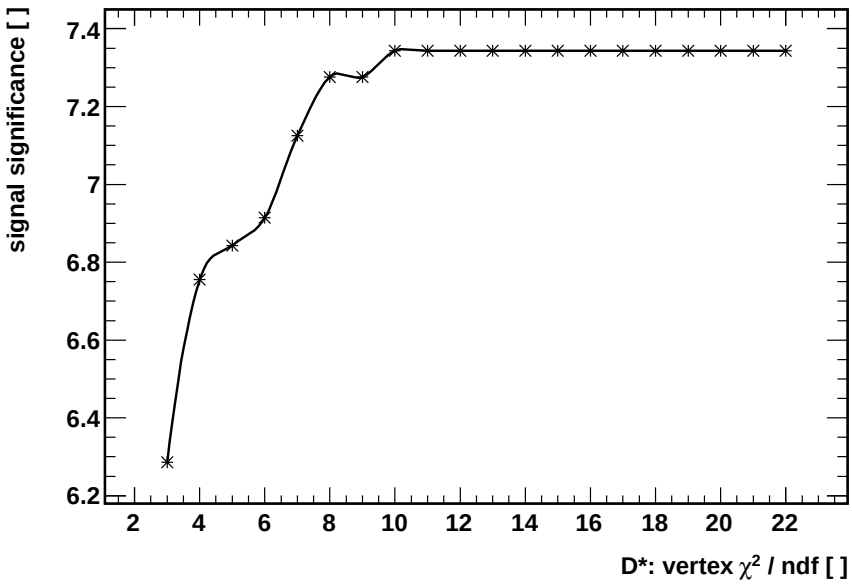

Figure A.6.: D^*: Cut optimization curve of the vertex χ^2/ndf distribution, maximizing the total signal significance σ_{sig} of the decay. The vertex χ^2/ndf cut value was initially chosen at $\chi^2/ndf < 13$, but obviously this cut is useless. It is not included in the final selection.

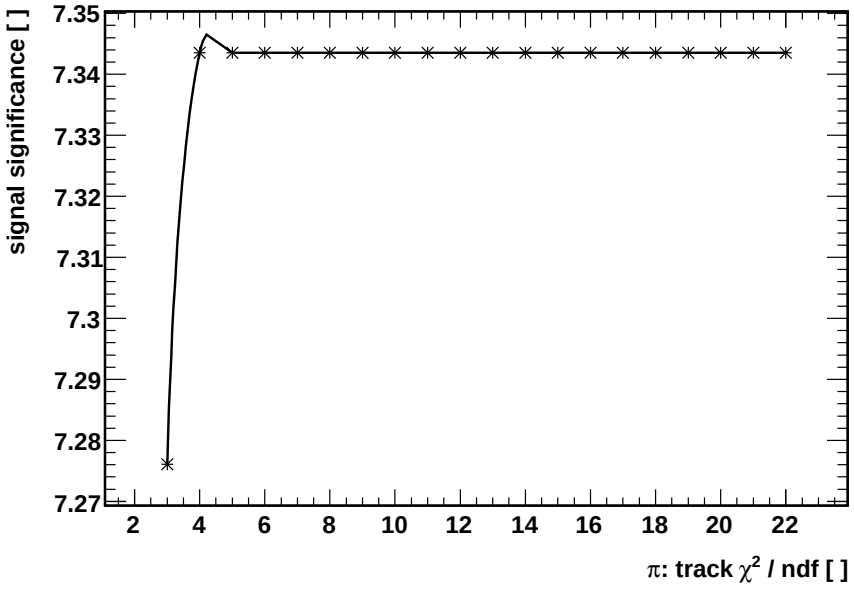

Figure A.7.: π_s: Cut optimization curve of the track χ^2/ndf distribution, maximizing the total signal significance σ_{sig} of the decay. The track χ^2/ndf cut value was initially chosen at $\chi^2/ndf < 5$, as recommended by the tracking group, but obviously here this cut is useless. It is not included in the final selection.

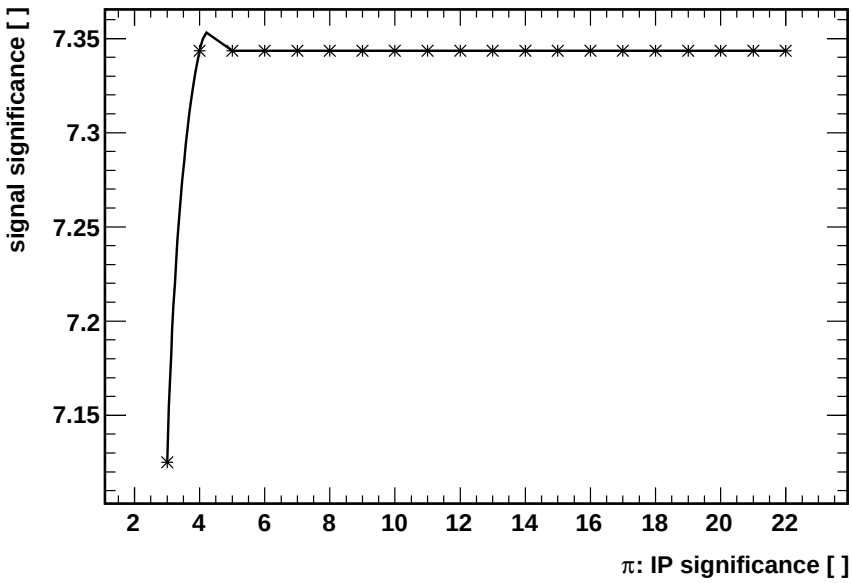

Figure A.8.: π_s: Cut optimization curve of the impact parameter significance (IP_{sig} distribution, maximizing the total signal significance σ_{sig} of the decay. The IP_{sig} cut value was initially chosen at $IP_{sig} < 5$, but obviously this cut is useless. It is not included in the final selection.

Bibliography

[1] BaBar collaboration, B. Aubert, et al., Evidence for D0-anti-D0 Mixing, *Phys.Rev.Lett.*, *98*(211802), 2007.

[2] Barrand, G., et al., GAUDI - A software architecture and framework for building HEP data processing applications, *Comput. Phys. Commun.*, *140*(45), 2001.

[3] Belle collaboration, M. Staric, et al., Evidence for $D^0 - \bar{D}^0$ Mixing, *Phys.Rev.Lett.*, *98*(211803), 2008.

[4] Belyaev, I., et al., Simulation application for the LHCb experiment, *physics/0306035*, 2003.

[5] Cabibbo, N., Unitary Symmetry and Leptonic Decays, *Phys.Rev.Lett.*, *10*, 531–532, 1963.

[6] CDF collaboration, T. Aaltonen, et al., Evidence for D0-D0bar mixing using the CDF II Detector, *Phys.Rev.Lett.*, *100*(121802), 2008.

[7] CERN, `http://te-epc-lpc.web.cern.ch/te-epc-lpc/machines/lhc/general.stm`, 2011.

[8] CKMfitter group, J. Charles, et al., updated results and plots available at: http://ckmfitter.in2p3.fr, 2011.

[9] Corti, G., et al., Software for the LHCb Experiment, *IEEE Transactions on Nuclear Science*, *53*(3), 2006.

[10] GEANT 4 collaboration, GEANT, *Nucl. Inst. and Methods*, *A 506*(250), 2003.

[11] Gersabeck, M., *Alignment of the LHCb Vertex Locator and Lifetime Measurements of Two-Body Hadronic Final States*, CERN-THESIS-2009-118, 2009.

[12] Glashow, S., Partial-Symmetries of Weak Interactions, *Nucl.Phys.*, *22*, 579, 1961.

[13] Glashow, S., J. Iliopoulos, and L. Maiani, Weak Interactions with Lepton-Hadron Symmetry, *Phys. Rev.*, *D2*, 1285, 1970.

[14] Heavy Flavor Averaging Group, `http://www.slac.stanford.edu/xorg/hfag/charm/CHARM10/results_mix+cpv.html`, 2010.

[15] J. Van Tilburg, *Track simulation and reconstruction in LHCb*, CERN-THESIS-2005-020, 2005.

[16] Kobayashi, M., and T. Maskawa, CP-Violation in the Renormalizable Theory of Weak Interaction, *Prog.Theor.Phys.*, *49*, 652–657, 1973.

[17] LHC machine outreach, `http://lhc-machine-outreach.web.cern.ch/lhc-machine-outreach/lhc_in_pictures.htm`, 2011.

[18] Nachtmann, O., *Phänomene und Konzepte der Elementarteilchenphysik*, Friedr. Vieweg & Sohn, 1986.

[19] Nakamura, K., et al., Review of Particle Physics, *J.Phys.*, *G37*(075021), 2010.

[20] Nir, Y., CP Violation in Meson Decays, *arXiv:hep-ph/0510413v1*, 2005.

[21] Ryd, A., et al., EvtGen A Monte Carlo Generator for B-Physics, *BAD 522 v6.*, 2005.

[22] S. Weinberg, A Model of Leptons, *Phys.Rev.Lett.*, *19*, 1264, 1967.

[23] Salam, A., and J. Ward, Electromagnetic and weak interactions, *Phys.Lett.*, *13*, 168, 1964.

[24] Sjöstrand, T., et al., PYTHIA, *Computer Physics Commun.*, *135*(238), 2001.

[25] SuperB, A Super Flavor Factory, `http://web.infn.it/sbuser/index.php/en/physics?start=1`, 2010.

[26] The LHCb Collaboration, *LHCb Technical proposal*, CERN-LHCC/98-4, 1998.

[27] The LHCb Collaboration, *LHCb Calorimeters Technical Design Report*, CERN/LHCC-2000-036, 2000.

[28] The LHCb Collaboration, *LHCb Muon Technical Design Report*, CERN/LHCC-2000-037, 2000.

[29] The LHCb Collaboration, *LHCb RICH technical design report*, CERN-LHCC/2000-037, 2000.

[30] The LHCb Collaboration, *LHCb Velo technical design report*, CERN-LHCC/2001-011, 2001.

[31] The LHCb Collaboration, *LHCb Outer Tracker Technical Design Report*, CERN/LHCC-2001-024, 2001.

[32] The LHCb Collaboration, *LHCb Inner Tracker design report*, CERN-LHCC/2002-029, 2003.

[33] The LHCb Collaboration, *LHCb Trigger System Technical Design Report*, CERN/LHCC-2003-031, 2003.

[34] The LHCb Collaboration, *LHCb Computing Technical Design Report*, CERN/LHCC-2005-019, 2005.

[35] The LHCb Collaboration, *The LHCb Detector at the LHC*, 2008 JINST 3 S08005, 2008.

[36] The LHCb Collaboration, 2010 Data: Plots for conferences and seminars, `https://lhcb-phys.web.cern.ch/lhcb-phys/Data_2010/default.htm`, 2010.

[37] The LHCb Collaboration, Roadmap for selected key measurements of LHCb, 2010.

[38] The LHCb Collaboration, LHCb Silicon Tracker - Material for Publications, 2010.

[39] The LHCb Collaboration, *Search for the rare decays* $B_s^0 \to \mu^+\mu^-$ *and* $B^0 \to \mu^+\mu^-$, LHCb-PAPER-2011-004, 2011.

[40] The LHCb Collaboration, *Measurement of* Δm_d *in* $B_d \to D^-\pi^+$, LHCb-ANA-2011-015-v4, 2011.

[41] The LHCb Collaboration, *Measurement of* Δm_s *in the decay* $B_s \to D_s(3)\pi$, LHCb-ANA-2011-005-v4, 2011.

Acknowledgements (Danksagungen)

Ich möchte mich bei allen bedanken, die zum Gelingen dieser Arbeit beigetragen haben. Dies sind insbesondere:

Die Heidelberger LHC*b* Arbeitsgruppe,

meine Familie,

mein liebster Eric

und alle meine Freunde, die mich von der Arbeit ablenken konnten.

Statement of Originality (Erklärung):

I certify that this thesis, and the research to which it refers, are the product of my own work. Any ideas or quotations from the work of other people, published or otherwise, are fully acknowledged in accordance with the standard referencing practices of the discipline.

Ich versichere, dass ich diese Arbeit selbständig verfasst und keine anderen als die angegebenen Quellen und Hilfsmittel benutzt habe.

Heidelberg, February 25, 2011

.....
(signature)